



TECHNISCHE  
UNIVERSITÄT  
WIEN

Dissertation

---

## Self-assembly scenarios of Inverse Patchy Colloids

---

ausgeführt zum Zwecke der Erlangung des Akademische Grades eines Doktors  
der Naturwissenschaften unter der Leitung von

Ao. Univ. Prof. Dr. Gerhard Kahl  
Institut für Teoretische Physik (E136)  
Technische Universität Wien

eingereicht an der Technischen Universität Wien  
Fakultät für Physik

von  
Dott. Mag. Silvano Ferrari  
Matrikelnummer 1229767

Wien, im Dezember 2015



## Kurzfassung

Spontane Selbst-Organisation bezeichnet die Fähigkeit von kolloidalen Teilchen, sich ohne äußere Einflüsse (wie etwa elektrische Felder oder chemische Wirkstoffe) in (geordneten) Strukturen anzuordnen. In dieser Arbeit wurde die Selbst-Organisation von sogenannten *Inverse patchy colloids* (IPCs) untersucht: diese Teilchen wurden ursprünglich als Modellsysteme eingeführt, um adsorbierte Sternpolymere auf geladenen Kolloiden zu beschreiben. Das daraus entwickelte Modell lässt sich aber auch zur Charakterisierung eines breiten Spektrums von Kolloiden mit heterogen geladenen Oberflächen heranziehen.

Unsere IPCs bestehen aus einem negativ geladenen, sphärischen Zentralteilchen, das auf den Polregionen mit positiv geladenen *patches* dekoriert ist. Als Folge der komplexen Attraktion und Repulsion der verschiedenen geladenen Oberflächenbereiche sind die Wechselwirkungspotentiale dieser Teilchen (und somit auch ihr Phasenverhalten) deutlich komplexer als jene konventioneller *patchy colloids*.

Mit Hilfe von Molekulardynamik Simulationen haben wir ein Spektrum an physikalischen Eigenschaften von IPCs untersucht, wobei wir – neben der Temperatur und der Dichte – insbesondere die Oberflächenladungsverteilung der verschiedenen Regionen, die Größe der *patches* und deren Interaktionsreichweite systematisch verändert haben. Dabei haben wir gefunden, dass Modelle mit kleiner *patch* Größe keine geordneten Strukturen bilden können; die entstandenen ungeordneten Phasen wurden auch mit Integralgleichungsverfahren untersucht. Weiters konnte gezeigt werden, dass IPC Modelle mit *patches* mittlerer Größe eine neue hybride kristall-flüssig Phase bilden können: ihre Eigenschaften wurden mit Hilfe statischer und dynamischer Korrelationsfunktionen eingehend untersucht. Schließlich wurde gefunden, dass IPCs mit großen *patches* in FCC Gittern kristallisieren.



## Abstract

Spontaneous self-assembly is a process in which a disordered system crystallizes into an ordered structure without external influence. In this work, we study the self-assembly properties of inverse patchy colloids (IPCs). IPCs were originally introduced to describe the complex colloids formed by the adsorption of polyelectrolyte stars onto charged colloids, however the proposed model of IPCs is very versatile and can be used to describe many real systems of colloids with a heterogeneously charged surface.

We consider IPCs composed of a negatively charged central body and two positively-charged patches localised at the poles. The complex interplay between the regions of like and unlike charge makes the phase behavior of IPCs considerably more complex than the one typical of conventional patchy colloids.

Using molecular dynamics simulation, we investigated the model by varying the charge distribution, the size of the patches, and the interaction range. Models with small patch extension did not spontaneously self-assemble into any ordered structure, thus we studied their fluid phase by means of integral equation theories. Models with medium patch extension crystallized in a novel hybrid crystal-liquid structure, that we characterized by means of correlation functions. Finally, models with large patch amplitudes formed a face centered cubic lattice.





*In ricordo di Giuseppe Pitzalis (1960-2008)*

*“Mi piace il numero quindici, si può usare in tante espressioni:  
fino a pagina quindici, quindici piegamenti. . . ”*





# Contents

<b>1</b>	<b>Why bother reading?</b>	<b>11</b>
<b>2</b>	<b>Inverse patchy colloids</b>	<b>13</b>
2.1	<i>Colloids</i> . . . . .	13
2.2	<i>Patchy</i> colloids . . . . .	15
2.3	<i>Inverse</i> patchy colloids . . . . .	16
2.4	Studies of IPCs . . . . .	19
<b>3</b>	<b>The physics behind</b>	<b>21</b>
3.1	Static properties: thermodynamics . . . . .	22
3.1.1	Ensembles and macrostate . . . . .	22
3.1.2	Phase diagram and phase transitions . . . . .	23
3.2	Static properties: structure . . . . .	25
3.2.1	Reduced distribution function . . . . .	25
3.2.2	Homogeneous and inhomogeneous systems . . . . .	27
3.2.3	Pair correlation and static structure factor . . . . .	29
3.2.4	Further correlation functions, integral equation theories . . . . .	30
3.2.5	Extension of integral equations to anisotropic particles . . . . .	32
3.3	Dynamic properties . . . . .	33
3.3.1	Time-dependent correlation functions . . . . .	33
3.3.2	Mode coupling theory, solution, non-ergodicity factor . . . . .	34
3.4	Solution schemes for the theoretical approaches . . . . .	36
3.4.1	Lado RHNC solution (for the $g(r)$ and the thermodynamics) . . . . .	36
3.4.2	Barker-Henderson TPT (for the thermodynamics) . . . . .	38
3.4.3	MCT solution (non-ergodicity factor) . . . . .	38
3.5	Numerical simulations using molecular dynamics . . . . .	40
3.5.1	Velocity-Verlet algorithm . . . . .	40
3.5.2	Adaptation of the potential . . . . .	40
3.5.3	Adaptation of the algorithm . . . . .	41
<b>4</b>	<b>Results</b>	<b>47</b>
4.1	Symmetric models with small patch extension . . . . .	51
4.1.1	Phase diagram . . . . .	52
4.1.2	Dynamics . . . . .	52
4.1.3	Static structure . . . . .	53
4.1.4	Thermodynamics . . . . .	56
4.1.5	Small-patch models: summary . . . . .	58
4.2	Models with $\gamma_1 = 45^\circ$ . . . . .	60
4.2.1	The crystal-liquid structure formed by model 45n . . . . .	60

*Contents*

4.2.2	Phase diagram of the 45n model . . . . .	65
4.2.3	Dynamics of the 45n model . . . . .	65
4.2.4	Overcharging and undercharging of symmetric IPCs: 45sQc models . .	68
4.2.5	Models with asymmetric patches . . . . .	68
4.2.6	45* models: summary . . . . .	70
4.3	Symmetric models with larger patch extension . . . . .	71
4.4	Completely asymmetric models . . . . .	72
<b>5</b>	<b>Conclusions</b>	<b>73</b>
<b>6</b>	<b>Widmung (ringraziamenti)</b>	<b>81</b>
<b>7</b>	<b>Curriculum Vitae</b>	<b>85</b>

# 1 Why bother reading?

Spontaneous self-assembly is a process where a disordered system crystallizes into an ordered structure without external influence [GS07], like electric fields or chemical agents. What triggers this process, and how to obtain control into which ordered structure will be formed, are yet open questions that scientists from many different fields (physicists, chemists, material engineers...) try to answer. Such a question arises not only out of scientific curiosity, but also because of the huge amount of possible applications ranging from medicine (drug delivery, tissue synthesis) to technology (construction of devices and sensors).

The predominant approaches for the manufacture of complex materials are top-bottom methods, which work like the sculpture: for example, computer microprocessors are manufactured via photolithography, where silicon layers are shaped using lasers or X-rays. Top-bottom methods have a major disadvantage: they can be very expensive, partially because they waste materials during the “sculpting”. The opposite approaches are called bottom-up processes. Methods that follow this philosophy aim to construct smart building blocks that will eventually form the desired structure without further action or, in other words, will self-assemble. Consequently, there is no waste of materials (as long as the production of the building blocks is efficient).

Spherical colloids with isotropic interactions only yield phases of simple symmetry such as face- or body-centered cubic: self-assembly of more complex phases requires particles that are either anisometric (i.e. nonspherical) or have anisotropic interactions. In this work, we focus on a model for colloids with heterogeneously charged surfaces, the so-called inverse patchy colloids (IPCs). With a negatively charged central body and positively charged patches at the poles, IPCs are characterized by their charge distribution, their interaction range, and the size of the patches. The first two parameters are fixed during the synthesis, while the interaction range is influenced by the pH of the solution in which the IPCs are dissolved. In conventional patchy colloids, the patches attract each other; in IPCs, due to the charge distribution, patches repel each other while attracting the center of the colloid. This “inverse” behavior of IPCs with respect to conventional patchy particles is the origin of the name “inverse” patchy colloids.

Using molecular dynamics simulations, we study few IPC models, varying the parameters that characterize the interaction: the patch size, the interaction range and the charge distribution. We identify which parameter combinations lead to spontaneous self-assembly of ordered structures, and we characterize these structures in depth from both the structural and the dynamical point of view.

The thesis is organized as follows. **Chapter 2** introduces inverse patchy colloids, and summarizes some results about IPCs from other authors that are useful in the context of this work. **Chapter 3** introduces the theoretical framework needed to study inverse patchy

*1 Why bother reading?*

colloids, namely the correlation-functions formulation of fluid state theory (first three sections), some self-consistent approximated methods to compute correlation functions (fourth section), and molecular dynamics computer simulations (fifth section). **Chapter 4** contains a summary of the results obtained in the three years of the Ph. D. studies, divided in four sections, each one describing a group of IPC models with similar self-assembly properties. Finally **Chapter 5** presents some concluding remarks.

## 2 Inverse patchy colloids

### Contents

2.1	<i>Colloids</i> . . . . .	13
2.2	<i>Patchy colloids</i> . . . . .	15
2.3	<i>Inverse patchy colloids</i> . . . . .	16
2.4	<i>Studies of IPCs</i> . . . . .	19

### 2.1 Colloids

The usual dictionary definition of colloidal dispersion involves a mesoscopic solute in a microscopic solvent. A more precise reference, maybe an encyclopedia or even Wikipedia, specifies the dimensions of the solute as ranging between the micrometer and the nanometer scale. To understand where these limits come from, one has to think about the most important phenomena regarding colloids, the Brownian motion, in which the solute is seen floating, apparently randomly, in the solvent, without being forced to sediment by gravity. The following definition comes from [Fre02].

Let us consider a small isolated body of mass  $m$  and density  $\rho$ . The body is put in a container, filled with a medium of density  $\rho_m$  at temperature  $T$ ; the gravitational field is considered constant and of intensity  $g$ . If the density of the body is larger than that of the medium, it will not float on the surface, and its mass will be reduced by the buoyancy to  $m^* = m(1 - \rho_m/\rho)$ . In this condition, the body will be found at an average height  $h$  from the bottom of the the container of

$$\langle h \rangle = \frac{\int_0^\infty h \exp\left(-\frac{m^*gh}{k_B T}\right) dh}{\int_0^\infty \exp\left(-\frac{m^*gh}{k_B T}\right) dh} = \frac{k_B T}{m^*g}, \quad (2.1)$$

where  $k_B$  is Boltzmann's constant. At room temperature, a macroscopic body with a mass as small as a tenth of gram will just sink to the bottom of the box: a colloid has to be much smaller. [Fre02] defines a colloid as a body that can float higher than its size: assuming a spherical shape with radius  $\sigma$ , the condition  $k_B T/m^*g > 2\sigma$  can be expressed as

$$\frac{3k_B T}{8\pi(\rho - \rho_m)g} > \sigma^4. \quad (2.2)$$

For an excess density of  $\rho - \rho_m = 1 \text{ g/cm}^3$ , this formula gives the upper limit of  $1 \mu\text{m}$  stated in the beginning – on earth. Of course, the same experiment carried in a space station would allow a larger size.

From this formula alone, it would seem that every material with a sufficiently low density would behave as a colloid, but this is not what intuition suggests. A solute molecule is not

only meant to float: it also has to move due to thermal diffusion. In a time  $\Delta t$ , a spherical particle diffuses approximatively  $\sqrt{2D\Delta t}$  where  $D$  is the diffusion constant. Since for a spherical particle  $D = k_B T / 3\pi\eta\sigma$ , with  $\eta$  the viscosity of the medium, the time required to diffuse further than a diameter is

$$\Delta t(2\sigma) \simeq \frac{3\pi\eta\sigma^3}{k_B T}. \quad (2.3)$$

For realistic values of  $\eta$ , a diffusion over  $2\sigma$  with  $\sigma \simeq 1\mu\text{m}$  happens in times of the orders of seconds; and due to the cubed radius, increasing the size leads to a fast increasing diffusion time. Thus, a macroscopic body of the same density as water (some kinds of wood, for example) would only be a colloid in a timescale much larger than that of human observation times.

The lowest limit stems instead from the physical description. A colloid is defined [Fre02] as something whose internal structure is not needed for the description of the phase behavior. This of course does not mean that the internal structure is irrelevant, just that the phase behavior can be predicted without its knowledge. For example, to understand the biological function of a protein, their exact chemical composition is crucial; but to compute its phase diagram in water solution, it is not. Thus, the same body can be regarded or not as a colloid depending on which properties are being studied.

There are at least three good practical reasons for which colloids are interesting.

- For theorists (physicists and chemists): colloidal solutions are composed by a solute and a solvent, and the particles of the former are larger (and slower) than those of the latter by some order of magnitudes. When the study is only concerned with the solute, the exact dynamics of the solvent is so fast that it can be treated as if it was a continuous medium, and the interaction between solute and solvent can be approximated with wonderful accuracy using classical statistical mechanics. Thus, the required mathematical methods are well-known and simple, leaving the researcher free to concentrate on the physics.
- For experimentals (physicists, chemists, biologists, engineers. . .): colloids are cheap and reasonably fast to manufacture, and due to their size observations can be carried with optical microscopy. Again, this frees the researcher to concentrate on the physics and not on the methods.
- For everybody: there are many technologic applications of colloids. They are ubiquitous, within our bodies, in the food we eat, in many things we use in everyday life. Further, considerable hope rests on colloidal science for the discovery of new technology.

A key feature of colloids, and in general of substances in solution, is the range of interactions. Long-ranged interactions are well known and frequently present simple phase diagrams like the left one in figure 2.1: a well defined vapor/liquid transition, with both a triple and a critical point. This kind of behavior is well documented in literature [HM06].

Short-ranged interactions are frequently associated with computer simulations. In fact it is true that the first computer, the ENIAC built in Los Alamos during the Manhattan Project, was tested simulating the dynamics of hard disks, and later of hard spheres. These

studies showed that hard particles without attractive forces have a simple phase diagram, with only a fluid and a face centered cubic crystal (FCC) state (figure 2.1, center) depending on the density (temperature obviously does not play a role). Even this, at the time, sounded unbelievable: while now it is understood that short-ranged repulsion and excluded volume effect are the main factors that decide the phase behavior of a system, at the time it was widely believed that any phase transition occurred thanks to attractive interactions. It was even argued that hard particles were unphysical, but at present day this model is frequently used to study many systems (for example silica particles [RJWS09]) and they are often used as the first degree of approximation in studies of other particles.

If a short-ranged isotropic attraction is added to hard spheres, the phase diagram is similar to the one for particles with long-ranged interactions. Fluid-solid transition depends again on temperature, and a liquid-vapor transition branch is found (figure 2.1, right), although it is only a metastable state that would separate to solid-fluid given an infinite time. Isotropic short-ranged interactions were also extensively studied in the sixties and seventies, and they are well understood theoretically thanks to integral-equations theories [HM06].

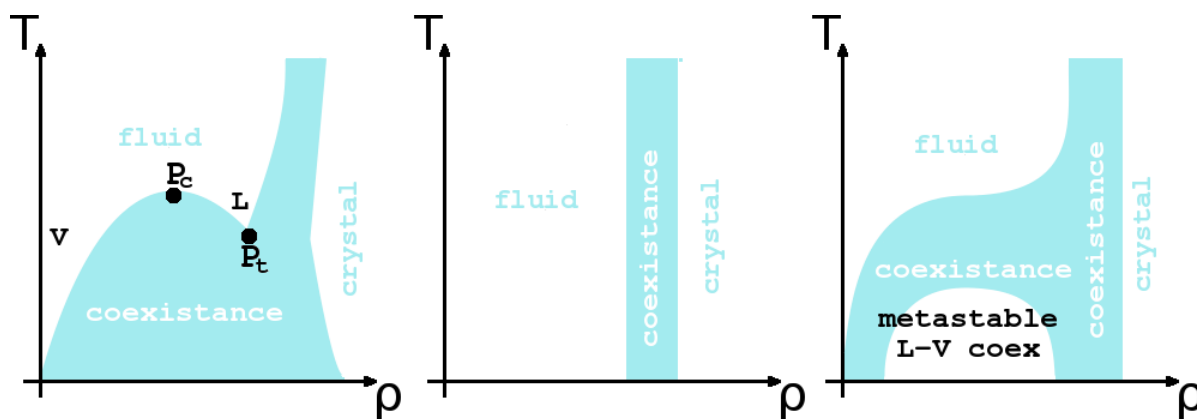
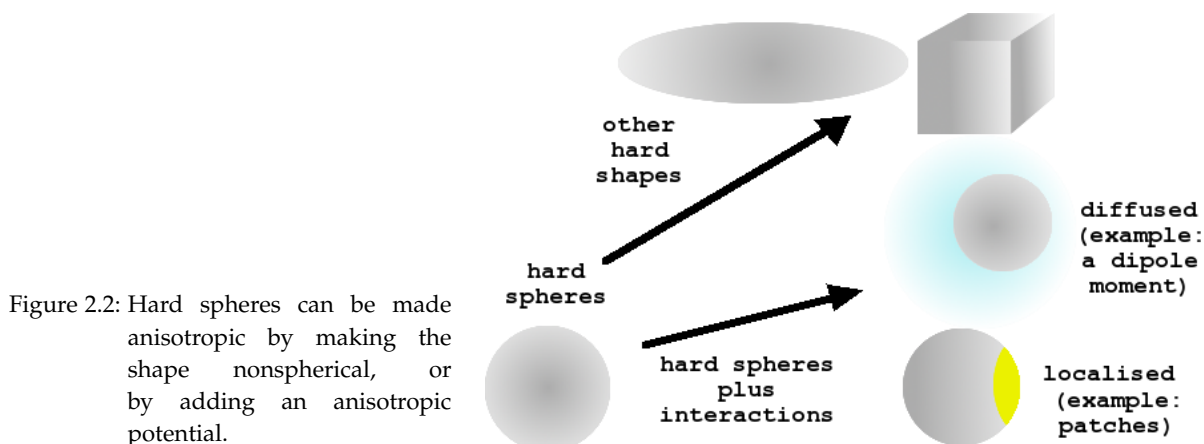


Figure 2.1: Phase diagram of a long-range-interactions substance (left); Hard Spheres (center); HS plus short-ranged attraction (right).

## 2.2 Patchy colloids

The next step after isotropic colloids is to increase complexity by reducing the symmetry of the interactions. Anisotropic particles can be more difficult to manufacture, and require more complex mathematics to deal with the orientations, but at the benefit of a richer phase diagram, featuring new phases that have a larger field of application. Anisotropy in colloidal systems can be introduced in many ways [GS07]. The most obvious one is using *anisometric* (i.e. non-spherical) colloids: particles (i.e. hard non-spherical particles), like cubes [RSI<sup>+</sup>11], ellipsoids [MFV09], octapods [QdGQ<sup>+</sup>12] and more complicated shapes (see figure 2.2). The other way to introduce the anisotropy is via the potential: for example, manufacturing hard spheres with an electric or magnetic dipole moment.

In some cases, the interactions are localized in small regions of the surface. For example, proteins only form bonds at particular spots. Another example are the famous Janus par-



ticles [GJC09, HCLG08], spherical particles that like the roman god have two faces: a rigid one, and an interacting one that can attract the interacting face of another particle. These colloids are fairly easy to manufacture: hard spheres are lined against a wall and sprayed with a chemical. The face that is not protected by the wall gets coated, and becomes attractive, while the other stays rigid. The attractive part of the surface is called a *patch*. The three snapshots in the left half of figure 2.3 show simulation snapshots [SGP09, GLL<sup>+</sup>10] of Janus particles in phases intermediate between the fluid and the FCC crystal seen in hard spheres: micelles and vesicles (top), and “wrinkled” planes (bottom). More complex variants of Janus colloids can be manufactured with more than one patch and different ratios between the attractive surface and the rigid one. Snapshots of a two-patch model are shown in the right half of figure 2.3: lamellae for small patch extension, and planes for larger amplitudes.

This section presented a very small sample of what can be done with patchy colloids, but it should have conveyed the message that anisotropic particles exhibit complex phases that are not present in isotropic systems. Excellent review papers on the subject are [BBL11, PK10, GS07].

### 2.3 Inverse patchy colloids

A different kind of patchy particles was proposed in [BKL11]. These colloids have charged surfaces, but different regions carry charge of different sign: thus, while conventional patchy particles have patches that can attract the patches of other particles, **inverse** patchy particles have patches that repel each other, while attracting the rest of the colloidal surface (see figure 2.4). Because of this peculiarity they are called *inverse patchy colloids* (IPCs).

Although originally developed to describe mesoparticles obtained from the adsorption of charged polyelectrolyte stars onto the surface of oppositely charged colloids, the model works equally well for heterogeneously charged colloids synthesized in the lab [vOHNR15]. In the original paper [BKL11], the authors concentrated on IPCs with two charged, symmetric, polar patches and an oppositely charged equatorial belt. This system was modeled as three equivalent point charges: one for the center, and two for the patches. The interaction potential between two colloids was derived by solving a Debye-Hückel equation, i.e. a Poisson equation where the charge density is assumed proportional to the Boltzmann



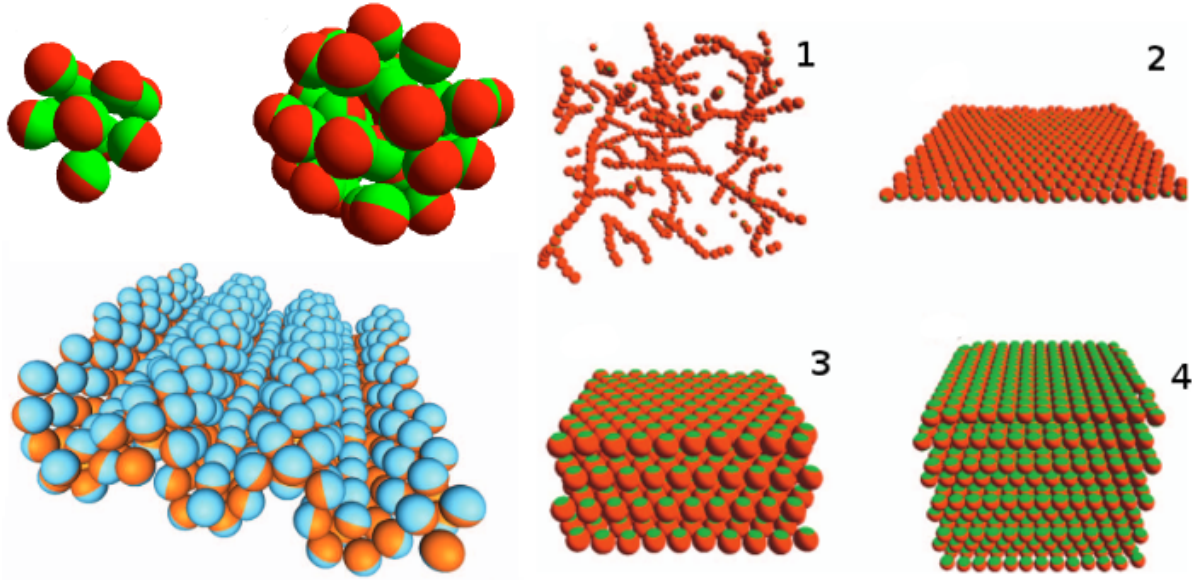


Figure 2.3: Structures obtained via simulations using the the Kern & Frenkel model (a hard sphere with square well interactions between the patches) with a single Janus (50%) patch (figures in the left half) and two patches with different opening angles (right). The one-patch model forms wrinkled solid planes [VPS<sup>+</sup>13], micelles and vesicles [SGP09]; the two-patch model, depending on the patch size, forms lamellae or planes [GLL<sup>+</sup>10].

factor of the potential (the so-called Maxwell-Boltzmann approximation) and the exponential is linearized. The solution was found analytically, as an expansion in Bessel functions and Legendre polynomials. Such a complicated expression is unsuitable for simulations, so the authors also presented a coarse-grained description: a simpler model that preserves all the key physical features. A few years later the model was extended to asymmetrical patches [SBK15].

The coarse-grained model is composed of a hard sphere of radius  $\sigma_C$  carrying three interaction sites. One corresponds to the colloid center, and two to the patch centers; the latter are placed at distances  $e_i$  from the colloid center, in opposite directions (see Figure 2.5). The colloid center carries a charge  $Z_C$ , while the patches have charge  $Z_1$  and  $Z_2$ . The colloid center has an interaction sphere of radius  $\sigma_C + \delta/2$ , where  $\delta$  is the interaction range; the patch interaction spheres have radius  $\sigma_i$ . By construction, for each patch the following relations

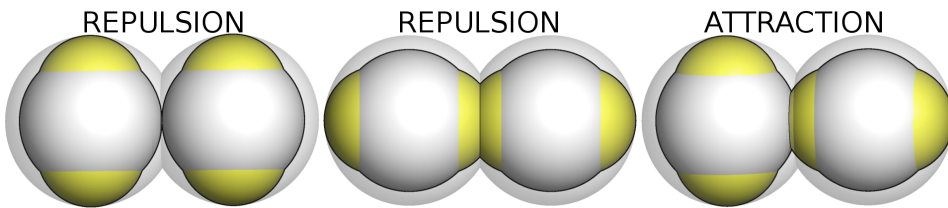


Figure 2.4: Types of interaction of two IPCs along the three main orientations.

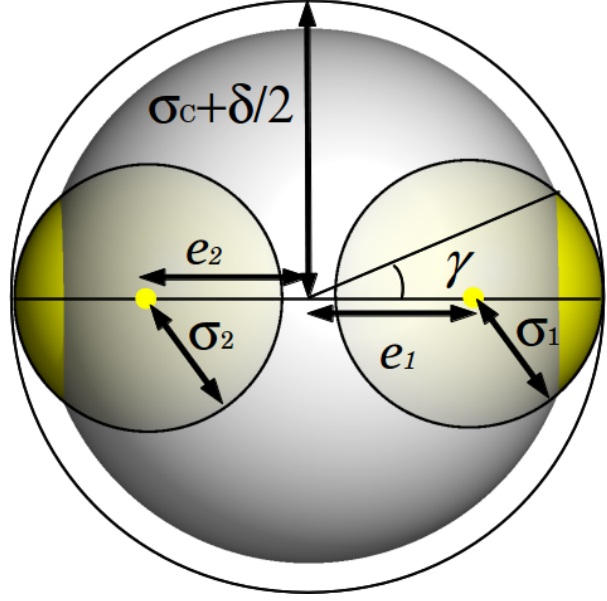


Figure 2.5: IPC cross-section.

hold: [BKL11]

$$\sigma_C + \delta/2 = e_i + \sigma_i \quad \text{and} \quad \cos \gamma_i = \frac{\sigma_C^2 + e_i^2 - \sigma_i^2}{2e_i\sigma_C}, \quad (2.4)$$

where  $\gamma_i$  is half of the opening angle of patch  $i$ , and  $i = 1, 2$ . In addition, the validity of the solution of the Debye-Hückel equation requires that all the sites where the charge is located do not lie outside the colloidal particle, i.e.  $e_i < \sigma_C$ . By virtue of the four constraints represented in equation (2.4), of the eight geometric parameters introduced ( $\sigma_C, \delta, \sigma_i, e_i, \gamma_i$ ) only four are independent (three if the patches are symmetrical).

For two IPCs separated by a center-center distance  $r$  whose orientations are given by the unit vectors  $\hat{\omega}_1$  and  $\hat{\omega}_2$ , the pair interaction is given by [BKL11]

$$U(r, \hat{\omega}_1, \hat{\omega}_2) = \begin{cases} +\infty & \text{if } r < 2\sigma_C \\ \frac{3}{4\pi\sigma_C^3} \sum_{ij} u_{ij} w_{ij}(r, \hat{\omega}_1, \hat{\omega}_2) & \text{if } 2\sigma_C < r < 2\sigma_C + \delta \\ 0 & \text{if } r \geq 2\sigma_C + \delta, \end{cases} \quad (2.5)$$

where  $i$  ( $j$ ) specifies one of the three interaction sites of the first (second) IPC. The  $w_{ij}(r, \hat{\omega}_1, \hat{\omega}_2)$  are the overlap volumes of the corresponding interaction spheres, and the  $u_{ij}$  are the coupling constants quantifying the strength of the  $ij$  interaction. While the  $u_{ij}$  are constants, the  $w_{ij}$  – as well as the potential  $U$  – depend in a complex way on both the inter-particle distance and the relative orientation of the two IPCs; luckily the  $w_{ij}(r, \hat{\omega}_1, \hat{\omega}_2)$  can also be written as simple functions of the site-site (i.e. patch-center, center-center and patch-patch)

distances [BKL11]:

$$w_{ij}(r_{ij}) = \begin{cases} 0 & \text{if } r_{ij} > \sigma_i + \sigma_j \\ \frac{\pi}{3} \left[ \left( 2\sigma_i + \frac{\sigma_i^2 - \sigma_j^2 + r_{ij}^2}{2r_{ij}} \right) \left( \sigma_i - \frac{\sigma_i^2 - \sigma_j^2 + r_{ij}^2}{2r_{ij}} \right)^2 \right] + & \text{if } \sigma_i + \sigma_j > r_{ij} > |\sigma_i - \sigma_j| \\ \frac{\pi}{3} \left[ \left( 2\sigma_j - \frac{\sigma_i^2 - \sigma_j^2 - r_{ij}^2}{2r_{ij}} \right) \left( \sigma_j + \frac{\sigma_i^2 - \sigma_j^2 - r_{ij}^2}{2r_{ij}} \right)^2 \right] & \\ \frac{4\pi}{3} \min(\sigma_i, \sigma_j)^3 & \text{if } r_{ij} < |\sigma_i - \sigma_j| \end{cases} \quad (2.6)$$

Of the nine  $u_{ij}$ , only six are independent:  $u_{CC}, u_{C1}, u_{C2}, u_{11}, u_{22}$  and  $u_{12}$ . For two identical patches they reduce to three,  $u_{CC}, u_{CP}$  and  $u_{PP}$ . In both cases, all the  $u_{ij}$  are fixed using the Debye-Hückel analytical description of the model [BKL11, SBK15], that relates them to macroscopic quantities like the screening of the solution, and to the model-characteristic parameters, i.e. the geometry ( $\sigma_C, \delta, \gamma_i$ ) and the charge distribution ( $Z_C, Z_1$  and  $Z_2$ ).

## 2.4 Studies of IPCs

Shortly after the original paper [BKL11], the same authors presented studies where the IPCs were constrained to two dimensions via both neutral and charged walls [BLK13, BLK14]. Their simulations showed a large number of obtainable phases depending on the model parameters. Various patch sizes and also different charging were investigated: overall neutral systems (total patch charge + central body charge = 0) and overall charged systems (total patch charge + central body charge  $\neq$  0). It was seen that models with a small patch did not form ordered structures, while particles with medium and large patch extensions formed hexagonal structures (see figure 2.6). In most cases, the orientation (defined as the direction that joins the two patches) of the IPCs was confined to the plane, but the model with the largest patch also showed a flower-like arrangement where one of the particles pointing orthogonally to the plane.

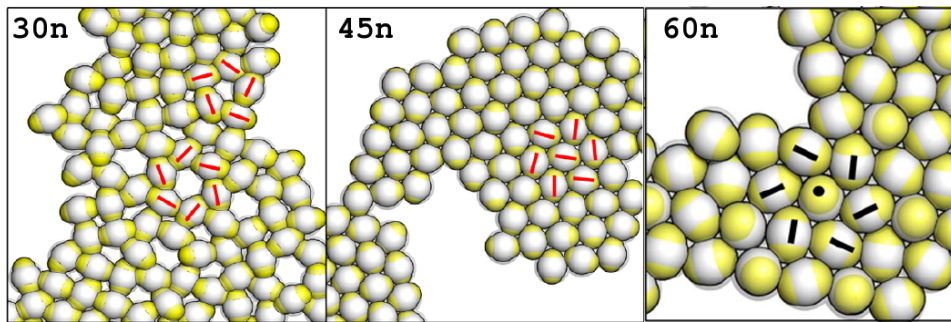


Figure 2.6: 2D IPC structures from [BLK13, BLK14]. The number in the subfigures refers to the model,  $n$  stands for neutral and the number is the  $\gamma$  angle in degrees.

In a successive study [NKD<sup>+</sup>14], the IPCs were studied in three dimension, and a similar structure was found. Particles with a total net charge and two symmetric patches with

$\gamma \simeq 38.6^\circ$  where investigated, and the full phase diagram was explored using a large assortment of techniques (Monte Carlo simulations in  $NpT$  and  $\mu VT$  ensembles, a genetic algorithm, thermodynamic integration, the Einstein molecule approach and direct coexistences). A phase composed by parallel planar layers was observed: the planes had the same hexagonal alignment shown by one of the models presented in [BLK13], the one shown in the center of figure 2.6. Orthogonal views of the three-dimensional lattice are shown in figure 2.7, where it may be noted that the planes are not aligned with each other. A follow-up paper [NB15] studied the stability of this phase with respect to overcharging, patch amplitude, and interaction range.

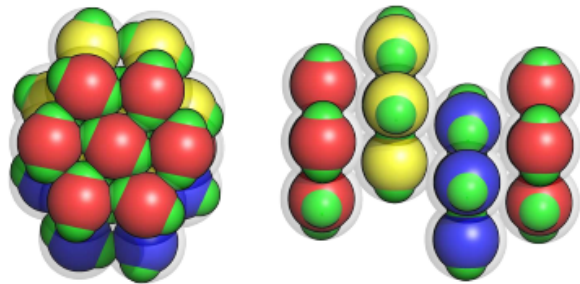


Figure 2.7: The crystalline structure found in reference [NKD<sup>+</sup>14]. The planes have an hexagonal lattice and are parallel but not aligned between themselves.

At the same time, the first experimental studies of IPCs began. In [vOHNR15], silica particles of  $2 \mu m$  of diameter were decorated with patches made of a charged dye; two snapshots are shown in figure 2.8. In this experiment the patches are not symmetric, one being around  $40^\circ$  and the other around  $50^\circ$ .

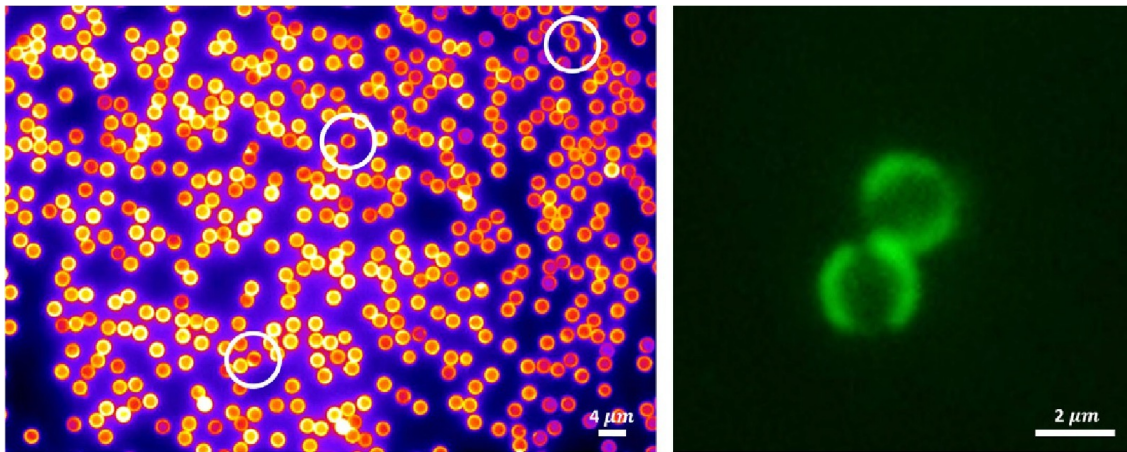


Figure 2.8: (left) Epifluorescence image that shows IPCs aggregation. It is not easy to distinguish the presence of patches, although the aggregation suggests it, since silica would otherwise be repulsive. (right) confocal microscope image of two IPCs, where the patches are more visible and the patch-to-equator alignment is evident. Both pictures come from [vOHNR15].

## 3 The physics behind

“Quando te l’ho chiesto?”

Roberto Marcis

### Contents

---

<b>3.1 Static properties: thermodynamics</b>	<b>22</b>
3.1.1 Ensembles and macrostate	22
3.1.2 Phase diagram and phase transitions	23
<b>3.2 Static properties: structure</b>	<b>25</b>
3.2.1 Reduced distribution function	25
3.2.2 Homogeneous and inhomogeneous systems	27
3.2.3 Pair correlation and static structure factor	29
3.2.4 Further correlation functions, integral equation theories	30
3.2.5 Extension of integral equations to anisotropic particles	32
<b>3.3 Dynamic properties</b>	<b>33</b>
3.3.1 Time-dependent correlation functions	33
3.3.2 Mode coupling theory, solution, non-ergodicity factor	34
<b>3.4 Solution schemes for the theoretical approaches</b>	<b>36</b>
3.4.1 Lado RHNC solution (for the $g(r)$ and the thermodynamics)	36
3.4.2 Barker-Henderson TPT (for the thermodynamics)	38
3.4.3 MCT solution (non-ergodicity factor)	38
<b>3.5 Numerical simulations using molecular dynamics</b>	<b>40</b>
3.5.1 Velocity-Verlet algorithm	40
3.5.2 Adaptation of the potential	40
3.5.3 Adaptation of the algorithm	41

---

While the previous chapter presented the phenomenology and did not need mathematical details, the present one introduces the theoretical framework typical of fluid state theories, based on statistical mechanics and correlation functions. We will go in depth as a standard textbook would; this chapter is meant as a brief summary, and as a quick introduction for an unexperienced reader to the physical tools used in the work. **A reader already familiar with the basics of fluid state theory can skip to subsections 3.4 and 3.5 where implementations are discussed. To ensure ease of reading, these subsections have been kept self-consistent, repeating all the non-standard notations.**

Three types of properties are discussed. *Static* properties are all the features of the system that do not evolve in time. This includes two different but closely related concepts: *thermodynamic* properties and *structural* properties. The former focus at the phase diagram and at equations of state; the latter describe how particles are arranged. *Dynamic* properties are all those quantities that depend on time.

### 3.1 Static properties: thermodynamics

In this section we define what phase transitions are, and why we are interested in them. The present discussion is based on the standard textbooks [Cal85, Pat96, Fer72], from which all the formulas are taken, and to which the reader is referred to for more details.

#### 3.1.1 Ensembles and macrostate

Let us consider a systems composed by  $N$  particles, enclosed in a volume  $V$  and with total energy  $E$ . In theory, it is possible to compute the trajectories of the particles by solving Newton's equations; in practice, since for a macroscopic system  $N = O(10^{23})$ , this task is impossible. Moreover, the single trajectories are of no relevance, because the state of the system can be described by means of experimentally measurable thermodynamic variables like density, temperature or pressure.

Constraining the system to fixed  $E, V$  and  $N$  defines the **microcanonical ensemble**, which is described by means of the entropy,  $S(E, V, N)$ . The triplet  $(E, V, N)$  defines the *macrostate*; each possible configuration of the positions and of the momenta of the particles is called a *microstate*. For every ensemble of  $N$  particles confined in a volume  $V$ , there are many ways to arrange the positions and momenta of the particles in such a way that the total energy is  $E$ ; thus, to each macrostate will correspond a number of microstates,  $\Omega(E, V, N)$ , that is almost always larger than one, and might be very large for some values of  $E$ . The link between the entropy and the micro- and macrostate is given by the famous formula

$$S(E, V, N) = k_B \ln \Omega(E, V, N), \quad (3.1)$$

where  $k_B$  is Boltzmann's constant.

The partial derivatives of the entropy with respect to the thermodynamic variables are called equations of state, and yield the pressure  $p$ , the temperature  $T$  and the chemical potential  $\mu$ :

$$\left. \frac{\partial S}{\partial E} \right|_{VN} = \frac{1}{T}, \quad \left. \frac{\partial S}{\partial V} \right|_{EN} = \frac{p}{T}, \quad \left. \frac{\partial S}{\partial N} \right|_{EV} = -\frac{\mu}{T}. \quad (3.2)$$

Knowledge of these three derivatives and of the three thermodynamic variables is sufficient to reconstruct the entropy, since it can be proven that [Cal85]

$$S(E, V, N) = \frac{E}{T} + \frac{pV}{T} - \frac{\mu N}{T}, \quad (3.3)$$

where  $p$ ,  $\mu$  and  $T$  are all functions of  $E$ ,  $V$  and  $N$ . This relation can also be inverted for the energy, yielding

$$E(S, V, N) = TS - pV + \mu N, \quad (3.4)$$

where  $p$ ,  $\mu$  and  $T$  are now functions of  $S$ ,  $V$  and  $N$ .

Let us now consider a system immersed in a thermal bath<sup>1</sup> with which it exchanges energy in the form of heat. At thermodynamic equilibrium, the system will assume the temperature of the bath, so that the thermodynamic variables will be  $(N, V, T)$ . This setup defines the

<sup>1</sup>See the suggested books for the definition of thermal bath.

**canonical ensemble**, and the thermodynamic potential that describes it is the Helmholtz free energy, linked by a Legendre transform <sup>2</sup> to the energy:

$$F(N, V, T) = E(S, V, N) - TS, \quad (3.5)$$

where  $S = S(N, V, T)$ .

Various other ensembles can be defined, but here we only define the two that will be used in the work. The first is the **isotherm-isobaric**, where the volume is not fixed because the walls of the container are mobile. The system reaches mechanical equilibrium with the surroundings when its pressure is equal to the external one; it is described by the Gibbs free energy, linked to the energy by a double Legendre transform

$$G(N, p, T) = E(S, V, N) - TS + pV(N, p, T), \quad (3.6)$$

where  $S = S(N, p, T)$  and  $V = V(N, p, T)$ . The last is the **grand canonical** ensemble, where the walls do not move but allow exchange of both heat and particles. The flow of particles between the system and its surroundings will stop when the system and the bath reach chemical equilibrium, i.e. when their chemical potentials will be the same. It is described by the grand potential

$$\Omega(\mu, V, T) = E(S, V, N) - TS - \mu N, \quad (3.7)$$

where  $S$  and  $N$  are both functions of  $(\mu, V, T)$ .

Concluding with an interesting side note, the combination of having mobile walls that allow exchange of both energy and particles (a hypothetical  $(\mu, p, T)$  ensemble) makes no sense, because experimentally it would be impossible to distinguish the system from the bath, and applying all the three possible Legendre transforms to the energy gives as a thermodynamic potential

$$E(S, V, N) - TS + pV - \mu N = 0 \quad (3.8)$$

in virtue of equation (3.4).

### 3.1.2 Phase diagram and phase transitions

Even knowing the energy, pressure, and chemical potential for a system at fixed  $N$ ,  $V$  and  $T$ , it is not obvious if the system is found in a liquid, solid or whatever other phase; and “Which phase will the system be found in?”, “What is the extent of this particular phase?” are some of the most interesting questions that can be made, especially from the point of view of applications.

Let us take as an example water in the isothermal-isobaric ensemble. It is pretty obvious that the molecular arrangement is very different between liquid water, vapor and ice. How does the system choose which state is the stable one, at certain pressure and temperature? The Gibbs free energy is well defined in both phases, and for each phase they have a different value; the phase with the lower value is the stable one – for that value of  $(N, p, T)$ ! Figure 3.1 illustrates the point: Gibbs free energy curves for solid, liquid and gas are shown, and the chosen phase at fixed  $T$ ,  $p$  and  $N$  will be the one with the lowest  $G$ .

<sup>2</sup>The general definition of Legendre transform is actually  $F(p) = \inf_x f(x) - px$ . Thermodynamic potentials are assumed to be doubly differentiable and convex functions, thus a sufficient condition is that  $p(x) = f'(x)$ . Assuming that at least locally is possible to invert  $p(x)$ , the Legendre transform becomes  $F(p) = f(x(p)) - px(p)$  with  $x = f'^{-1}(p)$ .

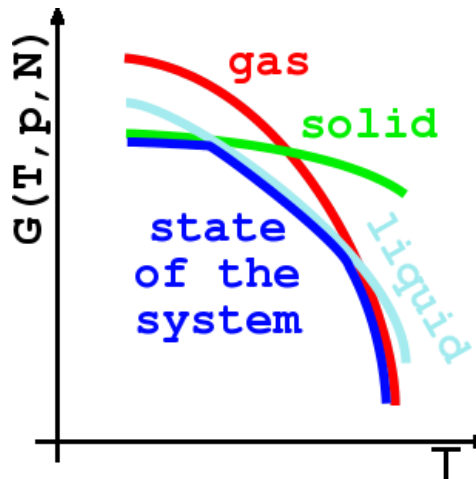


Figure 3.1: Gibbs free energy as a function of temperature for three phases along paths at constant  $p$  and  $N$ .

The information on phases can be collected in the so-called phase diagram. The thermodynamic variables are on the axes, and depending on which ones are used the phase diagram will have a very different look. The most comprehensive ones are three-dimensional plots, but they are difficult both to draw and to visualize, so two-dimensional projections of the three-dimensional representation, where a third variable is kept constant, are the norm. Some examples are shown in figure 3.2.

Pressure-temperature diagrams commonly emerge from experimental data: the pressure is often the atmospheric one, the temperature can be easily manipulated, and the number of particles is assumed constant. The  $p - T$  diagram in the left panel of figure 3.2 shows in blue the three typical transition branches: liquid-solid, liquid-vapor and solid-vapor. Liquid and vapor are structurally indistinguishable, and the only difference is the density. At temperatures and/or pressures higher than the critical ones (signalled in the figure by the critical point  $P_C$ ) the phase transition does not happen anymore. Old textbooks call these region the gas, but in research it is customary to refer to vapor, liquid and gas as a single fluid phase. Most materials have a phase diagram that follows the blue curve in the figure; the red line characterizes an alternative liquid-solid branch for materials (like, for example, water) that can be made liquid by compressing the solid.

Pressure-volume diagrams are the first ones encountered in thermodynamics classes, because the work done at constant temperature by/onto the system – computable as  $\int p dV$  – is portrayable as areas below the isotherms, i.e. the curves at constant temperature depicted in green in the central panel of figure 3.2. The blue curves enclose the coexistence region, where the system will separate into two phases. For example, following the lower isotherm, the system (if initially in the vapor phase) will meet the coexistence region when compressed, and separate; the larger the compression, the more vapor will liquify, until all the system will be found in the liquid phase. The coexistence region around the triple point can be either a smooth minimum (red in figure) or a cusp.

In research, the thermodynamic limit ( $V$  and  $N \rightarrow \infty$ , but  $N/V = \rho$  constant) is assumed. In this case,  $\rho$  takes the place of both  $N$  and  $V$ , and only another variable is needed to specify a statepoint, usually pressure or temperature. Pressure-density diagrams, like the one in the right panel of figure 3.2, are often seen in papers about theoretical methods (integral equa-



tions, perturbation theories... see next sections). Often, theoreticians work in the canonical ensemble, where temperature and density are fixed. When the above-mentioned methods are used to compute phase diagrams, the pressure is computed at single statepoints along isotherms by varying the density; deswegen the results are best presented by drawing these isotherms in a  $p - \rho$  diagram.

Another type of diagram which is frequent in papers is temperature-density.  $T - \rho$  diagrams are practical in presenting results from simulations which were run in the canonical ensemble.

### 3.2 Static properties: structure

In this section we introduce the time-independent spatial correlation functions. All the formulas are quoted from [HM06].

#### 3.2.1 Reduced distribution function

“The partition function is the dream of every theoretician.”

Giorgio Pastore

The simplest Hamiltonian for an  $N$ -body system is composed by the kinetic term plus a pairwise additive isotropic potential:

$$H = K + U = \sum_{i=1}^N \frac{p_i^2}{2m} + \sum_{i=1}^{N-1} \sum_{j=i+1}^N \varphi(x_i, x_j), \quad (3.9)$$

where the  $x_i$  are the positions of the particles and the  $p_i$  are the momenta. In the canonical ensemble, with fixed temperature  $T$  and volume  $V$ , to each possible position-momentum configuration of the  $N$  particles  $\{p, x\}$  can be attributed a probability density function in

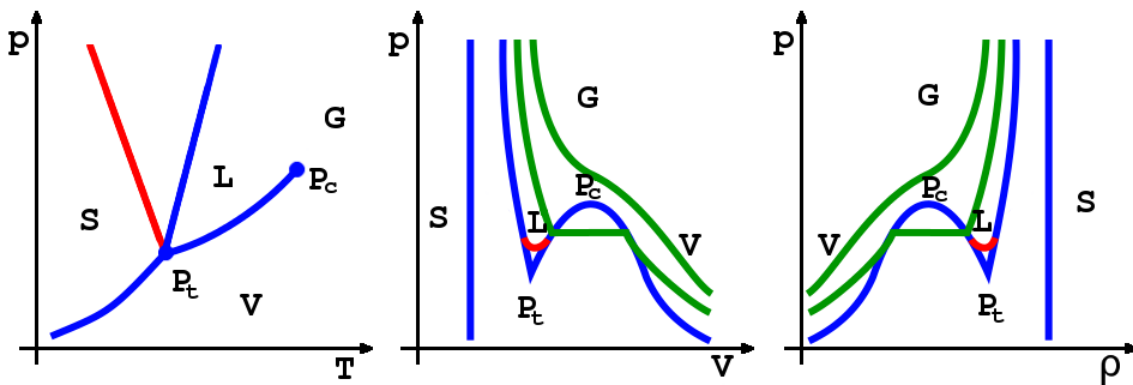


Figure 3.2: Examples of phase diagram:  $p - T$  (left),  $p - \rho$  (center) and  $T - \rho$  (right). S,V,G,L denote the phase: solid, vapor, gas, liquid;  $P_c$  and  $P_t$  the critical and triple point. For the line colors, see the text.

configuration space

$$f(\{\mathbf{p}, \mathbf{x}\}) = \frac{e^{-\beta H(\{\mathbf{p}, \mathbf{x}\})}}{h^{3N} N! Q_N}, \quad (3.10)$$

where  $h$  is the Plack constant and  $Q_N$  is the partition function,

$$Q_N = \int \frac{e^{-\beta H(\{\mathbf{p}, \mathbf{x}\})}}{h^{3N} N!} d^N \mathbf{p} d^N \mathbf{x}, \quad (3.11)$$

the integral of 1 over all the possible microstates (intended, as in the previous sections, as the positions and momenta of all particles) weighted by the Boltzmann factor  $e^{-\beta H(\{\mathbf{p}, \mathbf{x}\})} / h^{3N} N!$ . This quantity was dubbed as a dream, because its knowledge would provide all the possible information on the system. Unfortunately, it is just a dream because it is not possible the compute the extremely complicated integral except for non-mutually-interacting particles.

The probability density function is a very complicated object. To lower the number of variables, we define the reduced (to  $n$ -particles) probability density by integrating away  $n - N$  coordinates:

$$f^{(n)}(\mathbf{p}_1, \mathbf{x}_1, \dots, \mathbf{p}_n, \mathbf{x}_n) = \frac{N!}{(N-n)!} \int f(\{\mathbf{p}, \mathbf{x}\}) d^{N-n} \mathbf{p} d^{N-n} \mathbf{x}. \quad (3.12)$$

Because of the additivity of the kinetic terms, the momenta can be factorized

$$f^{(n)}(\mathbf{p}_1, \mathbf{x}_1, \dots, \mathbf{p}_n, \mathbf{x}_n) = \rho_N^{(n)}(\mathbf{x}_1, \dots, \mathbf{x}_n) \prod_{i=1}^n \frac{e^{-\beta \mathbf{p}_i^2 / 2m}}{(2\pi m k T)^{3/2}}, \quad (3.13)$$

and since their contribution is trivial, they can also be integrated away. The remaining part is called the  $n$ -particles density

$$\rho_N^n(\mathbf{x}_1, \dots, \mathbf{x}_n) = \frac{N!}{(N-n)!} \int \frac{e^{-\beta U(\{\mathbf{x}\})}}{Z_N} d^{N-n} \mathbf{x}, \quad (3.14)$$

where

$$Z_N = \int e^{-\beta U(\{\mathbf{x}\})} d^N \mathbf{x} \quad (3.15)$$

is the reduced partition sum (the letter  $Z$  comes from the german Zustandsumme, literally sum over states). The  $n$ -particles densities rapresent the probability density of finding a particle in the position specified by the arguments. For example,  $\rho_N^{(2)}(\mathbf{x}_1, \mathbf{x}_2) d\mathbf{x}_1 d\mathbf{x}_2$  is the probability to find a particle in the volume  $d\mathbf{x}_1$  around  $\mathbf{x}_1$  and another one in the volume  $d\mathbf{x}_2$  around  $\mathbf{x}_2$ .  $n$ -particles densities are normalized such that

$$\int \rho_N^{(n)}(\mathbf{x}_1, \dots, \mathbf{x}_n) d^n \mathbf{x} = \frac{N!}{(N-n)!}. \quad (3.16)$$

From the  $n$ -particle densities it is possible to define the  $n$ -particles distribution function

$$\boxed{g_N^{(n)}(\mathbf{x}_1, \dots, \mathbf{x}_n) = \frac{\rho_N^{(n)}(\mathbf{x}_1, \dots, \mathbf{x}_n)}{\rho_N^{(1)}(\mathbf{x}_1) \dots \rho_N^{(1)}(\mathbf{x}_n)}}. \quad (3.17)$$

If particles where completely uncorrelated – as in a perfect gas – then the  $n$ -particle densities could be factorized:

$$\rho_N^{(n)}(\mathbf{x}_1, \dots, \mathbf{x}_n) = \prod_{i=1}^n \rho_N^{(1)}(\mathbf{x}_i), \quad (3.18)$$

and the  $g_N^{(n)}(\mathbf{x}_1, \dots, \mathbf{x}_n)$  would be identically one; otherwise, the  $g_N^{(n)}(\mathbf{x}_1, \dots, \mathbf{x}_n)$  signals the deviation from complete uncorrelation. And since the only interaction that does not originate a correlation between the particles is no interaction, the  $n$ -particles distribution function measures the deviation from a perfect gas. Two equations of state can be written in terms of the  $g_N^{(n)}(\mathbf{x}_1, \dots, \mathbf{x}_n)$ : the excess energy per particle

$$u_{xc} = \frac{1}{2} \int g_N^{(2)}(\mathbf{x}_1, \mathbf{x}_2) \rho_N^{(1)}(\mathbf{x}_1) \rho_N^{(1)}(\mathbf{x}_2) \varphi(r_{12}) d\mathbf{x}_1 d\mathbf{x}_2 \quad (3.19)$$

and the virial pressure

$$p = \rho kT - \frac{1}{6} \int g_N^{(2)}(\mathbf{x}_1, \mathbf{x}_2) \rho_N^{(1)}(\mathbf{x}_1) \rho_N^{(1)}(\mathbf{x}_2) \mathbf{x}_1 \cdot \nabla_1 \varphi(r_{12}) d\mathbf{x}_1 d\mathbf{x}_2. \quad (3.20)$$

Before ending this subsection, we introduce a compact notation for the ensemble average,

$$\langle \dots \rangle = \int \dots \frac{e^{-\beta U(\{\mathbf{x}\})}}{Z_N} d^{N-n} \mathbf{x}, \quad (3.21)$$

and two identities (that can be proven by direct evaluation) that will be of use in the next section. Denoting with  $\delta(\mathbf{x})$  the three-dimensional Dirac delta:

$$\rho_N^{(1)}(\mathbf{x}) = \left\langle \sum_{i=1}^N \delta(\mathbf{x} - \mathbf{x}_i) \right\rangle, \quad (3.22)$$

and

$$\rho_N^{(2)}(\mathbf{x}, \mathbf{y}) = \left\langle \sum_{i=1}^N \sum_{j \neq i}^N \delta(\mathbf{x} - \mathbf{x}_i) \delta(\mathbf{y} - \mathbf{x}_j) \right\rangle. \quad (3.23)$$

### 3.2.2 Homogeneous and inhomogeneous systems

The 1- and 2-particles densities (and distribution functions) have respectively 3 and 6 arguments. To further simplify them we will consider homogeneous and isotropic systems. *Inhomogeneous* and *anisotropic* systems may have walls or other obstacles, be subject to external fields, or have a crystalline structure where the density is very irregular: to describe these kind of systems, all the arguments are necessary. Instead, in a pure unordered phase and far from the surface, the  $n$ -particle densities and distribution functions vary smoothly, and depend only on  $|\mathbf{x}_1 - \mathbf{x}_2|$  whenever the potential also does. The equilibrium (i.e. the ensemble- or time-averaged) single particle density is constant,

$$\rho_N^{(1)}(\mathbf{x}) = N/V = \rho, \quad (3.24)$$

which greatly simplifies equation (3.17):

$$\rho^{(n)} g_N^{(n)}(\mathbf{x}_1, \dots, \mathbf{x}_n) = \rho^n(\mathbf{x}_1, \dots, \mathbf{x}_n). \quad (3.25)$$

Of course, no real system is truly homogeneous, because in real systems there will always be walls; but as long as surfaces effects can be neglected, experiments can study the bulk behaviour of large samples, and calculations can use the thermodynamic limit.

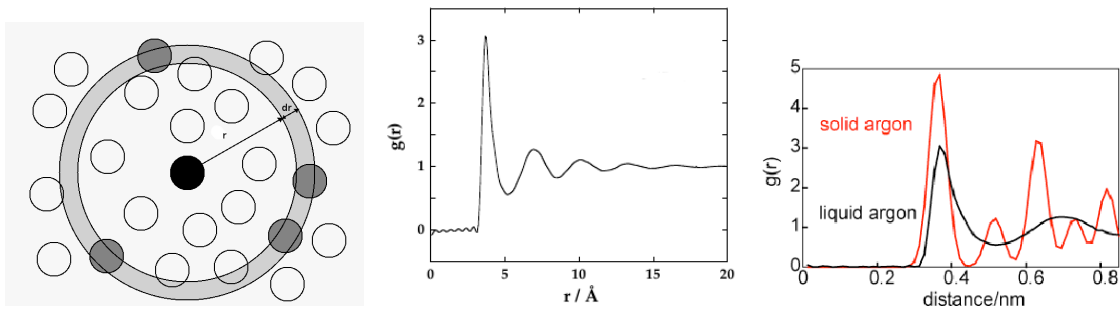
Assuming homogeneity and isotropy, we use the change of variable  $\mathbf{x}_2 = \mathbf{x}_1 + \mathbf{r}$  to introduce the relative position of two particles  $\mathbf{r}$ , and the absolute positions can be integrated out from the 2-particles distribution function  $g_N^{(2)}(\mathbf{x}, \mathbf{x} + \mathbf{r})$ :<sup>3</sup>

$$\frac{1}{V} \int g_N^{(2)}(\mathbf{x}, \mathbf{x} + \mathbf{r}) d\mathbf{x} = g(\mathbf{r}) = g(r). \quad (3.26)$$

The  $g(r)$  is called the radial distribution function, depends only on the radial distance under the assumption of anisotropy, and it is normalized so that

$$\rho \int g(r) 4\pi r^2 dr = N - 1. \quad (3.27)$$

The  $g(r)$  can be interpreted as the conditional probability density that, having a particle in the origin, another will be found at distance  $r$ ; thus,  $\rho g(r) 4\pi r^2 dr$  is the number of particles located in a spherical shell of thickness  $dr$  at distance  $r$  from the particle in the origin. This interpretation can be better understood by looking at figure 3.3(a).



(a) Given a particle in the origin, the number of different particles in the spherical shell at distance  $r$  and thick  $dr$  is  $\rho g(r) 4\pi r^2 dr$ . (b)  $g(r)$  from scattering experiments on liquid Argon at 85 K. The ripples near zero are artifacts due to a Fourier transform. (c) Comparison of the  $g(r)$  of Argon in the solid and the liquid phase. From [HM06].

Figure 3.3:  $g(r)$ , explanation and example

In figure 3.3(b) a typical liquid  $g(r)$  obtained from experiments is shown: at small distance it goes to zero because of Pauli repulsion, while at large distances converges to unity, signalling loss of correlation. This is a general fact: it can be proved analytically that

$$g(r) \xrightarrow{r \rightarrow \infty} 1 - 1/N. \quad (3.28)$$

The peaks at intermediate distance, instead, characterize the structure. Figure 3.3(c) shows a comparison of the  $g(r)$  of Argon in the solid and the liquid phase. Liquid Argon has essentially no structure, and this is reflected in the absence of remarkable features in the plot; on the other hand, the  $g(r)$  of solid Argon has very pronounced peaks and valleys, revealing the presence of a rigid structure with ordered neighbours and vacancies.

We conclude the section with some equations that will be used in the implementation of the theoretical methods. The equations of state shown in the previous section are greatly

<sup>3</sup>Many papers skip the integration and define  $g(r) = g_N^{(2)}(|\mathbf{x}_1 - \mathbf{x}_2|)$ ; this is obviously equivalent, although not rigorous. See [HM06].

simplified in terms of the  $g(r)$ :

$$u_{xc} = \frac{\rho}{2} \int_0^\infty g(r) \varphi(r) 4\pi r^2 dr, \quad (3.29)$$

$$p = \rho kT - \frac{\rho^2}{6} \int_0^\infty \frac{\partial \varphi(r)}{\partial r} g(r) 4\pi r^3 dr. \quad (3.30)$$

Another useful identity can be derived using equation (3.23):

$$\begin{aligned} \frac{1}{V} \int g_N^{(2)}(\mathbf{x}, \mathbf{x} + \mathbf{r}) d\mathbf{x} &= \frac{1}{V\rho^2} \int \rho_N^{(2)}(\mathbf{x}, \mathbf{x} + \mathbf{r}) d\mathbf{x} \\ &= \frac{1}{\rho N} \left\langle \sum_{i=1}^N \sum_{j \neq i}^N \int \delta(\mathbf{x} - \mathbf{x}_i) \delta(\mathbf{x} + \mathbf{r} - \mathbf{x}_j) d\mathbf{x} \right\rangle \\ &= \frac{1}{\rho N} \left\langle \sum_{i=1}^N \sum_{j \neq i}^N \delta(\mathbf{r} - [\mathbf{x}_j - \mathbf{x}_i]) \right\rangle = g(r). \end{aligned} \quad (3.31)$$

The last line can be used, together with the physical interpretation (*that*  $\rho g(r) 4\pi r^2 dr$  is the number of particles located in a spherical shell of thickness  $dr$  at distance  $r$  from the particle in the origin), to compute the pair distribution function from simulations:

$$\rho g(r) = \left\langle \frac{\text{number of couples in } (r - dr/2, r + dr/2)}{N 4\pi r^2 dr} \right\rangle. \quad (3.32)$$

### 3.2.3 Pair correlation and static structure factor

The pair distribution function has the problem that it does not converge to zero at infinity. For later convenience, the pair correlation function is defined as

$$g_N^{(2)}(\mathbf{x}_1, \mathbf{x}_2) - 1 = h_N^{(2)}(\mathbf{x}_1, \mathbf{x}_2); \quad (3.33)$$

in a homogeneous system this relation is simply  $h(r) = g(r) - 1$ .

Another important and closely related quantity is the static structure factor (SSF)

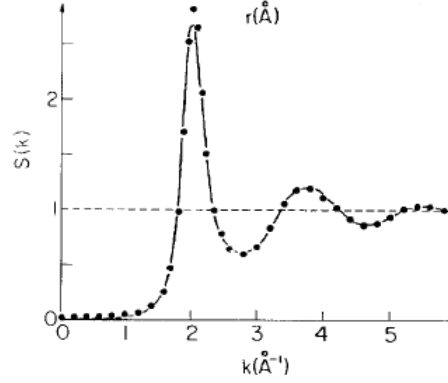
$$S(\mathbf{k}) = 1 + \rho \hat{g}(\mathbf{k}) = 1 + \rho 8\pi^3 \delta(\mathbf{k}) + \rho \hat{h}(\mathbf{k}) \quad (3.34)$$

where the hat denotes a Fourier transform. The SSF is experimentally measurable in elastic scattering experiments with neutrons or X-rays, via the differential cross section per unit solid angle  $\Omega$

$$\frac{d\sigma}{d\Omega}(\mathbf{k}) = N(B_i + B_c S(\mathbf{k})), \quad (3.35)$$

where  $B_i$  and  $B_c$  are called the coherent and incoherent mean squared diffusion lengths, which typically depend on the type of material but not on the shape of the sample; the size of the sample only enters the equation through the number of particles in the sample  $N$ . The delta contribution in formula 3.34 represents the particles that emerge from the sample unscattered. Mathematically, it is due to the  $g(r)$  not converging to zero at  $r \rightarrow \infty$ . The introduction of  $h(r)$  helps making this evident.

Figure 3.4: Liquid Sodium SSF. The dots are from experiment, the line is a Monte Carlo simulation with isotropic potentials  $\propto r^{-4}$ . Adapted from [Cac96].



Using formula 3.22 it can be also proven that

$$S(\mathbf{k}) = \left\langle \frac{\hat{\rho}(\mathbf{k})\hat{\rho}(-\mathbf{k})}{N} \right\rangle. \quad (3.36)$$

where

$$\hat{\rho}(\mathbf{k}) = \sum_{i=1}^N e^{-i\mathbf{k}\cdot\mathbf{x}_i} \quad (3.37)$$

is the Fourier transform of equation (3.22).

Figure 3.4 shows a comparison of experimental and simulation results, where we can observe the typical shape of the SSF in the fluid phase: a large main peak, a decay to unity at large  $k$ , and a small but nonzero value at  $k = 0$ . The main peak of the SSF is usually found at  $2\pi/a$ , where  $a$  is the typical particle-particle separation; other peaks at smaller  $k$  denote structures of periodicity larger than  $a$ .  $S(0)$  is a very important value, because it can be proved that

$$S(0) = \rho k_B T \chi_T, \quad (3.38)$$

where  $\chi_T$  is the isothermal compressibility of the system,

$$\chi_T = -\frac{1}{V} \left. \frac{\partial V}{\partial p} \right|_T. \quad (3.39)$$

During an isothermal phase transition (see figure 3.2, central panel), a finite change in volume does not induce any change in pressure: the compressibility diverges, and consequently so does the zero value of the SSF.

### 3.2.4 Further correlation functions, integral equation theories

The direct correlation function  $c(\mathbf{x}_1, \mathbf{x}_2)$  is often defined by postulating the Ornstein-Zernike (OZ) equation [HM06]

$$h_N^{(2)}(\mathbf{x}_1, \mathbf{x}_2) = c_N^{(2)}(\mathbf{x}_1, \mathbf{x}_2) + \int c_N^{(2)}(\mathbf{x}_1, \mathbf{y}) \rho_N^{(1)}(\mathbf{y}) h_N^{(2)}(\mathbf{y}, \mathbf{x}_2) d\mathbf{y}, \quad (3.40)$$

but a more accurate density functional treatment (found for example in [HM06]) would first introduce the  $c_N^{(2)}(\mathbf{x}_1, \mathbf{x}_2)$  as the linear response of the free energy functional to density fluctuations and deduce equation (3.40) from it.

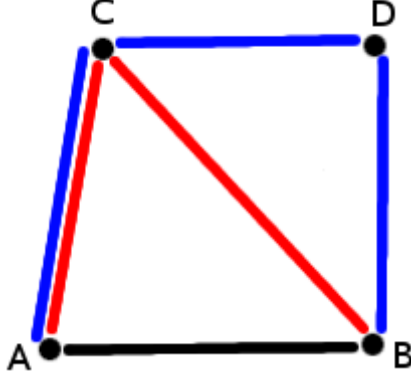


Figure 3.5: Direct action of A on B in black; indirect action in color – see equation (3.42).

The physical meaning of the OZ equation is very important: the total correlation ( $h$ ) between two particles is given partially by the direct interaction between the two ( $c$ ), and partially by the indirect interaction that these particles have through the other particles in the system. Denoting the convolution with the symbol  $\otimes$ , the OZ equation reads

$$h = c + \rho c \otimes h \quad (3.41)$$

which can be formally expanded as

$$h = c + c \otimes \rho c + c \otimes \rho c \otimes \rho c + \dots \quad (3.42)$$

where the colors refer to the lines in figure 3.5. The first term ( $c$ ) accounts for the direct interaction between particles A and B, the second term ( $\rho c \otimes c$ ) stands for the interaction that a third particle, C, exerts on B by being influenced by A, the third term ( $\rho^2 c \otimes c \otimes c$ ) would include fourth particle, D, and so on. The OZ equation ensures that the full indirect action is taken into account.

The convolution part of equation (3.40) is usually termed the indirect (or series) correlation function

$$\gamma_N^{(2)}(\mathbf{x}_1, \mathbf{x}_2) = h_N^{(2)}(\mathbf{x}_1, \mathbf{x}_2) - c_N^{(2)}(\mathbf{x}_1, \mathbf{x}_2) = \int c_N^{(2)}(\mathbf{x}_1, \mathbf{y}) \rho_N^{(1)}(\mathbf{y}) h_N^{(2)}(\mathbf{y}, \mathbf{x}_2) d\mathbf{y}. \quad (3.43)$$

We have introduced four correlation functions,  $g_N^{(2)}(\mathbf{x}_1, \mathbf{x}_2)$ ,  $h_N^{(2)}(\mathbf{x}_1, \mathbf{x}_2)$ ,  $c_N^{(2)}(\mathbf{x}_1, \mathbf{x}_2)$  and  $\gamma_N^{(2)}(\mathbf{x}_1, \mathbf{x}_2)$ , but since  $g_N^{(2)}(\mathbf{x}_1, \mathbf{x}_2) - 1 = h_N^{(2)}(\mathbf{x}_1, \mathbf{x}_2)$  and  $\gamma_N^{(2)}(\mathbf{x}_1, \mathbf{x}_2) = h_N^{(2)}(\mathbf{x}_1, \mathbf{x}_2) - c_N^{(2)}(\mathbf{x}_1, \mathbf{x}_2)$ , only two are independent. To solve for two unknowns, two equations are needed: the first is the OZ, (3.40), while the second, appropriately called closure equation, reads [HM06]

$$g_N^{(2)}(\mathbf{x}_1, \mathbf{x}_2) = e^{-\beta \varphi(\mathbf{x}_1, \mathbf{x}_2) + \gamma_N^{(2)}(\mathbf{x}_1, \mathbf{x}_2) + B(\mathbf{x}_1, \mathbf{x}_2)}, \quad (3.44)$$

where  $\varphi(\mathbf{x}_1, \mathbf{x}_2)$  is the two-body potential, and  $\beta = 1/k_b T$ .  $B(\mathbf{x}_1, \mathbf{x}_2)$ , called the bridge function, can be derived in a density functional theory (found for example in [HM06]) as a complicated functional of the pair distribution function.<sup>4</sup> As with the partition function, it

<sup>4</sup>As an historical digression, it is interesting to note that the names bridge and series function come from the diagrammatic expansion of the logarithm of the cavity function. Three types of diagram are involved: the terms that involve disconnected diagrams, which look like electrical circuits in parallel, sum to zero; the terms that look like electrical circuits in series sum to  $\gamma(\mathbf{x}_1, \mathbf{x}_2)$ ; the terms that look like Wheatstone bridges sum to  $B(\mathbf{x}_1, \mathbf{x}_2)$ . This is where the apparently strange names come from.

is impossible to compute  $B(\mathbf{x}_1, \mathbf{x}_2)$  exactly, so approximations are needed. The first approximation to the closure equation was proposed in 1958 by Percus and Yevick, and reads

$$g_N^{(2)}(\mathbf{x}_1, \mathbf{x}_2) = e^{-\beta\varphi(\mathbf{x}_1, \mathbf{x}_2)} \gamma_N^{(2)}(\mathbf{x}_1, \mathbf{x}_2), \quad (3.45)$$

which corresponds to the choice  $B(\mathbf{x}_1, \mathbf{x}_2) = \gamma_N^{(2)}(\mathbf{x}_1, \mathbf{x}_2) + \ln \gamma_N^{(2)}(\mathbf{x}_1, \mathbf{x}_2)$ ; the second, proposed two years later, is called hypernetted chain closure (HNC) and sets the bridge function to zero:

$$g_N^{(2)}(\mathbf{x}_1, \mathbf{x}_2) = e^{-\beta\varphi(\mathbf{x}_1, \mathbf{x}_2) + \gamma_N^{(2)}(\mathbf{x}_1, \mathbf{x}_2)}. \quad (3.46)$$

Not strictly needed in theory, but useful in practical calculations, is the cavity function

$$y(\mathbf{x}_1, \mathbf{x}_2) = g_N^{(2)}(\mathbf{x}_1, \mathbf{x}_2) e^{\beta\varphi(\mathbf{x}_1, \mathbf{x}_2)} = e^{\gamma_N^{(2)}(\mathbf{x}_1, \mathbf{x}_2) + B(\mathbf{x}_1, \mathbf{x}_2)}. \quad (3.47)$$

By direct substitution in (3.17) and (3.14) it can be shown that the cavity function is the pair distribution function of pair of particles that do not interact with each other, while interacting with all the other particles of the system. The name cavity stems from hard spheres, for which two noninteracting particles can be seen as compenetrable cavities. The introduction of  $y(\mathbf{x}_1, \mathbf{x}_2)$  is justified by the fact that at very short distances the pair distribution function goes to zero while the potential diverges. The cavity function is instead finite in this region.

In the homogeneous case, the OZ and closure equations greatly simplify:

$$h(r) = c(r) + \rho \int c(|\mathbf{r} - \mathbf{y}|) h(|\mathbf{y}|) d\mathbf{y}, \quad (3.48)$$

$$g(r) = e^{-\beta\varphi(r) + \gamma(r) + B(r)}. \quad (3.49)$$

### 3.2.5 Extension of integral equations to anisotropic particles

When particles are not spherical, the distribution functions have to take into account the orientations  $\hat{\omega}_i$ , which in general need to be specified by three angles. In case of particles with a cylindrical or axial symmetry, the orientation of a particle can be defined as the direction of the symmetry axis, and specified with only two angles. For the IPCs, this is the line joining the center of the two patches. In an anisotropic (no external fields) and homogeneous (no walls and phase transitions) system, the two-particle correlation functions for IPCs depend only on the mutual center-center distance  $r$ , the two angles between the vector joining the center of mass ( $\mathbf{r}$ ) and the orientations of the particles,  $\theta_1$  and  $\theta_2$ , and the relative angle between to particles  $\phi = \phi_2 - \phi_1$  in the plane orthogonal to  $\mathbf{r}$ .

The OZ equation, modified to take orientations into account, reads

$$\boxed{h(r_{12}, \hat{\omega}_1, \hat{\omega}_2) = c(r_{12}, \hat{\omega}_1, \hat{\omega}_2) + \frac{\rho}{4\pi} \int c(r_{13}, \hat{\omega}_1, \hat{\omega}_3) h(r_{32}, \hat{\omega}_3, \hat{\omega}_2) dr_3 d\hat{\omega}_3.} \quad (3.50)$$

It is called the molecular OZ (MOZ) equation, and features a convolution in five variables. The closure equation changes minimally:

$$\boxed{g(r, \hat{\omega}_1, \hat{\omega}_2) = e^{-\beta\varphi(r, \hat{\omega}_1, \hat{\omega}_2) + \gamma(r, \hat{\omega}_1, \hat{\omega}_2) + B(r, \hat{\omega}_1, \hat{\omega}_2).} \quad (3.51)$$



### 3.3 Dynamic properties

#### 3.3.1 Time-dependent correlation functions

Time-dependent correlation functions are frequently used in many fields of physics, engineering and even economy. They are typically defined as

$$\langle A(t' + t)B(t') \rangle, \quad (3.52)$$

where  $A$  and  $B$  are two generic time-dependent functions, and  $\langle \dots \rangle$  denotes an ensemble average. At thermodynamic equilibrium, the correlation functions do not depend on the absolute time,  $t'$ , but only on the time difference between the arguments,  $t$ , so that they are more frequently defined as

$$\langle A(t)B(0) \rangle. \quad (3.53)$$

A correlation function for which  $A = B$  is called an autocorrelation function.

In this work we will use the normalized autocorrelation function of the velocity  $\mathbf{v}(t)$

$$c_v(t) = \left\langle \frac{\mathbf{v}(t) \cdot \mathbf{v}(0)}{\mathbf{v}(0) \cdot \mathbf{v}(0)} \right\rangle, \quad (3.54)$$

the autocorrelation function (automatically normalized) of the orientation  $\hat{\mathbf{n}}(t)$

$$c_n(t) = \langle \hat{\mathbf{n}}(t) \cdot \hat{\mathbf{n}}(0) \rangle, \quad (3.55)$$

and the mean squared displacement (MSD)

$$\Delta \mathbf{x}^2(t) = \langle [\mathbf{x}(t) - \mathbf{x}(0)]^2 \rangle, \quad (3.56)$$

where  $\mathbf{x}(t)$  is the trajectory of a particle. Via the MSD we also implicitly define the diffusion coefficient  $D$  as

$$\Delta \mathbf{x}^2(t) = 2dDt, \quad (3.57)$$

in the limit of  $t \rightarrow \infty$ .  $d$  is the dimension of the space, thus we would have  $4Dt$  in two dimension,  $6Dt$  in three and so on.

The spatial correlation functions introduced in the previous sections (such as  $g(r)$  and  $S(k)$ ) can be extended to describe time-dependent observables. The extension of the  $g(r)$  is the Van Hove function  $G(\mathbf{x}, t)$ , defined as [HM06]

$$G(\mathbf{x}, t) = \frac{1}{N} \left\langle \sum_{i=1}^N \sum_{j=1}^N \delta(\mathbf{x} - \mathbf{x}_j(t) + \mathbf{x}_i(0)) \right\rangle. \quad (3.58)$$

The Van Hove function can be seen as a density autocorrelation:

$$\begin{aligned} G(\mathbf{x}, t) &= \frac{1}{N} \left\langle \sum_{i=1}^N \sum_{j=1}^N \int \delta(\mathbf{x} + \mathbf{y} - \mathbf{x}_j(t)) \delta(\mathbf{y} - \mathbf{x}_i(0)) d\mathbf{y} \right\rangle \\ &= \frac{1}{N} \left\langle \int \rho(\mathbf{x} + \mathbf{y}, t) \rho(\mathbf{y}, 0) d\mathbf{y} \right\rangle = \frac{1}{\rho} \langle \rho(\mathbf{x}, t) \rho(\mathbf{0}, 0) \rangle \end{aligned} \quad (3.59)$$

where

$$\rho(\mathbf{x}, t) = \sum_{i=1}^N \delta(\mathbf{x} - \mathbf{x}_i(t)) \quad (3.60)$$

is the obvious time-dependent extension of (3.22). The  $G(\mathbf{x}, t)$  can be written as the sum of two parts: a self part,

$$G_s(\mathbf{x}, t) = \frac{1}{N} \left\langle \sum_{i=1}^N \delta(\mathbf{x} - \mathbf{x}_i(t) + \mathbf{x}_i(0)) \right\rangle, \quad (3.61)$$

that accounts for the diffusion of single particle, satisfying the  $t = 0$  condition  $G_s(\mathbf{x}, 0) = \delta(\mathbf{x})$ ; and a distinct part,

$$G_d(\mathbf{x}, t) = \frac{1}{N} \left\langle \sum_{i=1}^N \sum_{i \neq j}^N \delta(\mathbf{x} - \mathbf{x}_j(t) + \mathbf{x}_i(0)) \right\rangle, \quad (3.62)$$

that correlates the actual position of a particle with the position that other particles at the initial times, and whose  $t = 0$  condition is  $G_d(\mathbf{x}, 0) = \rho g(\mathbf{x})$ .

Switching to Fourier space, equation (3.60) becomes

$$\hat{\rho}(\mathbf{k}, t) = \sum_i^N e^{i\mathbf{k} \cdot \mathbf{x}_i(t)} \quad (3.63)$$

and can be used to generalize the static structure factor  $S(\mathbf{k})$  (3.36):

$$F(\mathbf{k}, t) = \left\langle \frac{\hat{\rho}(\mathbf{k}, t) \hat{\rho}(-\mathbf{k}, 0)}{N} \right\rangle. \quad (3.64)$$

This quantity, the autocorrelation of  $\rho(\mathbf{k}, t)/\sqrt{N}$ , is called the intermediate scattering function (ISF); by definition  $F(\mathbf{k}, 0) = S(\mathbf{k})$ . Comparing equation (3.59) and (3.64), one can see that the  $F(\mathbf{k}, t)$  and the Van Hove function are closely related; in fact, they are the spatial Fourier transform of each other [HM06]. The inverse time Fourier transform of the  $F(\mathbf{k}, t)$  is called the dynamic structure factor [HM06]

$$S(\mathbf{k}, \omega) = \frac{1}{2\pi} \int F(\mathbf{k}, t) e^{i\omega t} dt, \quad (3.65)$$

and can be measured in inelastic scattering experiments, via its relation to the scattering cross section:

$$\frac{d^2\sigma}{d\Omega d\omega} = N b^2 \frac{k_i}{k_s} S(\mathbf{k}, \omega) \quad (3.66)$$

where  $\Omega$  is the scattering solid angle,  $b^2$  is the the mean squared scattering length,  $k_i$  is the wave vector of the incident particle, and  $k_s$  of the scattered particle.

### 3.3.2 Mode coupling theory, solution, non-ergodicity factor

The time evolution of a generic autocorrelation function  $f(t)$  can be predict by integration of the Zwanzig-Mori (ZM) equation [KB11, Göt09]

$$f''(t) + \Omega^2 f(t) + \Omega^2 \int_0^{+\infty} M_f(t - \tau) f'(\tau) d\tau = 0; \quad (3.67)$$

here, the primes denote time derivatives,  $\Omega^2$  (not to be confused with the solid angle in the previous §) is a constant characterizing the function  $f$ , and the memory kernel  $M_f(t)$  has been introduced.<sup>5</sup> The careful reader will recognize (3.67) as the equation of motion of an harmonic oscillator onto which a time-retarded force  $\Omega^2 M_f(t)$  is applied. The ZM equation is exact, but the memory kernel is unknown in an exact, closed form; nevertheless, many approximated expressions have been proposed, among which we use the so-called Mode Coupling Theory (MCT).

The MCT approach can be applied to different types of correlation functions; we are interested in applying it to intermediate scattering function (ISF) introduced in the previous paragraph,

$$F(\mathbf{q}, t) = \frac{1}{N} \sum_i^N \langle e^{i\mathbf{q} \cdot \mathbf{x}_i(t)} e^{-i\mathbf{q} \cdot \mathbf{x}_i(0)} \rangle, \quad (3.68)$$

whose  $t = 0$  value,  $F(\mathbf{q}, 0) = S(\mathbf{q})$ , is the static structure factor (SSF). In what follows, homogeneity and isotropy of the fluid will be assumed, so that  $F(\mathbf{q}, t) = F(q, t)$  and  $S(\mathbf{q}) = S(q)$ . Each mode<sup>6</sup> of the ISF will satisfy its own ZM equation with its own memory function  $M(q, t)$  and its own constant  $\Omega^2(q)$ , so that in general

$$F''(q, t) + \Omega^2(q)F(q, t) + \Omega^2(q) \int_0^{+\infty} M(q, t - \tau) F'(q, \tau) d\tau = 0, \quad (3.69)$$

holds. It can be shown [HM06, KB11, Göt09] that  $\Omega^2(q) = k_B T q^2 / m S(q)$ , with  $m$  the mass of the particles. It was proposed by Götze [KB11, Göt09] to write the memory function in terms of the ISF as

$$M(q, t) = v(q)M_r(t) + \frac{\rho S(q)}{16\pi^3 q^4} \int_{\mathbb{R}^3} F(\mathbf{k}, t) F(|\mathbf{q} - \mathbf{k}|, t) \left[ (\mathbf{q} \cdot \mathbf{k}) c(k) + \mathbf{q} \cdot (\mathbf{q} - \mathbf{k}) c(|\mathbf{q} - \mathbf{k}|) \right]^2 d\mathbf{k}, \quad (3.70)$$

where  $c(q) = \rho^{-1}(1 - 1/S(q))$  is the direct correlation function, introduced in § 3.2.4. The first term,  $v(q)M_r(t)$ , in which  $t$ - and  $q$ -dependence are factorized, is called the regular part [KB11, Göt09], and is only important in fluid phases in which there is no dynamic arrest. Its exact shape is a very thin peak around  $t = 0$ , and on the much larger timescale of arrested states (gels, glasses) it can often be neglected [Kra07]. On the other hand, the part with the complicated integral vanishes in ergodic states but is very important for arrested states [KB11].

Together with the initial conditions  $F(k, 0) = S(q)$  and  $F'(q, 0) = 0$  [Kra07], equations (3.69) and (3.70) can be numerically solved with a self-consistent procedure. Unfortunately, the solution of the time-dependent MCT equations is very complicated. However, the  $F(q, t)$  carries a lot of information that might not be wanted. If the system is ergodic,  $F(q, t)$  will eventually decay to zero for all values of  $q$ ; if it does not, the limit function

$$f(q) = \lim_{t \rightarrow \infty} \frac{F(q, t)}{S(q)}, \quad (3.71)$$

appropriately called the non-ergodicity factor, will provide information on the modes which are not decaying.  $f(q)$  possess the additional benefit of not depending on time, therefore it

<sup>5</sup>Another version of the ZM equation for other applications has only a first order derivative.

<sup>6</sup>We call "mode" the value assumed by  $F(q, t)$  for a specific  $q$ .

satisfies a time-independent ZM equation [KB11, Kra07]

$$\frac{f(\mathbf{q})}{1-f(\mathbf{q})} = \frac{\rho S(\mathbf{q})}{16\pi^3 q^4} \int_{\mathbb{R}^3} S(\mathbf{k})f(\mathbf{k})S(|\mathbf{q}-\mathbf{k}|)f(|\mathbf{q}-\mathbf{k}|) \left[ (\mathbf{q} \cdot \mathbf{k})c(\mathbf{k}) + \mathbf{q} \cdot (\mathbf{q}-\mathbf{k})c(|\mathbf{q}-\mathbf{k}|) \right]^2 d\mathbf{k}. \quad (3.72)$$

Thus, whenever the full time-dependence of the decay of  $F(\mathbf{q}, t)$  is not important, one can just compute only  $f(\mathbf{q})$ , which is easier and faster.

### 3.4 Solution schemes for the theoretical approaches

#### 3.4.1 Lado RHNC solution (for the $g(r)$ and the thermodynamics)

In 1982, Fred Lado proposed to expand the correlation functions onto rotational invariants [Lad82]. Axially symmetric particles like IPCs have two rotational degrees of freedom, so their correlation functions have four. Since each couple of degrees of freedom requires a spherical harmonic  $Y_\ell^m(\theta, \phi)$ , a generic function  $F(r, \theta_1, \theta_2, \phi)$  is expanded as follows:

$$F(r, \theta_1, \theta_2, \phi) = 4\pi \sum_{\ell_1=0}^{\infty} \sum_{\ell_2=0}^{\infty} \sum_{m=-M}^M f_{\ell_1 \ell_2 m}(r) Y_{\ell_1}^m(\theta_1, \phi_1) Y_{\ell_2}^{-m}(\theta_2, \phi_2), \quad (3.73)$$

where  $M = \min(\ell_1, \ell_2)$ ,  $\mathbf{r}$  is the vector joining the two particle centers,  $\theta_i$  is the angle between  $\mathbf{r}$  and the orientation unit vector of particle  $i$ , and  $\phi = \phi_2 - \phi_1$  is the difference in the azimuthal angle, i.e. the angle between the two orientation unit vectors in the plane orthogonal to  $\mathbf{r}$ . The functions do not depend directly on  $\phi_2$  and  $\phi_1$  because of the isotropy of space, consequently only the difference  $\phi$  appears in the expansions, in exponentials like  $e^{m(\phi_2 - \phi_1)}$ . To reconstruct  $F(r, \theta_1, \theta_2, \phi)$  from the  $f_{\ell_1 \ell_2 m}(r)$  coefficients, the inverse formula can be used:

$$f_{\ell_1 \ell_2 m}(r) = \frac{1}{(4\pi)^2} \int [Y_{\ell_1}^m(\theta_1, \phi_1) Y_{\ell_2}^{-m}(\theta_2, \phi_2)]^* F(r, \theta_1, \theta_2, \phi) \sin \theta_1 d\theta_1 \sin \theta_2 d\theta_2 d\phi_1 d\phi_2. \quad (3.74)$$

Some of the  $f_{\ell_1 \ell_2 m}(r)$  coefficients have an obvious interpretation: the  $g_{000}$  is the spherical average and coincides with the  $g(r)$  of an isotropic system thanks to the  $4\pi$  in the definition, the terms with  $\ell_i = 1$  depend on the dipole moment that the potential might possess (and thus are all zero in the case of IPCs with symmetric patches), and so on.

Lado proposed to use this expansion to simplify the solution of the MOZ equation (3.50). Written for the coefficients of the total correlation function and direct correlation function,  $h_{\ell_1 \ell_2 m}(r)$  and  $c_{\ell_1 \ell_2 m}(r)$ , the MOZ equation reads

$$h_{\ell_1 \ell_2 m}(r_{12}) - c_{\ell_1 \ell_2 m}(r_{12}) = (-1)^m \rho \sum_{j=0}^{\infty} \int h_{\ell_1 j m}(r_{13}) c_{j \ell_2 m}(r_{32}) dr_3 \quad (3.75)$$

where we had to introduce  $\mathbf{r}_{ij} = \mathbf{r}_i - \mathbf{r}_j$ ,  $\mathbf{r}_i$  being the position of particle  $i$ ; what we called  $\mathbf{r}$  is obviously  $\mathbf{r}_{12}$ . In Fourier space equation (3.75) becomes

$$h_{\ell_1 \ell_2 m}(\mathbf{k}) - c_{\ell_1 \ell_2 m}(\mathbf{k}) = (-1)^m \rho \sum_{j=0}^{\infty} h_{\ell_1 j m}(\mathbf{k}) c_{j \ell_2 m}(\mathbf{k}), \quad (3.76)$$

which, at fixed  $m$ , is a system of linear integral equations in the first two indices.

The second equation that is necessary to solve to obtain the correlation functions is the closure equation (3.51). Unfortunately, due to its nonlinearity, it does not simplify when expanded onto spherical harmonics, and must be solved as it is.

Lado devised a program for the self-consistent solution of equations (3.76) and (3.51) in reference [Lad82]. It follows an iterative procedure divided in two steps. In the first one, starting from a guess for  $h(r, \theta_1, \theta_2, \phi)$ , the closure relation (3.51) is solved for  $c(r, \theta_1, \theta_2, \phi)$ . The bridge function used is  $E_{\text{HS}}(r; \sigma^*)$ , i.e. the bridge of an HS fluid based on the parametrization proposed in [VW72]; the parameter  $\sigma^*$  is an effective HS diameter that differs from the diameter of the particles under study, and for which at the beginning of the iterative procedure a suitable guess is assumed. In the second step,  $c(r, \theta_1, \theta_2, \phi)$  is expanded in terms of the  $c_{\ell_1 \ell_2 m}(r)$ , using formula (3.74); the angular integrals are carried out using Gaussian quadratures. The  $c_{\ell_1 \ell_2 m}(r)$  coefficients are then Fourier transformed and used to solve equation (3.76) for the  $h_{\ell_1 \ell_2 m}(r)$ . The  $h(r, \theta_1, \theta_2, \phi)$  is then obtained from the  $h_{\ell_1 \ell_2 m}(r)$  coefficients via formula (3.73). These two steps constitute an iteration loop that will be iterated to self-consistency. Many subtleties are used to treat the discontinuities and the Fourier transforms; the reader is referred to references [Lad82, GLL<sup>+</sup>09, GLL<sup>+</sup>10, GGL<sup>+</sup>14] for more details.

When convergence is achieved <sup>7</sup> for a particular value of  $\sigma^*$ , then this variable is changed and the iterative scheme is repeated, until the free energy of the system, which is convex with respect to  $\sigma^*$ , has been minimized. The way in which the free energy is computed is very complicated, and the interested reader should consult [GGL<sup>+</sup>09, GLL<sup>+</sup>10].

The initial guess for  $g(r, \theta_1, \theta_2, \phi)$  and  $\gamma(r, \theta_1, \theta_2, \phi)$  stems, whenever possible, from a previous solution of the problem for a neighbouring state point; otherwise the program can resort to the parametrization of the isotropic HS counterparts of  $g(r, \theta_1, \theta_2, \phi)$  and  $\gamma(r, \theta_1, \theta_2, \phi)$  proposed in [VW72].

Once the algorithm has converged, the excess energy per particle and the pressure are obtained from the following equations:

$$u_{\text{xc}} = \frac{\rho}{2} \int dX g(r, \theta_1, \theta_2, \phi) \varphi(r, \theta_1, \theta_2, \phi), \quad (3.77)$$

$$p = \rho k_B T - \frac{\rho^2}{6} \int dX g(r, \theta_1, \theta_2, \phi) r \frac{\partial}{\partial r} \varphi(r, \theta_1, \theta_2, \phi), \quad (3.78)$$

where we used the symbol

$$\int dX = \frac{1}{(4\pi)^2} \int_0^\infty dr \int_{-1}^1 d \cos \theta_1 \int_{-1}^1 d \cos \theta_2 \int_0^{2\pi} d\phi_1 \int_0^{2\pi} d\phi_2. \quad (3.79)$$

The chemical potential can be computed from pressure and the free energy  $F$  using formula  $\beta\mu = \beta F/N + \beta p/\rho$ . <sup>8</sup>

The computation of a single state point takes just a few minutes on a modern computer, although high density and/or low temperature states may require intermediate steps.

<sup>7</sup>In our case, the criterium is  $\sum_{\ell_1 \ell_2 m} \int h_{\ell_1 \ell_2 m}(r) dr < 10^{-5}$ .

<sup>8</sup>The validity of this formula is far from obvious: due to the approximations introduced, in many theories this is not valid. Lado's treatment [Lad82] ensures that the Hiroike condition  $\rho \frac{\partial u}{\partial \rho} = \beta \frac{\partial}{\partial \beta} \left( \frac{\beta p}{\rho} \right)$  is satisfied, and this is sufficient for  $\beta\mu = \beta F/N + \beta p/\rho$  to hold. See for example reference [GGL<sup>+</sup>10].

### 3.4.2 Barker-Henderson TPT (for the thermodynamics)

The original Barker-Henderson Thermodynamic Perturbation Theory [BH67] (TPT) for isotropic systems was devised to allow an approximate computation of the pressure and the chemical potential, so that coexistence regions could be obtained by searching for the state points of equal  $T$ ,  $p$  and  $\mu$ . The Helmholtz free energy  $F$  is expanded in a perturbative series starting from a reference fluid:

$$\frac{\beta F}{N} = \frac{\beta F_{\text{ref}}}{N} + \sum_{i \geq 1} \frac{\beta F_i}{N}, \quad (3.80)$$

where  $N$  is again the number of particles and  $\beta = 1/k_B T$ . Each  $\beta F_i/N$  is computed as an integral of the potential weighted by the reference pair distribution function [BH67]. The reference fluid was chosen in the paper to be the hard-sphere fluid, for which good parametrizations of the pair distribution function as well as the free energy are available.

The TPT was later extended to anisotropic potentials in reference [GRSG12]; they still used the hard spheres as the reference fluid, and they proposed to use the spherical average of the potential in the integrals. According to reference [GRSG12], the the first and second order corrections are

$$\beta F_1/N = 2\pi\rho \int_{2\sigma}^{2\sigma+\delta} g_{\text{ref}}(r) \langle \beta \varphi(r, \hat{\omega}_1, \hat{\omega}_2) \rangle_{\hat{\omega}_1, \hat{\omega}_2} dr \quad (3.81)$$

and

$$\beta F_2/N = -\frac{\pi\rho}{\tilde{\chi}} \int_{2\sigma}^{2\sigma+\delta} g_{\text{ref}}(r) \langle [\beta \varphi(r, \hat{\omega}_1, \hat{\omega}_2)]^2 \rangle_{\hat{\omega}_1, \hat{\omega}_2} dr, \quad (3.82)$$

where  $\langle \dots \rangle_{\hat{\omega}_i} = \frac{1}{4\pi} \int d\hat{\omega}_i$  indicates an angular average over the solid angle,  $\hat{\omega}_i$  is the orientation of the particle  $i$ , and

$$\tilde{\chi} = \frac{6}{\pi} \frac{\partial}{\partial \rho} \left( \frac{\beta p}{\rho} \right)_{\text{ref}}. \quad (3.83)$$

Knowing the free energy, the pressure and the chemical potential can be computed as

$$\frac{\beta p}{\rho} = \rho \frac{\partial}{\partial \rho} \left( \frac{\beta F}{N} \right) \quad \text{and} \quad \beta \mu = \frac{\partial}{\partial \rho} \left( \rho \frac{\beta F}{N} \right). \quad (3.84)$$

As mentioned above, the reference fluid was chosen to be hard spheres due to the availability of parametrization for the observables needed by the TPT. The equation of state of hard spheres can be approximated by the Carnahan and Starling formula [CS69, Ros90], and the pair distribution function was modeled by Verlet and Weis [VW72].

### 3.4.3 MCT solution (non-ergodicity factor)

In non-ergodic systems, the intermediate scattering function  $F(q, t)$  introduced in (3.64) does not uniformly decay to zero at large time; the limit behavior is captured by the so-called non-ergodicity parameter (NEP), defined as

$$f(q) = \lim_{t \rightarrow \infty} \frac{F(q, t)}{S(q)}, \quad (3.85)$$

where  $S(q) = F(q, 0)$  is the well-known static structure factor.  $f(q)$  provides information on which modes are not decaying to zero at  $t \rightarrow \infty$ , and satisfies the equation

$$f(q) = \frac{M(q)}{M(q) + 1} \quad (3.86)$$

with

$$M(q) = \frac{\rho S(q)}{2q^4} \int_{\mathbb{R}^3} \frac{d\mathbf{k}}{(2\pi)^3} S(k)f(k)S(|\mathbf{q}-\mathbf{k}|)f(|\mathbf{q}-\mathbf{k}|) \left[ (\mathbf{q} \cdot \mathbf{k})c(k) + \mathbf{q} \cdot (\mathbf{q}-\mathbf{k})c(|\mathbf{q}-\mathbf{k}|) \right]^2, \quad (3.87)$$

where  $c(q) = \rho^{-1}(1 - 1/S(q))$ . These two equations can be numerically solved starting from a guess for  $f(q)$ ,<sup>9</sup> solving for  $M$ , and using it to obtain a new estimate for  $f$ . This cycle has to be repeated until convergency is achieved.

The complicated expression for  $M(q)$  can be rewritten in a form that is better suited to numerical computation. [Voi02] Using polar coordinates and exploiting the symmetry of the integrand around  $\mathbf{q}$ , the integration variables and boundaries become

$$\int_{\mathbb{R}^3} d\mathbf{k} = 2\pi \int_0^\infty k^2 dk \int_{-1}^1 d \cos \theta, \quad (3.88)$$

with  $\theta$  being the angle between  $\mathbf{k}$  and  $\mathbf{q}$ . The integration variable is now changed from  $\cos \theta$  to  $p$ , the modulus of  $\mathbf{p} = \mathbf{q} - \mathbf{k}$ ;  $\cos \theta$  and  $p$  are related via the equation  $p^2 = (\mathbf{q} - \mathbf{k})^2 = q^2 + k^2 - 2qk \cos \theta$ . A differentiation and straightforward algebra yield for the integration variables and boundaries

$$\int_{\mathbb{R}^3} \frac{d\mathbf{k}}{(2\pi)^3} = \frac{1}{q} \int_0^\infty \frac{k dk}{2\pi} \int_{|q-k|}^{q+k} \frac{p dp}{2\pi}. \quad (3.89)$$

Substitution of (3.89) in (3.87) yields

$$M(q) = \frac{\rho S(q)}{8\pi^2 q^5} \int_0^\infty dk \quad k S(k) f(k) \int_{|q-k|}^{q+k} dp \quad p S(p) f(p) \left[ (\mathbf{q} \cdot \mathbf{k})c(k) + (\mathbf{q} \cdot \mathbf{p})c(p) \right]^2. \quad (3.90)$$

The scalar products can be written in terms of  $q$ ,  $k$  and  $p$  as

$$2\mathbf{q} \cdot \mathbf{k} = q^2 + k^2 - p^2, \quad (3.91)$$

$$2\mathbf{q} \cdot \mathbf{p} = q^2 + p^2 - k^2. \quad (3.92)$$

Substitution of these expression gives the final formula for  $M$ ,

$$M(q) = \frac{\rho S(q)}{32\pi^2 q^5} \int_0^\infty dk \quad k S(k) f(k) \times \int_{|q-k|}^{q+k} dp \quad p S(p) f(p) \left[ (q^2 + k^2 - p^2)c(k) + (q^2 + p^2 - k^2)c(p) \right]^2, \quad (3.93)$$

which can be discretized in two Riemann sums on  $k$  and  $p$ . The final subtlety is due to the value  $M(q = 0)$ , problematic because of the divergent  $q^{-5}$  term; the obvious solution is to compute  $M(q)$  on a grid spaced not as

$$0, \delta k, 2\delta k, \dots \quad (3.94)$$

but instead as

$$\frac{1}{2}\delta k, \left(1 + \frac{1}{2}\right)\delta k, \left(2 + \frac{1}{2}\right)\delta k \dots \quad (3.95)$$

<sup>9</sup>not too refined: even  $f(q) \equiv 1$  often works, while  $f(q) \equiv 0$  has to be avoided because it's always a solution but not the interesting one.

### 3.5 Numerical simulations using molecular dynamics

Numerical simulations have been used with profit since many years, and are now regarded as the third paradigm of physics: after a theory is developed, gets tested and refined by the comparison with simulations, and only later compared with experiments. The simplest introductory book on the subject is [FS02], while [AT87] presents indispensable “advanced” topics like cell lists and constrained dynamics.

In an N-body problem we consider N point particles of mass  $m_i$  under the influence of an interaction pair potential  $\varphi(\mathbf{x}_i, \mathbf{x}_j)$ . The equations of motion for particle i read

$$m_i \ddot{\mathbf{x}}_i(t) = \mathbf{F}_i(t), \quad (3.96)$$

where  $\mathbf{x}_i$  is the trajectory of particle i, the dots denote time derivation, and  $\mathbf{F}_i$  is the total force acting on particle i

$$\mathbf{F}_i(t) = -\nabla_{\mathbf{x}_i} \sum_{j \neq i} \varphi(\mathbf{x}_i, \mathbf{x}_j), \quad (3.97)$$

which depends on the trajectory of all particles. This set of equations is impossible to solve analytically, so we find ourself in need of an approximate numeric solution.

#### 3.5.1 Velocity-Verlet algorithm

Molecular dynamics (MD) solves an N-body problem by substituting the time derivatives in the equations of motion with finite differences. The trajectories are reconstructed on a discrete time grid. Many algorithms have been proposed with different degrees of short-time and long-time accuracy; the one of our choice is the Velocity-Verlet (VV) algorithm. VV discretized the equations of motion (3.96) for particle i as [SABW82, AT87, FS02]

$$\mathbf{x}_i(t+h) = \mathbf{x}_i(t) + \mathbf{v}_i(t)h + \frac{\mathbf{F}_i(t)}{2m_i}h^2, \quad (3.98)$$

$$\mathbf{v}_i(t+h) = \mathbf{v}_i(t) + \frac{\mathbf{F}_i(t) + \mathbf{F}_i(t+h)}{2m_i}h. \quad (3.99)$$

This algorithm has many good properties, that are well described in the references, and will not be repeated. To speed up the time-expensive force calculation we use cell lists [AT87]; the code was written in C++ and compiled with g++ version 4.1.2 20080704, and parallelized using the GNU OpenMP library.

Two difficulties arise when applying VV to IPCs, and the next paragraphs will present them.

#### 3.5.2 Adaptation of the potential

The force between two particles is obtained as the gradient of the potential:

$$\mathbf{F}_{12}(\mathbf{x}_1, \mathbf{x}_2) = -\nabla_{\mathbf{x}_1} \varphi(\mathbf{x}_1, \mathbf{x}_2) = -\mathbf{F}_{21}. \quad (3.100)$$

The IPC potential presented in § 2.3 includes an hard sphere which, at the contact between two particles, is discontinuous. A discontinuous potential in equation (3.100) implies that



the force diverges, and thus cannot be used inside the VV scheme. Usually, hard sphere dynamics is treated using the so-called collision dynamics, which does not discretize the times: particles follow an uniform linear motion until they collide, and the collisions are approximated as perfectly elastic scattering. Unfortunately, such an approach is incompatible with the continuous part of the potential.

In our program, we used the VV algorithm but substituted the hard sphere with a soft sphere potential, which at center-center particle distance  $r$  reads

$$\varphi_{\text{HC}}(r) = A \left[ \left( \frac{2\sigma_C}{r} \right)^{2k} - 2 \left( \frac{2\sigma_C}{r} \right)^k + 1 \right] \Theta(2\sigma_C - r), \quad (3.101)$$

where  $A$  (which has the dimension of an energy) and  $k$  (adimensional) are parameters to be fitted to properly reproduce IPCs. This soft sphere potential is regular<sup>10</sup> and vanishes at  $r \geq 2\sigma_C$ , as does its first derivative.

The sensibility of the soft-core version of the model was checked by comparing energies, pair distribution functions and static structure factors obtained via MD with the same observables obtained via Monte Carlo simulations of the original hard-sphere model from [BKL11]. We did this check at many state points, and at different patch amplitudes and interaction strengths. Values of  $k = 15$  and  $A = 500\epsilon_m$  where chosen, where  $\epsilon_m$  is the energy unit that will be defined in chapter 4. No significative deviations were observed between the hard-sphere and the soft-sphere model.

The reader could wonder if the exponent  $k$  is not too small, making the potential not sufficiently stiff to reproduce an hard core. In fact, a value of  $k = 15$  is small compared to what is used in other papers –for example, a value of 100 was used in [AFST05], where a very similar potential is used. But looking at the exponent alone is deceiving, because the large value of the coefficient  $A$  contributes to make the potential as stiff as needed in the range that is actually explored by the particles during the simulation.

### 3.5.3 Adaptation of the algorithm

IPCs are linear rigid bodies, composed of three interaction centers. There are two standard ways to treat the dynamics of rigid bodies in MD: the decomposition of the motion in center-of-mass motion plus rotation, and constrained dynamics.

The first approach associates a 4-dimensional unit vector (called quaternion) to a general rigid body, and a three dimensional unit vector to a linear/axial particle. Albeit extremely efficient, quaternions are not easy to implement nor very flexible: for example, switching from a linear two-patch particle to a more complex three-patch particle would require complete rewriting of the program.

Within constrained dynamics, instead, the trajectories of all the interaction sites are computed, while forcing them to keep fixed mutual distances by inserting the constraints into the equations of motion via Lagrange multipliers. Constrained dynamics is less efficient

<sup>10</sup>Regular in the sense continuous with continuous first derivative ( $C^1$ ). A discontinuity in the potential would cause a divergent force, a discontinuity in the force would cause a divergence in the pressure; hence it is crucial for the potential to be at least  $C^1$ . Continuity in higher order derivatives is not required, in fact the proposed potential is not even  $C^2$ .

than quaternions, but extremely easy to code and to extend, and in addition works with the position of the three interaction sites, which would be required anyway to compute the forces using equation (2.6).

Because of these reasons, we choose constrained dynamics for our program. Unfortunately, another problem has yet to be solved. An IPCs is described as a linear molecule composed of three sites, one for the center of the colloid and two for the patches. In the framework of VV, constrained dynamics is implemented via the RATTLE algorithm [And82]; unfortunately, this approach is singular for linear particles. The reason is that the corrections to the trajectories are proportional to the relative positions of the three sites,  $\mathbf{x}_c - \mathbf{x}_1$ ,  $\mathbf{x}_c - \mathbf{x}_2$  and  $\mathbf{x}_2 - \mathbf{x}_1$ , where  $c$  denotes the colloid center and 1 and 2 the patches. For a general rigid body, these three vectors form a basis of  $\mathbb{R}^3$ ; however, in the case of a linear particle they are all parallel, and as soon as one of the sites develops a displacement in a direction orthogonal to the initial one, the algorithm can no longer correct for it, and consequently fails. Due to this problem, we make use of the scheme introduced in reference [CFR82] to reduce the number of degrees of freedom of rigid bodies. The Ciccotti scheme divides the particles in two groups: “primary” particles, whose trajectory will be integrated by solving the equations of motion, and “secondary” particles, whose trajectory will not be integrated but computed as a linear combination of the trajectories of the primary particles. These linear combinations are used as constraints, that will be included in the equations of motion of the primary particles via an effective force representing the inertia of the secondary particles; in addition to these effective forces, the trajectories of the primary particles will be integrated using constrained dynamics. Having less trajectories to be integrated, the code also becomes more efficient.

The entire procedure will be clarified in the next paragraph by applying the concept to the IPC case.

### Construction of the equations of motion

The two patches will be considered the primary particles. The colloid center is treated as a secondary particle<sup>11</sup>, whose position position can be written as the linear combination

$$\mathbf{x}_c = (e_1/d)\mathbf{x}_2 + (e_2/d)\mathbf{x}_1, \quad (3.102)$$

where  $e_1, e_2$  are the the eccentricities that were introduced in § 2.3,  $d = e_1 + e_2$ , and  $\mathbf{x}_{12} = \mathbf{x}_1 - \mathbf{x}_2$ . Equation (3.102) is the first constraint imposed on each IPC; the second is due to the fixed distance between the particles. We reformulate both constraints as:

$$\sigma = (\mathbf{x}_1 - \mathbf{x}_2)^2 - d^2 = 0 \quad \text{and} \quad \boldsymbol{\tau} = -\mathbf{x}_c + (e_1/d)\mathbf{x}_2 + (e_2/d)\mathbf{x}_1 = 0. \quad (3.103)$$

The equations of motion are corrected subtracting the gradient of the constraints multiplied by the Lagrange multipliers  $\boldsymbol{\mu}$  and  $\lambda$ :

$$m_i \mathbf{x}_i = \mathbf{F}_i - (1/2) \nabla_i (\boldsymbol{\tau} \cdot \boldsymbol{\mu} + \lambda \sigma), \quad (3.104)$$

<sup>11</sup>Of course using the center and one of the patches as primary would be perfectly equivalent.

where  $i = 1, 2, c$ , denote the first patch, the second patch and the center, and the  $1/2$  factor is for future convenience. Substitution of the constraints (3.103) in the equations of motion (3.104) gives

$$\begin{cases} m_1 \ddot{\mathbf{x}}_1 = \mathbf{F}_1 - (e_2/d)\boldsymbol{\mu} - \lambda \mathbf{x}_{12} \\ m_2 \ddot{\mathbf{x}}_2 = \mathbf{F}_2 - (e_1/d)\boldsymbol{\mu} + \lambda \mathbf{x}_{12} \\ m_c \ddot{\mathbf{x}}_c = \mathbf{F}_c - \boldsymbol{\mu}. \end{cases} \quad (3.105)$$

We can now determine the value of  $\boldsymbol{\mu}$  from the constraint  $\tau = 0$ . Inserting the equations of motion (3.105) in the second time derivative of  $\tau = 0$ , and solving for  $\boldsymbol{\mu}$ , we obtain the value

$$\boldsymbol{\mu} = -\frac{d^2}{I m_c} \mathbf{F}_c + \frac{de_1}{I m_2} \mathbf{F}_2 + \frac{de_2}{I m_1} \mathbf{F}_1 - \lambda \left[ \frac{de_2}{I m_1} - \frac{de_1}{I m_2} \right] \mathbf{x}_{12} \quad (3.106)$$

where for ease of writing we defined

$$I = \frac{d^2}{m_c} + \frac{e_1^2}{m_1} + \frac{e_2^2}{m_2}. \quad (3.107)$$

Since this value of  $\boldsymbol{\mu}$  ensures that the constraint  $\tau = 0$  is always satisfied, we can use equation (3.102) as the trajectory of the colloid center  $\mathbf{x}_c(t)$ ; this is a great simplification, because we are substituting a second order differential equation with a linear algebraic equation. Now we only need to integrate for the trajectories of the patches  $\mathbf{x}_1(t)$  and  $\mathbf{x}_2(t)$ , and the position of the colloid center can be obtained from them. With this simplification, the equations of motion that we have to solve are

$$\begin{cases} m_1 \ddot{\mathbf{x}}_1 = \left(1 - \frac{e_2^2}{I m_1}\right) \mathbf{F}_1 + \left(-\frac{e_1 e_2}{I m_2}\right) \mathbf{F}_2 + \left(\frac{de_2}{I m_c}\right) \mathbf{F}_c - \lambda \left[1 + \frac{e_1}{I} \left(\frac{e_2}{m_1} - \frac{e_1}{m_2}\right)\right] \mathbf{x}_{12} \\ m_2 \ddot{\mathbf{x}}_2 = \left(1 - \frac{e_1^2}{I m_2}\right) \mathbf{F}_2 + \left(-\frac{e_1 e_2}{I m_1}\right) \mathbf{F}_1 + \left(\frac{de_1}{I m_c}\right) \mathbf{F}_c + \lambda \left[1 + \frac{e_2}{I} \left(\frac{e_2}{m_1} - \frac{e_1}{m_2}\right)\right] \mathbf{x}_{12}. \end{cases} \quad (3.108)$$

#### Application of RATTLE and VV

The system (3.108) still contains the Lagrange multiplier  $\lambda$ . If we were to naively substitute (3.108) in the second time derivative of  $\sigma = 0$  (equation (3.103)), we would obtain a solution that would be subject to a large error when we discretize the equations of motion for numerical solution (the reason is explained in reference [And82]). The idea behind RATTLE is to determine the value of  $\lambda$  at each numerical integration step, so that  $\sigma = 0$  is always satisfied within numerical accuracy.

First, we rewrite (3.108) in a shorter way: we call  $\tilde{\mathbf{F}}$  the effective total forces, and we introduce two coefficients  $\alpha_1$  and  $\alpha_2$  defined as

$$\alpha_1 = 1 + \frac{e_2}{I} \left( \frac{e_2}{m_1} - \frac{e_1}{m_2} \right), \quad \alpha_2 = 1 + \frac{e_1}{I} \left( \frac{e_2}{m_1} - \frac{e_1}{m_2} \right), \quad (3.109)$$

so that the equations of motion for the patches of a single IPC read now as

$$\begin{cases} m_1 \ddot{\mathbf{x}}_1 = \tilde{\mathbf{F}}_1 - \alpha_1 \lambda \mathbf{x}_{12} \\ m_2 \ddot{\mathbf{x}}_2 = \tilde{\mathbf{F}}_2 + \alpha_2 \lambda \mathbf{x}_{12} \end{cases} . \quad (3.110)$$

Within the VV scheme, equations (3.110) are discretized as

$$\begin{cases} \mathbf{x}_1(t+h) = \mathbf{x}_1(t) + h\mathbf{v}_1(t) + \frac{h^2}{2m_1}\tilde{\mathbf{F}}_1(t) - \alpha_1\lambda_x\mathbf{x}_{12}(t) \\ \mathbf{x}_2(t+h) = \mathbf{x}_2(t) + h\mathbf{v}_2(t) + \frac{h^2}{2m_2}\tilde{\mathbf{F}}_2(t) + \alpha_2\lambda_x\mathbf{x}_{12}(t) \\ \mathbf{v}_1(t+h) = \mathbf{v}_1(t) + \frac{h}{2m_1}(\tilde{\mathbf{F}}_1(t) + \tilde{\mathbf{F}}_1(t+h)) - \alpha_1\lambda_v\mathbf{x}_{12}(t+h) \\ \mathbf{v}_2(t+h) = \mathbf{v}_2(t) + \frac{h}{2m_2}(\tilde{\mathbf{F}}_2(t) + \tilde{\mathbf{F}}_2(t+h)) + \alpha_2\lambda_v\mathbf{x}_{12}(t+h). \end{cases} \quad (3.111)$$

where  $\mathbf{v}_i(t)$  are the velocities and  $h$  is again the time step. Following reference [And82], two different Lagrange multipliers are used,  $\lambda_x$  and  $\lambda_v$ . The first two equations of (3.111) are solved for the new positions  $\mathbf{x}_1(t+h)$  and  $\mathbf{x}_2(t+h)$ , which can then be used to compute the new velocities  $\mathbf{v}_1(t+h)$  and  $\mathbf{v}_2(t+h)$ .

The equations for the positions of the patches are solved as follows. Defining the uncorrected positions

$$\mathbf{s}_i(t) = \mathbf{x}_i(t) + h\mathbf{v}_i(t) + \frac{h^2}{2m_i}\tilde{\mathbf{F}}_i(t), \quad (3.112)$$

and  $\mathbf{s}_{12} = \mathbf{s}_1 - \mathbf{s}_2$ , the constraint  $|\mathbf{x}_1(t+h) - \mathbf{x}_2(t+h)|^2 = d^2$  reads

$$|\mathbf{s}_1 - \alpha_1\lambda_x\mathbf{x}_{12} - \mathbf{s}_2 - \alpha_2\lambda_x\mathbf{x}_{12}|^2 = \mathbf{s}_{12}^2 - 2\lambda_x(\alpha_1 + \alpha_2)\mathbf{s}_{12} \cdot \mathbf{x}_{12} + O(\lambda_x^2) = d^2, \quad (3.113)$$

which can be solved for  $\lambda_x$  as

$$\lambda_x = \frac{\mathbf{s}_{12}^2 - d^2}{2(\alpha_1 + \alpha_2)\mathbf{s}_{12} \cdot \mathbf{x}_{12}} + O(\lambda_x^2). \quad (3.114)$$

This value is substituted in equation (3.111) and the new positions  $\mathbf{x}_i(t+h)$  are updated. Since terms of order  $O(\lambda_x^2)$  have been neglected in equation (3.114), the positions might have to be corrected more than once; if

$$|\mathbf{x}_1(t+h) - \mathbf{x}_2(t+h)|^2 - d^2 < 10^{-12}d^2, \quad (3.115)$$

the program can go on, otherwise  $\lambda_x$  is recomputed from equation (3.114) using the just corrected positions until (3.115) is satisfied. The reader familiar with machine calculus will notice that  $10^{-12}$  is quite close to the machine epsilon;<sup>12</sup> in fact, a threshold lower than  $10^{-12}$  would make convergence unreachable with 8 byte variables.

Once the new positions  $\mathbf{x}(t+h)$  of all the patches of all the IPCs have been corrected, the velocities are also updated, according to

$$\mathbf{v}_i(t+h/2) = \mathbf{v}_i(t) + \frac{h}{2m_i}\tilde{\mathbf{F}}_i(t). \quad (3.116)$$

The old forces are no longer needed, and their memory space can be used to store the new forces  $\tilde{\mathbf{F}}_i(t+h)$ , that are now computed from the new positions  $\mathbf{x}(t+h)$ . The velocities are again updated, as

$$\mathbf{v}_i^*(t+h) = \mathbf{v}_i(t+h/2) + \frac{h}{2m_i}\tilde{\mathbf{F}}_i(t+h), \quad (3.117)$$

where the \* signals that we still have to correct for the constraints. According to the RATTLE scheme, we must enforce the time derivative of the constraint  $|\mathbf{x}_{12}(t+h)|^2 = d^2$ ,

$$\mathbf{x}_{12}(t+h) \cdot \mathbf{v}_{12}(t+h) = 0, \quad (3.118)$$

<sup>12</sup> The machine epsilon  $\epsilon$  is the smallest number satisfying  $1 + \epsilon \neq 1$  in machine algebra. Using 8 bytes variables it is  $1.11 \dots \times 10^{-16}$ .

where  $\mathbf{v}_{12} = \mathbf{v}_1 + \mathbf{v}_2$ . This constraint ensures that the velocities of the patches cannot stretch the IPC but can only rotate or translate it. Thus, to obtain the updated velocities

$$\mathbf{v}_i(t+h) = \mathbf{v}_i^*(t+h) \mp \alpha_i \lambda_v \mathbf{x}_{12}(t+h), \quad (3.119)$$

we substitute (3.119) in the constraint (3.118), obtaining

$$[\mathbf{v}_{12}^*(t+h) - \lambda_v(\alpha_1 + \alpha_2)\mathbf{x}_{12}(t+h)] \cdot \mathbf{x}_{12}(t+h) = 0, \quad (3.120)$$

which can be solved (exactly) as

$$\lambda_v = \frac{\mathbf{v}_{12}^* \cdot \mathbf{x}_{12}}{(\alpha_1 + \alpha_2)d^2}. \quad (3.121)$$

As a safety measure to avoid problems due to machine arithmetic (explained by [AT87], but only in the example codes on the website), equations (3.118) are only applied if

$$q_{12} \cdot \mathbf{x}_{12} < 10^{-12}. \quad (3.122)$$

#### Symmetric solution

In the most symmetric case ( $m_1 = m_2 = m_p$  and  $\mathbf{e}_1 = \mathbf{e}_2$ ) the equations of motion (3.108) reduce to

$$\begin{cases} m_1 \ddot{\mathbf{x}}_1 &= \left(1 - \frac{m_c}{2M}\right) \mathbf{F}_1 + \left(-\frac{m_c}{2M}\right) \mathbf{F}_2 + \left(\frac{m_p}{M}\right) \mathbf{F}_c - 2\lambda \mathbf{x}_{12} \\ m_2 \ddot{\mathbf{x}}_2 &= \left(1 - \frac{m_c}{2M}\right) \mathbf{F}_2 + \left(-\frac{m_c}{2M}\right) \mathbf{F}_1 + \left(\frac{m_p}{M}\right) \mathbf{F}_c + 2\lambda \mathbf{x}_{12} \end{cases} \quad (3.123)$$

where  $M = 2m_p + m_c$ , and

$$\mathbf{x}_c = (\mathbf{x}_2 + \mathbf{x}_1)/2; \quad (3.124)$$

the RATTLE equations (3.110) become just

$$\begin{cases} m_1 \ddot{\mathbf{x}}_1 &= \tilde{\mathbf{F}}_1 - \lambda \mathbf{x}_{12} \\ m_2 \ddot{\mathbf{x}}_2 &= \tilde{\mathbf{F}}_2 + \lambda \mathbf{x}_{12} \end{cases} \quad (3.125)$$

since  $\alpha_1 = \alpha_2 = 1$ .



## 4 Results

### Contents

<b>4.1 Symmetric models with small patch extension</b>	<b>51</b>
4.1.1 Phase diagram	52
4.1.2 Dynamics	52
4.1.3 Static structure	53
4.1.4 Thermodynamics	56
4.1.5 Small-patch models: summary	58
<b>4.2 Models with <math>\gamma_1 = 45^\circ</math></b>	<b>60</b>
4.2.1 The crystal-liquid structure formed by model 45n	60
4.2.2 Phase diagram of the 45n model	65
4.2.3 Dynamics of the 45n model	65
4.2.4 Overcharging and undercharging of symmetric IPCs: 45sQc models	68
4.2.5 Models with asymmetric patches	68
4.2.6 45* models: summary	70
<b>4.3 Symmetric models with larger patch extension</b>	<b>71</b>
<b>4.4 Completely asymmetric models</b>	<b>72</b>

This chapter presents most of the results obtained in the three years of the Ph.D. Part of the results was published in peer reviewed journals [KBFK15, FBKK15], and another part will be soon [FBK].

### Units and reduced quantities

Lengths are expressed in units of the hard sphere diameter,  $2\sigma_C$ . The energy unit,  $\epsilon_m$ , is defined as the absolute value of the minimum of the potential between two IPCs, met when particles are at polar-equator alignment and at a center-center distance of  $2\sigma_C$ . The last unit to be fixed is the mass: its unit,  $m_0$ , will be chosen so that an IPC has always a mass of  $3m_0$ . The time unit can be derived from the other units through dimensional analysis:  $t_0 = \sqrt{m_0(2\sigma_C)^2/\epsilon_m}$ . Reduced quantities will be defined for convenience: a reduced density  $\rho^* = \rho/(2\sigma_C)^3$ , a reduced temperature  $T^* = k_B T/\epsilon_m$ , a reduced time  $t^* = t/t_0$ , a reduced pressure  $p^* = p(2\sigma_C)^3/\epsilon_m$  and a reduced excess energy per particle  $u^* = u_{xc}/\epsilon_m$ .<sup>1</sup>

### The models

As explained in chapter 2, a two-patch IPC model is completely specified by its hard-sphere radius  $\sigma_C$ , its patch amplitudes  $\gamma = (\gamma_1, \gamma_2)$ , its interaction range  $\delta$ , and its charge distribution ( $Z_c$  and  $Z_p = (Z_1, Z_2)$ ). Table 4.1 shows these parameters for all the models that we studied. As a consequence of our choice of the units of length and energy, only the ratios  $\delta/2\sigma_C$  and  $Z_i/Z_c$  are relevant.

<sup>1</sup> Should the disappearance of the suffix xc confuse the reader, we specify:  $u^*$  does not include the kinetic contribution  $(3/2)k_B T$ .

Table 4.2 presents the other model parameters that are derived from  $\gamma$ ,  $\delta$  and  $Z$ : the eccentricities  $e$ , the patch interaction sphere radiuses  $\sigma_p$ , and the coupling constants  $u_{ij}$ .

The models presented in tables 4.1 and 4.2 are divided in four blocks according to the patch size. The first block includes small-patch symmetric models, that did not self-assemble in ordered structures, and will be presented in section 4.1. In the models in the second block, one of the patches is fixed to an opening angle of  $45.6^\circ$  while the extent of the other patch is varied; we also study various possibilities of overcharging the colloid center or the patches. This models self-assemble into a very interesting hybrid crystal-liquid structure; the corresponding results are presented in section 4.2. The third block contains four symmetric models with large patches; some of them self-assemble into a face-centered cubic crystal, and the results are presented in section 4.3. In the fourth block, both patches are asymmetric both in charge and size, following the experimental IPCs studied by van Oostrum and coworkers, in part published in [vOHNR15]. The corresponding results are presented in section 4.4.

### Simulation details

Simulations were carried in the NVE ensemble, so whenever we refer to a temperature we actually mean the average value of the temperature during the run. We took great care to ensure that the system was equilibrated by running and that the temperature fluctuations did not present any drift. Most equilibration runs lasted for over  $10^5 t_0$ ; the runs over which the observables were sampled  $10^5 t_0$ . The ensemble size in the simulations varied. Since a single IPC requires a force calculation for each of the three interaction sites, the computational cost of a simulation with  $N$  IPCs is equivalent to the cost of a simulation with  $3N$  spherical particles, so we could not go very high in  $N$ . More than half of the self-assembly runs were done with 2048 IPCs, the others only 1372. Size-effects checks were carried on with 4000 IPCs. Finally, we studied the crystal phase of the 45n models using “perfect” lattices of 1302 IPCs that completely fill the periodic cubic simulation box.

A very important observation is that the mass distribution of the IPCs (i.e. how much mass is concentrated in the colloid center and how much in the patch centers) does not influence the physics. In the experiment of Van Oostrum and coworkers [vOHNR15], the particle is a solid silica sphere with the patch carrying less than 1% of the total mass; thus the inertia tensor of an IPC is basically the inertia tensor of a sphere, because the patches have a negligible mass. In simulation, the inertia tensor for a linear particle is  $I = (m_1 e_1^2 + m_2 e_2^2) \text{diag}(1, 1, 0)$ , where  $m_1$  and  $m_2$  are the masses attributed to the patches. During our runs we verified that a completely symmetric mass distribution where  $m_1 = m_2 = m_C = m_0$ , and a more realistic one in which  $m_1 = m_2 = 0.01 m_0$  and  $m_C = 2.98 m_0$ , showed the same dynamics: the velocity autocorrelation functions were essentially identical, and the orientational autocorrelation functions could be made coincide via a time scaling corresponding to the ratios of the inertia tensors, i.e. the ratio of the masses. Hence, in simulation we used the symmetric distribution  $m_1 = m_2 = m_C = m_0$ , which ensured the highest computational efficiency of the program.



	Model	$\delta/2\sigma_C$	$\gamma$	$-Z_p/Z_c$	Behavior
Section 4.1	M1	0.10	22.3°	1/2	does not self-assemble
	M2	0.30	43.5°	1/2	does not self-assemble
	30n	0.20	31.1°	1/2	does not self-assemble
	g38n	0.25	38.6°	1/2	does not self-assemble
	g38c	0.25	38.6°	5/11	does not self-assemble
	39n	0.20	39.0°	1/2	does not self-assemble
	42n	0.20	42.1°	1/2	does not self-assemble
Section 4.2	3145n	0.2	31.1°, 45.6°	1/2, 1/2	does not self-assemble
	3345n	0.2	33.6°, 45.6°	1/2, 1/2	does not self-assemble
	3645n	0.2	36.2°, 45.6°	1/2, 1/2	self-assembles in AP
	3945n	0.2	39.0°, 45.6°	1/2, 1/2	self-assembles in AP
	4245n	0.2	42.1°, 45.6°	1/2, 1/2	self-assembles in AP
	45n	0.2	45.6°	1/2	self-assembles in SP
	45sQc	0.2	45.6°	15/(30+Q)	most self-assemble in SP
	5045n	0.2	49.5°, 45.6°	1/2, 1/2	does not self-assemble
	5045c	0.2	49.5°, 45.6°	5/11, 5/11	self-assembles in AP
	5545n	0.2	53.9°, 45.6°	1/2, 1/2	does not self-assemble
	6045n	0.2	59.2°, 45.6°	1/2, 1/2	does not self-assemble
Sec. 4.3	50n	0.20	49.5°	1/2	does not self-assemble
	55n	0.20	53.9°	1/2	self assembles in FO
	g57c	0.25	56.8°	15/36	does not self-assemble
	60n	0.20	59.2°	1/2	self assembles in FO
Sec. 4.4	4050c	0.2	39.8°, 49.5°	1/3, 1/2	self-assembles in AP
	4050n	0.2	39.8°, 49.5°	1/2, 1/2	does not self-assemble
	5535n	0.2	55.2°, 34.8°	3/5, 2/5	does not self-assemble

Table 4.1: IPC models: main parameters, as explained in the text. The four blocks in which the table is divided are all addressed in a different section indicated in the first column. When only one value is specified for  $\gamma$  or  $-Z_p/Z_c$ , the model is symmetric. Most model names are chosen to be coherent with the reference in which they were introduced. Models with names composed by a two digits number followed by n or c have symmetric patches,  $\delta/2\sigma_C = 0.2$ , the number specifies  $\gamma$ , and the letter refers to the charging (n for neutral, c for charged). When the number is preceded by a g,  $\delta/2\sigma_C = 0.25$ . Models starting with a four digits number have asymmetric patches, and the number specifies  $\gamma_1$  and  $\gamma_2$ . Models 45sQc are symmetric and the parameter Q controls the overcharging (see section 4.2.4). The acronyms of the structures stand for: SP: Symmetric Planes, AP: Asymmetric Planes (both introduced in section 4.2), and FO: Fcc with Orientations (section 4.3).

	Model	$e/2\sigma_C$	$\sigma_P/2\sigma_C$	$u_{CC}$	$u_{C1}$	$u_{C2}$	$u_{12}$	$u_{11}$	$u_{22}$	
Section 4.1	M1	0.30	0.25	4.284	-111.6			989.0		
	M2	0.30	0.35	0.4230	-10.26			85.47		
	30n	0.32	0.28	0.8631	-26.62			241.8		
	g38n	0.30	0.325	2.707	-18.73			105.9		
	g38c	0.30	0.325	3.553	-20.07			81.54		
	39n	0.26	0.34	1.341	-23.36			177.2		
	42n	0.24	0.36	1.528	-22.50			162.0		
Section 4.2	3145n	0.32, 0.22	0.28, 0.38	0.619166	-26.2067	-7.19724	166.934	302.941	59.6915	
	3345n	0.30, 0.22	0.30, 0.38	0.749261	-24.8535	-8.89217	157.293	260.601	71.7756	
	3645n	0.28, 0.22	0.32, 0.38	0.903902	-23.7641	-11.0287	152.583	227.987	87.0606	
	3945n	0.26, 0.22	0.34, 0.38	1.08756	-22.8896	-13.7380	152.219	202.290	106.575	
	4245n	0.24, 0.22	0.36, 0.38	1.30595	-22.1966	-17.1995	156.124	181.626	131.759	
	45n	0.22	0.28	1.724		-21.87		149.0		
	45sQc	0.22	0.28		depends on Q:					
				2.86231		-23.3889		62.3727		
				2.20791		-22.5177		86.3069		
				1.85387		-22.0465		119.268		
			(45n)	1.724		-21.87		149.0		
				1.66417		-21.7934		200.323		
				2.74534		-23.2332		709.735		
		5045n	0.20, 0.22	0.40, 0.38	1.47400	-16.6738	-21.5407	140.046	117.872	163.221
		5045c	0.20, 0.22	0.40, 0.38	1.96161	-17.1432	-22.1899	102.342	86.1378	119.277
	5545n	0.18, 0.22	0.42, 0.38	1.38637	-12.8009	-21.4180	121.535	83.9937	162.472	
	6045n	0.16, 0.22	0.44, 0.38	1.63959	-10.8657	-22.9990	110.322	61.2675	166.018	
Sec. 4.3	50n	0.20	0.40	1.928	-21.34			137.8		
	55n	0.18	0.42	2.163	-20.90			128.1		
	g57c	0.20	0.425	15.05	-30.79			51.97		
	60n	0.16	0.44	4.003	-25.16			128.2		
Sec. 4.4	4050c	0.255, 0.20	0.345, 0.40	2.13961	-24.1344	-17.4279	94.6045	114.493	76.1911	
	4050n	0.255, 0.20	0.345, 0.40	1.07487	-22.6089	-11.2353	134.523	195.536	80.6252	
	5535n	0.175, 0.29	0.425, 0.31	0.830747	-7.34357	-24.3068	114.705	41.2298	292.121	

Table 4.2: IPC models: secondary coarse-grained parameters (see text). The four blocks in which the table is divided are all addressed in a different section indicated in the first column. When a single value is given for  $e/2\sigma_C$  or  $\sigma_P/2\sigma_C$ , the model is symmetric.

## 4.1 Symmetric models with small patch extension

The models presented in this section have as a common denominator a patch extension smaller than  $45^\circ$  and the fact that they do not self-assemble into ordered structures. Models M1 and M2 were presented as examples in the very first paper about IPCs [BKL11]; model 30n, along with its charged counterpart, was first studied in two-dimensional confinement in reference [BLK13], where via Montecarlo simulations it was clearly seen that no ordered structure would form at finite temperatures. This trend was confirmed by our simulations in three dimensions, where we did not see any self-assembly at all.

We concentrated on the fluid region, that in this work we define as the density range  $\rho^* \in [0.1, 0.8]$  and the temperature range where particles are not frozen (in the sense that particles can diffuse much more than their diameter:  $|\Delta\mathbf{x}(t_S)| \gg \sigma_C$  where  $t_S$  is the simulation time). In this region we found fluid phases and liquid-vapor separation (an example snapshot is shown in figure 4.1). Further cooling of the system would produce a gel, i.e. an

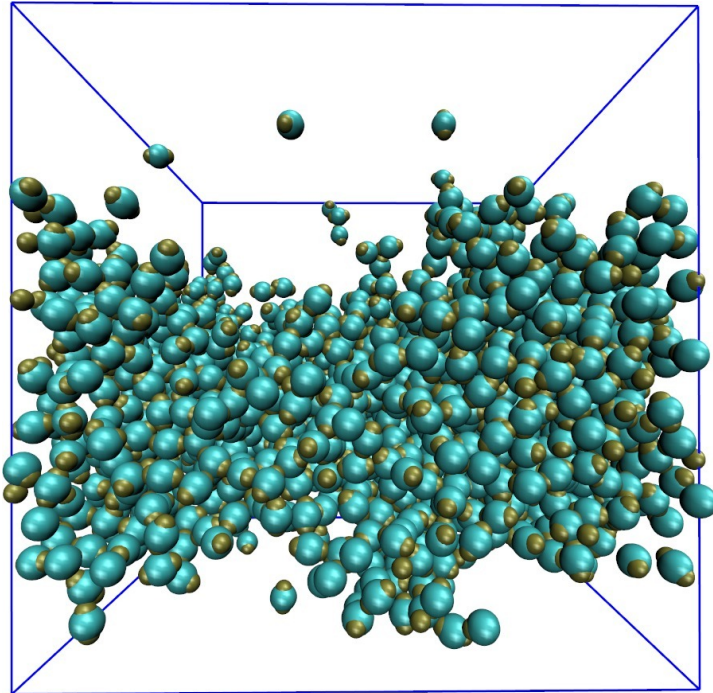


Figure 4.1: MD simulation snapshot of the 30n model for a state-point inside the coexistence region, where liquid and vapor separate.

disordered system where particles rearrange locally but do not diffuse; such a system is not thermodynamically stable, and in an infinite time would crystallize, however in simulation time is metastable. Analogously, at higher density ranges the system is incapable to self-assemble in any ordered, stable structure, and forms a glass, i.e. a disordered metastable phase where no movement happens.

It is important to note that, although the models discussed in this section do not self-assemble, it does not mean that they do not have ordered phases at all, just that these phases are not obtainable via simple self-assembly. Other studies using more sophisticated methods (see references [Dop12, DNBK12, NKD<sup>+</sup>14, NB15] for details) indeed found crystal structures at patch amplitudes less than  $42^\circ$ . At high density, all models would crystallize in

a face-centered cubic lattice [Dop12], and the g38n model (discussed in § 2.4) forms a very interesting phase composed by planar layers [NKD<sup>+</sup>14, NB15]. But again, the aim of this work is to study the phases that can self-assemble in MD simulations.

In our study of the fluid phase, we investigated the dynamics by means of the autocorrelation functions, measured in simulations, and tried to predict the thermodynamics and the static structure using liquid-theory methods. The first liquid-state theory used is the very simple Barker-Henderson thermodynamic perturbation theory (TPT) [BH67, GRSG12] introduced in § 3.4.2; these calculations were carried by the author of thesis, who also fully implemented the code. The second method is based on integral-equations theories, and uses the so-called reference hypernetted chain (RHNC) method [Lad82, GLL<sup>+</sup>09, GLL<sup>+</sup>10, GGL<sup>+</sup>14] that we introduced in § 3.4.1. Also these results were computed by the author of the thesis, but the using the last version of the code written by F. Lado [GGL<sup>+</sup>14]. Finally, the third method is the associative Percus Yevick theory (APY), based on a diagrammatic expansion of the potential within the so-called Wertheim theory [Wer84a, Wer84b, Wer86a, Wer86b, Wer87]. It was developed and implemented by Y. Kalyuzhnyi [KBFK15].

The data discussed in this section was published in references [KBFK15, FBKK15].

#### 4.1.1 Phase diagram

The phase behavior of all the small-patch models is very similar: they have a liquid-vapor phase separation and they do not self-assemble into ordered structure by annealing within the density range  $\rho^* \in [0.1, 0.8]$ . As an example, figure 4.2 shows the phase diagram of the 30n model.

#### 4.1.2 Dynamics

We studied the dynamics via the correlation functions defined in § 3.3.1: the mean squared displacement  $|\Delta\mathbf{x}(t)|^2$ , the autocorrelation of the velocity  $c_v(t)$ , and the orientational autocorrelation function  $c_n(t)$ . The orientation is defined as the direction joining the two patches. As already said, all the short-patch model were studied in the fluid phase only, and the correlation functions of different models presented similar behaviors. There is thus no need to present each model in depth, and we describe the dynamics of the 30n model as a general example for all models.

All the data are collected in figures 4.3 and 4.4, which are taken from reference [FBKK15]. The upper panels of figure 4.3 show  $c_v(t)$  for selected temperatures and densities. The curves at high temperatures show a monotonous decay, while for the lowest values of  $T^*$  a rebound mechanism takes place, signaled by negative values of  $c_v(t)$ . The shape of the curves is independent of the density, but decay becomes faster for increasing densities. These are all standard features seen in most fluids; nothing remarkable is learnt from the velocity autocorrelation function. On the other hand, a very interesting feature can be observed in the orientational autocorrelation function  $c_n(t)$ . As can be seen in the lower panels of figure 4.3, short-times ripples are present at the lowest temperatures and for every density: this is a hint of orientational vibrations undergone by the particles. In the next section,

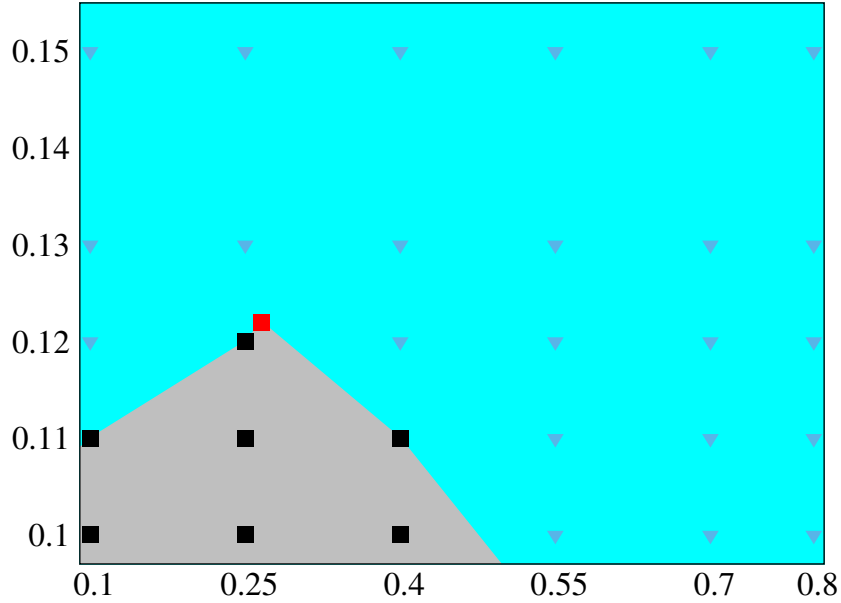


Figure 4.2: Phase diagram of the 30n model in the  $T^* - \rho^*$  plane, as obtained via MD simulation. At the statepoints denoted by the blue triangles the system was found in a pure phase, while liquid-vapor coexistence was observed in the statepoints indicated by the black squares. The red square is the critical point of the vapor-liquid transition, as obtained via Grand Canonical MC simulations performed by E. Bianchi [FBKK15]. The background colors are guides for the eye.

dedicated to the models with  $\gamma_1 = 45^\circ$ , we shall see how these vibrations will evolve in an ordered phase where IPCs have fixed spatial position and preferred orientations.

The left panel of figure 4.4 shows the diffusion coefficient  $D$  versus density at different temperatures. As expected,  $D$  shows a monotonous decrease with decreasing temperature and raising density. In the right panel of figure 4.4 the same data is plotted along the phase diagram in the temperature-density plane, in terms of the isodiffusivity lines. The region of dynamical slowing-down is often defined as the region where  $D \lesssim 10^{-4}(2\sigma_C)^2/t_0$ , and for our model is localized in the low  $T^*/$ high  $\rho^*$  region of the phase diagram.

### 4.1.3 Static structure

As explained in chapter 3, integral equation theories describe the structure of the fluid in terms of the pair correlation function  $g(r)$ , which gives information about the spatial distribution of particles. Once the  $g(r)$  is known, the excess energy and the pressure can be computed as weighted integrals of the  $g(r)$  (see § 3.4.1 for RHNC, and reference [KBFK15] for APY). It is thus of crucial importance that this spatial correlation function is faithfully reproduced.

Figure 4.5 shows the  $g(r)$  for three different models: simulation data is compared to theoretical results. The first column shows the  $g(r)$  for model M1, which has a short interaction range ( $\delta/2\sigma_C = 0.1$ ) and a small patch semi-amplitude ( $\gamma = 22.3^\circ$ ). The second column

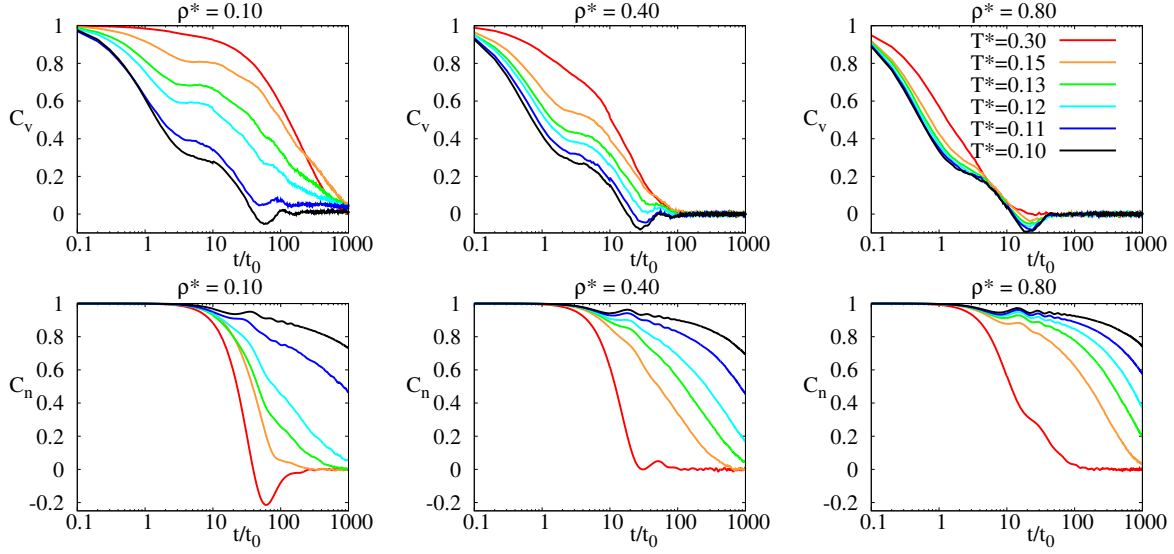


Figure 4.3: MD results for the velocity (top panel) and orientational (bottom panel) autocorrelation functions at several temperatures and densities (as labeled). Reprinted from [FBKK15].

shows the  $g(r)$  for model M2, whose interaction range is longer ( $\delta/2\sigma_C = 0.3$ ) and the patch amplitude  $\gamma$  is almost twice that of model M1:  $43.5^\circ$ . Finally the third column shows the  $g(r)$  for model 30n, with intermediate values for both the interaction range and patch semi-amplitude ( $\delta/2\sigma_C = 0.2$ ,  $\gamma = 31.1^\circ$ ). The simulation data comes from MC for models M1 and M2, and MD for model 30n.

The first two columns of figure 4.5 present the  $g(r)$  for models M1 and M2 computed at the same statepoints. The top panels show data at high temperature ( $T^* = 0.50$ ) and low density ( $\rho^* = 0.20$ ) state, while in the second and third row the density is higher ( $\rho^* = 0.45$ ) and the temperature is progressively lower ( $T^* = 0.23$  and  $0.18$ ). Both RHNC and APY excellently reproduce the pair distribution function for model M1, the one with the shorter  $\delta$  and smaller patch, at all presented temperatures and densities. At  $\rho^* = 0.45$  it can be noted that APY shows small deviations in the second neighbor peak, while RHNC correctly reproduces this feature. For model M2 there is also a good agreement, but more discrepancies arise. RHNC again reproduces better the shape of second neighbor peak, but is unable to converge numerically at the lowest temperature; on the other hand, APY reproduces more faithfully the valley between the first and second peak and converges for all the presented statepoints. The capacity of APY to converge at lower temperatures than RHNC is evidenced in the study of model 30n, presented in the rightmost column of the figure. This system is studied at lower  $T^*$  and higher  $\rho^*$  than models M1 and M2. In this case RHNC does not appear in the plots because it does not converge at temperatures  $T^* < 0.15$ , and only APY could be compared with the simulation data. Here we see that, although the description of the second peak is far from perfect (especially at the lowest temperature), the range  $2\sigma_C < r < 2\sigma_C + \delta/2$  is very faithfully reproduced. Quality of the  $g(r)$  in this range is the main goal of integral equation theories, because pressure and energy are obtained as integrals of the  $g(r)$  from  $2\sigma_C$  to  $2\sigma_C + \delta/2$ .

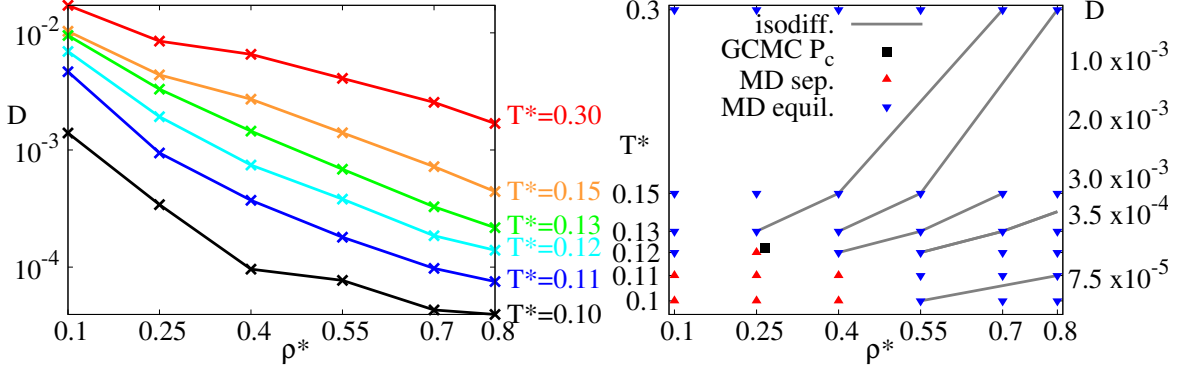


Figure 4.4: Left: MD results for the diffusion coefficient  $D$  along several isotherms (as labeled). Right: phase diagram of the system along the isodiffusivity lines. The highlighted points correspond to the numerically investigated statepoints: a red upward triangle denotes a phase separating system, a blue downward triangle corresponds to a homogeneous fluid, and the black full square symbolizes the critical point. Along the gray curves the value of the diffusion coefficient  $D$  is constant and decreases from  $10^{-3}$  to  $7.5 \cdot 10^{-5}$  in units of  $(2\sigma_C)^2/t_0$ . Reprinted from [FBKK15].

How do the deviations arise? RHNC describes the bridge function of the model as an “equivalent hard sphere” [Lad82]; the more anisometric<sup>2</sup> the systems is, the less the RHNC approximation is valid. On the other hand, APY strongly relies on two approximations. The first is the single-bonding approximation, i.e. each patch interacts with the center of only another particle; this approximation is reasonable if the patch is small, and ceases to be valid if the patch amplitude becomes too large. The second approximation lies in the treatment of the patch-patch repulsion, which are neglected in the expansion of the potential and then added back in the solution of OZ equation. It was argued [KBFK15] that this leads to the imprecision in the description of the second peak.

Only for model 30n, we compared APY to MD simulation data not only using the  $g(r)$ , but also the static structure factor  $S(k)$ . While the  $g(r)$  captures the short range details, the  $S(k)$  evidences long range spatial correlations: being able to describe both limits is a very good test for an integral equation theory. It is important to note that, in APY, the  $g(r)$  is obtained through a Fourier transform of the  $S(k)$ , while in the simulation  $g(r)$  and  $S(k)$  are measured using two independent procedures. The results are shown in figure 4.6. The agreement between theory and simulation data is excellent, even at the lowest temperature.

The careful reader will notice that the simulation data of the  $S(k)$  is more noisy than that of the  $g(r)$ : the reason lies in the measurement method. Equation (3.32) accumulates  $N(N-1)/2$  statistically independent data points, one for every possible couple of IPCs, from each simulation frame. These data points must be divided between the bins in which  $r$ -axis is discretized; since we sampled 5000 frames and 2048 IPCs in a simulation box whose side was between 15 and 30 (in units of  $2\sigma_C$ ), distributing the points in bins of length between 0.05 and 0.02 still leaves about a million of statistically meaningful data points in every  $r$ -bin, which is a good statistical sample. On the other side, equation (3.34) can accumulate from each simulation frame only a single statistically independent point for every value of  $k$  that

<sup>2</sup>Anisometric = different from an hard sphere.

## 4 Results

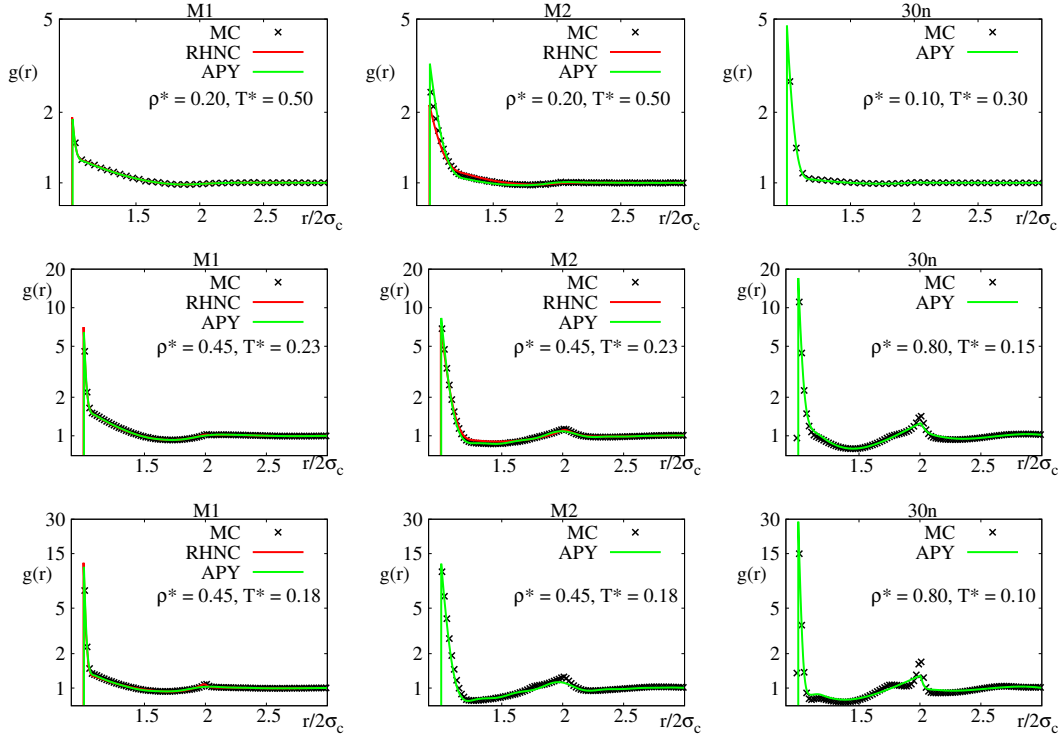


Figure 4.5: Pair correlation functions  $g(r)$  for models M1 (left column), M2 (central column) and 30n (right column), at selected statepoints (as labeled); note the logarithmic scale of the vertical axis. Crosses correspond to MC simulation data for models M1 and M2 and to MD data for model 30n; green lines represent APY results and red lines RHNC results.

is sampled; since we sampled 5000 frames this amounts to only 5000 statistically meaningful points in every  $k$ -bin. The reader might wonder why this method is used at all, if it turns out to be so inefficient compared to calculating the  $g(r)$  and then Fourier transforming it. The reason is that, to obtain good precision at small  $k$ , the long-range values of the  $g(r)$  are needed, but the simulation  $g(r)$  is only known up to a finite range and, especially at high densities, it might be unpractical or even impossible to simulate a system of the necessary size.

### 4.1.4 Thermodynamics

In integral equation theories, pressure and energy are obtained as integrals of the  $g(r)$  over the range  $2\sigma_C < r < 2\sigma_C + \delta/2$  (i.e. the interaction range). Because of the excellent agreement between simulation data and theoretical results met in the interaction range, it is natural to expect an agreement of the same quality for the thermodynamics. Moreover, RHNC had a better agreement with simulation data for model M1, and APY was better for model M2; one would expect this trend to be reflected also in the thermodynamics. Instead, the opposite is observed: RHNC turns out to work better for model M2, while APY gives better results for model M1. In addition, the TPT was used, to show how another approach, not based on integral equations, compares with RHNC and APY.



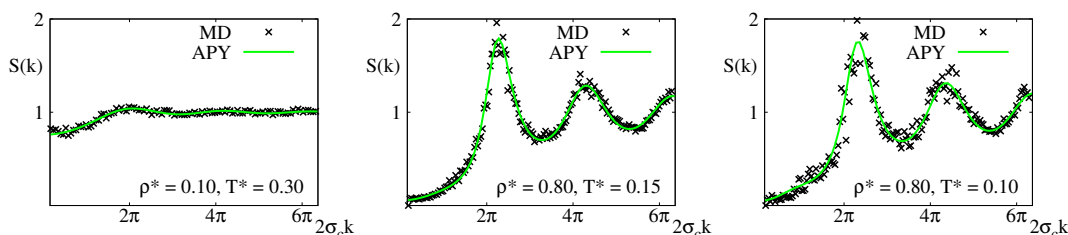


Figure 4.6: Static structure factor  $S(k)$  for model 30n at selected statepoints (as labeled). Crosses represent MD simulation data, green lines are APY results.

The results are summarized in figure 4.7: energy in left column, pressure in the right, and each row shows a different model, M1, M2 and 30n.

The curves for the energy  $u^*$  are presented in the left column of figure 4.7. Both theories have an excellent agreement with simulation data at  $T^* = 0.50$  and  $0.32$ ; however, RHNC underestimates the simulation data at the lower temperatures for model M1, while APY overestimates the simulation data at high density for model M2. This is the opposite behavior to that seen in the data for the  $g(r)$ ! The explanation is that neither technique uses only the plain center-center  $g(r)$  to compute the integrals: APY uses three site-site correlation functions – center-center (the  $g(r)$ ), patch-center, and patch-patch – each with appropriate weights, while RHNC uses a spherical harmonics expansion of the angular dependent distribution function of which the  $g(r)$  is just the isotropic component (see § 3.4.1). Hence, the quality in the other site-site correlation function for APY, and in the other components of the direction-dependent distribution function for RHNC, will influence the thermodynamics beyond the simple center-center radial  $g(r)$ .

Similar observations can be made for the pressure: for model M1 all theories – now including the TPT – give a good result for  $T^* \geq 0.32$ ; but for  $T^* \leq 0.23$  only APY is able to reproduce the correct result, while both TPT and RHNC deviate by quite a large amount. Passing from model M1 to model M2, we see the same behavior that was observed for the energies: both integral equations theories work well for  $T^* \geq 0.32$ , and for  $T^* = 0.23$  RHNC is slightly closer to the MC data, while APY deviates from it, although less than RHNC did for model M1. At  $T^* = 0.18$  APY gives a result of poor quality, while RHNC does not even converge. The TPT data are not even shown for model M2 because the results deviate by an entire order of magnitude, showing that this simple perturbation theory is unsuited for the description of a complex model such as IPCs.

For model 30n, no pressure data are available, and only the energies are shown in the picture, compared with APY. The reduced temperature was extended to lower values than in the previous models, and RHNC did not converge. The agreement between simulation and APY data is remarkably good even for the half of the  $T^* = 0.10$  along the values in the liquid branch; the other half of this isotherm is not shown because the system is phase-separating, and integral equations are not applicable in the coexistence region. Data for the pressure for model 30n are not shown; to compute the pressure in the MD simulations, the virial had to be extended to include the contributions due to the Ciccoti algorithm; unfortunately there is no standard expression for it in the literature, and the derivation turned out to be a very

challenging task that the author of the thesis was unable to solve.

#### 4.1.5 Small-patch models: summary

The small patch models did not self-assemble into ordered structures, thus were used to test the application of APY and RHNC integral equation theories. From the data we concluded that each theory is better suited to describe different properties ( $g(r)$ , thermodynamics) for different model parameters. However we can conclude that APY is more reliable, in the sense that it converges for lower temperatures, and presents deviations from the simulation data that are in general smaller than RHNC.

Another important feature that we met were the oscillations in the orientational correlation function  $c_n(t)$ , that originate from the vibrations of the IPCs, and will be encountered again in the crystal-liquid phase presented in the next section.

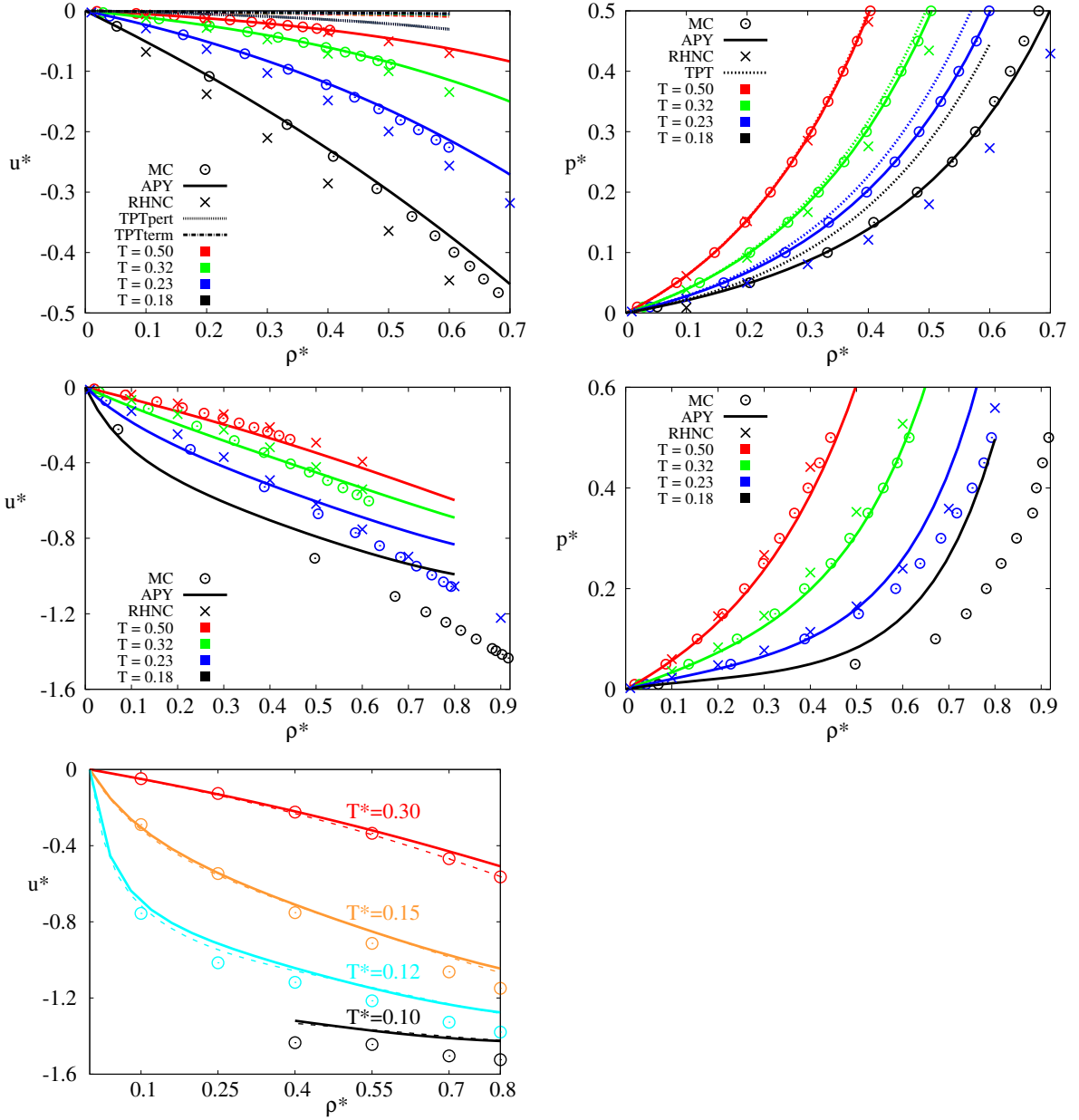


Figure 4.7: Energy  $u^*$  and pressure  $p^*$  versus density  $\rho^*$  for different models. Energies are shown in the left column, pressures in the right one. The first row shows results for model M1, the second for model M2, and the third for model 30n. Different colors denote different temperatures. For models M1 and M2: open circles – MC data, continuous lines – APY results, crosses – RHNC results, dashed lines – TPT results (where convergent). For model 30n: open circles – MD data, continuous lines – APY results with hard sphere, dashed lines – APY with soft sphere.

## 4.2 Models with $\gamma_1 = 45^\circ$

In this section we present models in which the amplitude of one of the patches is fixed to  $\gamma_1 = 45.6^\circ$ . In the most simple case, the other patch is symmetric, and IPC total charge is zero; this model is called 45n, and it spontaneously self-assembles into an interesting ordered structure that will be presented in § 4.2.1. Its phase diagram is presented in § 4.2.2, and its dynamics in § 4.2.3. In § 4.2.4 we study symmetric models in which either the center or the patches are overcharged; if the other patch is symmetric in size we refer to them as 45sQc. In the last subsection, § 4.2.5, we analyze asymmetric models and check for which values of  $\gamma_2$  the ordered structure is still stable.

The initial input to this line of research came from previous studies that showed that IPCs with medium-sized patches could crystallize into a hexagonal lattice [BLK13] in two-dimensional confinement and into planar structures in three dimensions [NKD<sup>+</sup>14, NB15]. These studies were already discussed in § 2.4 so we will not repeat the description here, but we will remind the reader that in the three-dimensional planar lattice studied in reference [NKD<sup>+</sup>14, NB15] the layers repel each other and align parallel.

In another reference [Dop12], a termed called 38n (overall neutral,  $\gamma = 38.6^\circ$ ,  $\delta/2\sigma_C = 0.25$ ) was found to be stable at zero temperature in a phase formed by planes stabilized by IPCs aligned perpendicular to the IPCs in the planes. The structure is shown in figure 4.8; the density of the system is relatively high ( $\rho^* \simeq 0.88$ ), outside what we defined as the “fluid region” in the last section. The models presented in this section self-assemble in a structure similar to this one, but with a larger lattice spacing (and thus a smaller density).

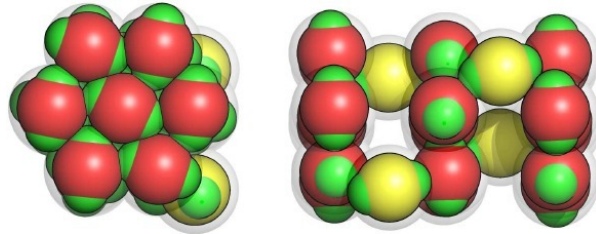


Figure 4.8: Snapshot of a structure formed by model 38n (reprinted from [Dop12]). Compare with the structure formed by model 45n in figure 4.9.

### 4.2.1 The crystal-liquid structure formed by model 45n

Since a picture is worth a thousand words, we start this subsection by inviting the reader to check figure 4.9, that presents a snapshot of the structure in which this model spontaneously self-assembles. This structure represents the most relevant novelty discovered in this thesis: even though layer and interlayer IPCs are exactly the same kind of particles, they behave like two different species within the temperature range  $0.045 < T^* < 0.135$ : the layers are found in a crystalline state, while the interlayers behave like a fluid. This behavior is not due to excluded volume effects: we carried out simulations with a density smaller than the one that would allow for a perfect filling of the simulation box, and we witnessed the formation of the same structure in coexistence with gas, as presented in figure 4.10. It is important to notice that the layer-layer distance is independent of density and temperature and characteristic for the phase. This also holds for the ratio of the number of particles in the layers and in the

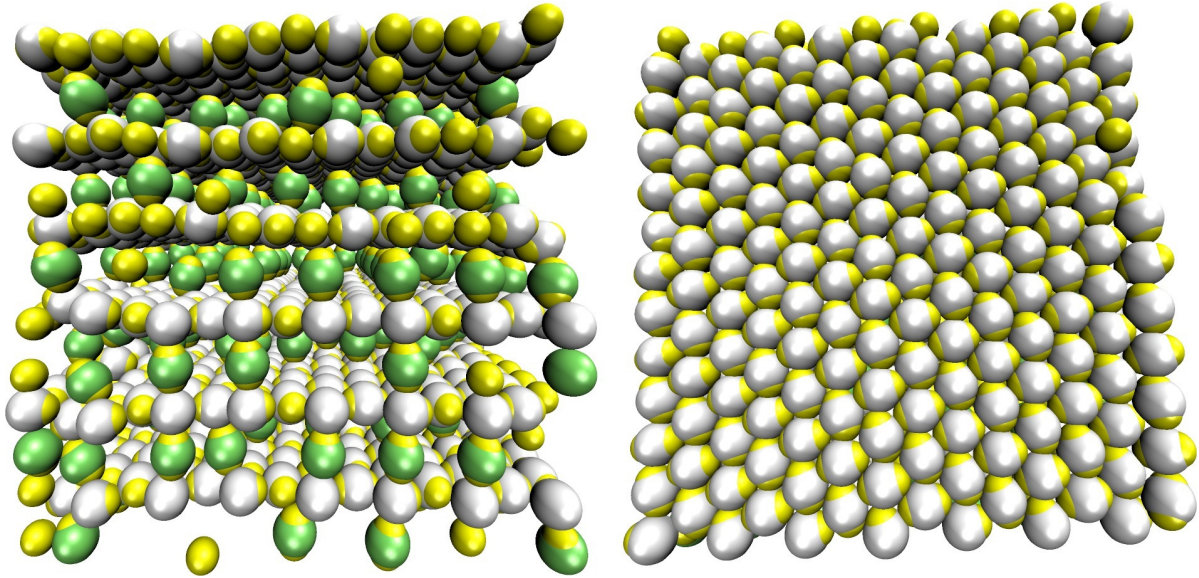


Figure 4.9: Snapshot of a simulation of the 45n model at density  $\rho^* = 0.75347 \dots$ , side view (left) and bird's eye view (right). The gray IPCs, that form the planar layers, are stable in their positions and orientations, and can only vibrate. The green IPCs, confined between the layers, are energetically forced to align orthogonally to the plane; at low temperatures they are fixed on the positions on top of the bellies of some of the IPCs in the planes, however when the temperature is sufficiently high they can diffuse along some minimum potential lines. We term this phase where the green IPCs are mobile as the **crystal-liquid phase**.

interlayers.

The interlayer fluid particles do not enter the planes after they are ready, instead they have an active role in the formation of the layers, that we discovered analyzing the trajectory movies. After an initial hexagonal plane has self-assembled, another plane would be repelled by it because the equators of the IPCs in the two planes would be facing each other, as it is the case in the model g38c studied in reference [NKD<sup>+</sup>14]. On the other hand, single IPCs are attracted by the plane because they are free to align their patches to point towards the plane, and form an attractive layer that acts as a coating of glue on which a second hexagonal plane can adhere.

We obtained the crystal-liquid structure by annealing a high-temperature gas. The crystal-liquid structure forms at a temperature between  $T^* = 0.13$  and  $T^* = 0.14$ . We checked the temperature using NVT Montecarlo direct coexistence simulations: we filled a rectangular simulation box with IPCs in the crystal-liquid structure, then we froze the particles in a half of the simulation box, while melting the IPCs in the other half. This setup was then equilibrated at constant temperature. Snapshots of this method are shown in figure 4.11. This transition temperature is consistent with the one we observed also in the MD simulations.

The reader might notice from figures 4.9, 4.10 and 4.11 that the ratio of the number of interlayer IPCs to layer IPCs is always the same. The ratio, in a perfect structure, would be of two IPC in the interlayers for every nine IPC in the layers. This number was checked through another NVT Montecarlo direct coexistence simulation: half of the simulation box was filled with IPCs in the fluid phase, and the other half with a crystal-liquid structure in

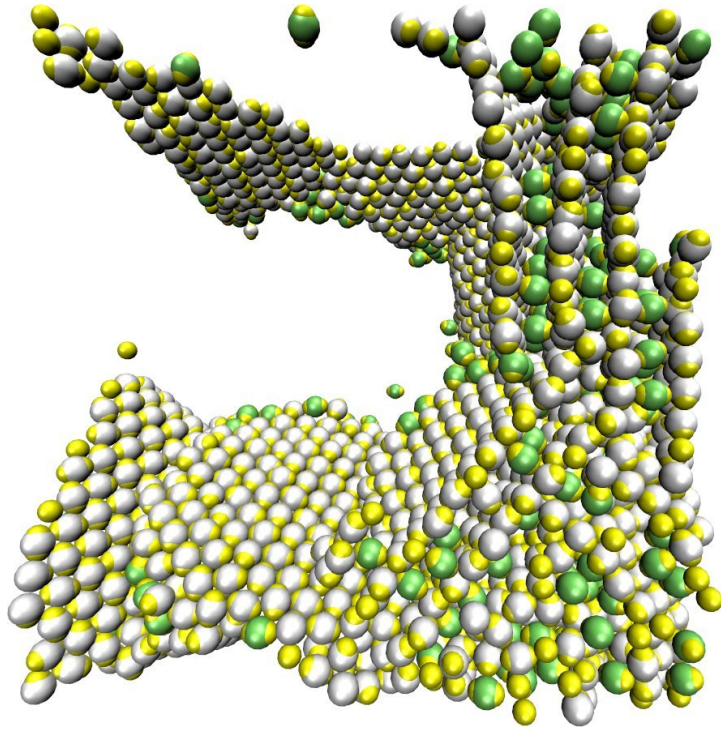
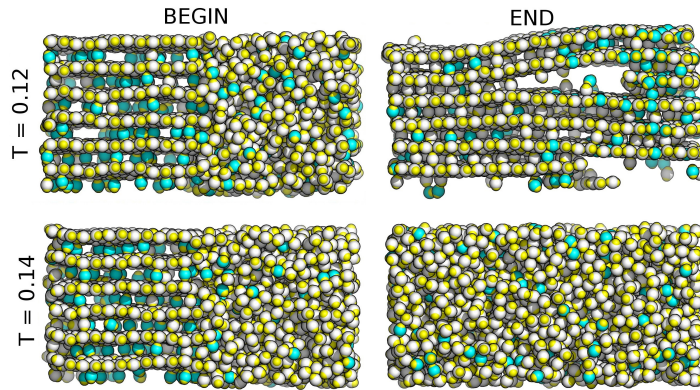


Figure 4.10: Snapshot of a simulation of the 45n model. Here the density is lower than in figure 4.9: the crystal-liquid structure still forms in a small spatial region, leaving the rest of the simulation box almost empty – i.e. a very low density gas.

Figure 4.11: An NVT Montecarlo direct coexistence simulation between the crystal-liquid structure (in the left side of the simulation box) and the liquid phase (in the right side of the simulation box). To enhance visibility, the IPCs that were in the interlayers at the beginning of the simulation (before the initial melting) are depicted in turquoise.



which the interlayers were under/over-filled. The part of the system in the crystal-liquid phase absorbed IPCs from the liquid (or ejected the surplus of IPCs into the liquid) until it reached the ideal ratio of particles.

The dynamic behavior of the interlayer particles changes radically with the temperature. A transition is located around  $T^* \simeq 0.045$ : below this temperature, interlayer IPCs remain in a fixed position and do not move, while above  $T^* \simeq 0.045$  they diffuse, and their mobility increases with raising temperature. It worth noting that the ratio between this transition temperature and the one at which the layers melt (i.e.  $0.045/0.135 \simeq 1/3$ ) gives the same numerical value of the ratio between of the binding energies of interlayer and layer IPCs in a perfect lattice ( $-1/3$ ), suggesting a link between binding energies and melting temperatures of the layers and interlayers.

As just stated, interlayers IPCs are frozen at  $T^* \lesssim 0.045$ . The orientation of the IPCs is

aligned perfectly orthogonal to the planes, and the patches are placed on top of the equators of the IPCs in the layers, if no defects are present. To better explain this phenomenon, we show in figure 4.12 the potential energy landscape felt by a single interlayer IPC between two layers at three different distances (the middle position between the layers, and two positions slightly closer to one of the layers) assuming three different orientations (one perfectly orthogonal to the planes, the other two inclined). It can be seen that the global minimum is found when the interlayer IPC is located at a distance  $\sigma_C$  from both the two planes (since the distance between the two planes is  $2\sigma_C$ , the interlayer IPC is in exact contact with the layer IPCs, but without penetrating the hard sphere core) and orientated perfectly orthogonal to the planes; the interstitial regions between layer particles are slightly repulsive, and all the other positions are not as repulsive but also not as convenient as the minimum. Tilting of the particle is not convenient, because the potential decreases for every orientation not orthogonal to the planes. If the IPC is moved closer to one of the planes ( $z = 1.49$ , central column of the figure – this happens due to thermal agitation and/or lattice defects in the planes), the hard cores of the layer and interlayer IPCs come into contact, so the equatorial region of layer IPCs becomes repulsive for the interlayer IPC. Around this repulsive region, there is an annulus-shaped region of equivalent minimum positions: hence, when the temperature is raised and defects are introduced, the interlayer IPCs start to “dance”, moving inside the annulus. In addition, the energy barrier between different annuli at  $z = 1.49$  is lower than the one between the equatorial regions for  $z = 1.50$ ; thus whenever an IPC accumulates sufficient kinetic energy, it can jump from annulus to annulus (or even from annulus to equatorial region and viceversa, if defects are present and/or the temperature is sufficiently high). Interlayer IPCs start having enough energy to jump between minima (equatorial regions or annuli) at  $T^* \simeq 0.040$ , but the jumps are sporadic and only at  $T^* \gtrsim 0.045$  this phenomenon happens with a frequency sufficient to allow a real diffusion.

In the left column of figure 4.12, the interlayer IPC is moved even closer to the lower plane (i.e.  $z = 1.45$ ): the shape of the potential is qualitatively close to the configuration at  $z = 1.49$ , but the attractive regions are smaller and their energy is higher, so this configuration is unfavored.

The bottom panel of figure 4.12 shows the minimum (in the  $x - y$  plane) of the potential felt by the interlayer IPC as a function of  $z$ . The plot shows that, although an attractive region can be found at every distance from the planes, the global minimum of the energy is found when the interlayer IPC is located in the middle position between the two planes.

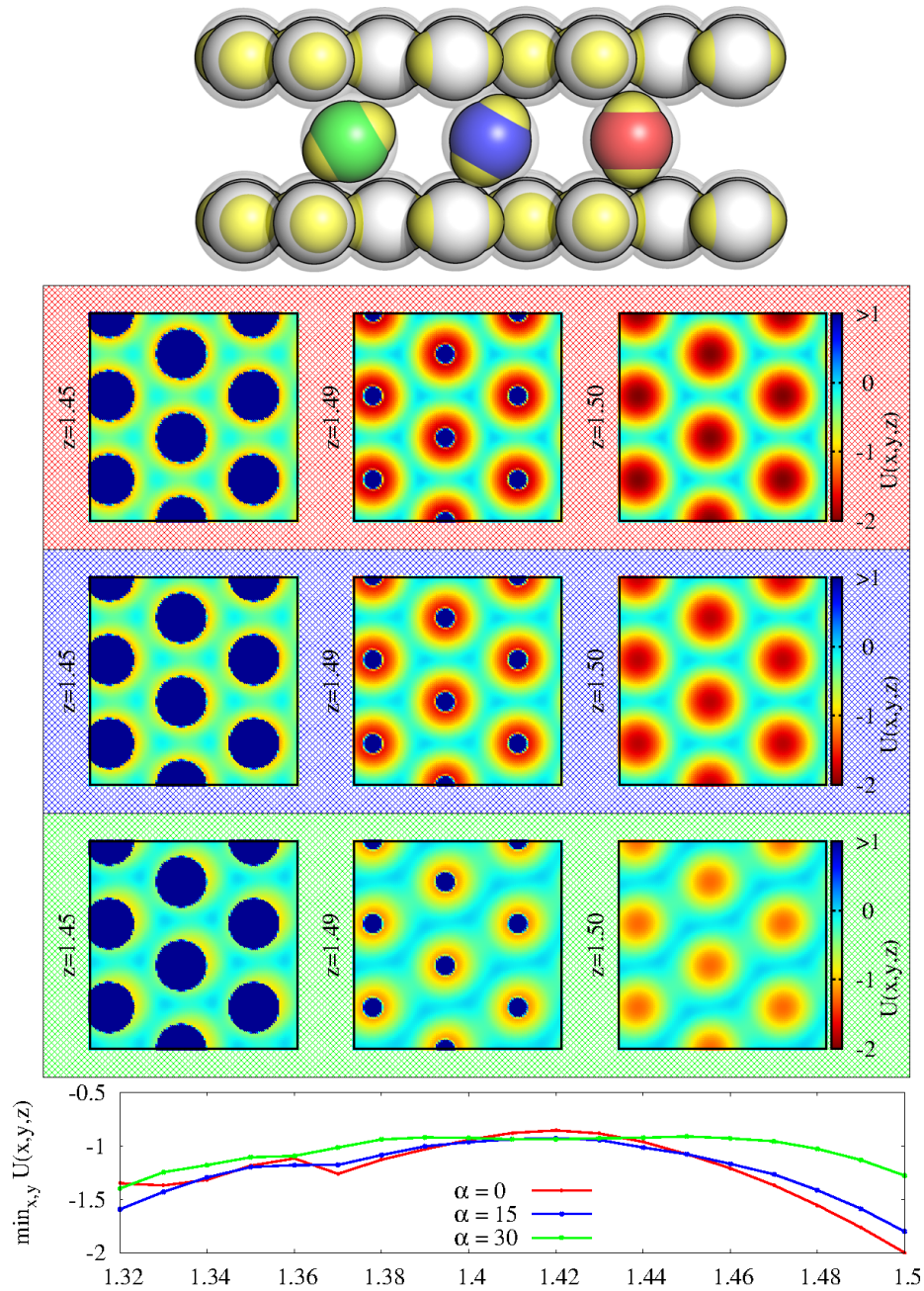


Figure 4.12: Contour plots of the potential experienced by a single interlayer IPCs at different orientations and distances from the planes. The snapshots at the top show the three orientations considered; the colors of the IPCs identify the inclination in the graphs below. In each row the panels show the potential for a single orientation at different distances ( $z = 1.45, 1.49, 1.50$ ); the lower plane is centered at 1.0 (in units of  $2\sigma_P$ ) and the second at 2.0, so  $z = 1.5$  is the middle position and the other  $z$  values are closer to the lower plane. Blue color in the contour plots should be regarded as inside the hard core of the IPCs. The graph immediately below the snapshots shows the depth of the absolute minima in the plane at fixed  $z$ , depending on the interlayer IPC height and orientation.



### 4.2.2 Phase diagram of the 45n model

The phase diagram in the  $T^* - \rho^*$  plane of model 45n is shown in figure 4.13. It can be seen that above  $T^* = 0.135$  the system is always found in the fluid phase. A small liquid-vapor coexistence region is found in the temperature range  $0.12 < T^* < 0.13$ , and for  $T^* < 0.12$  the system is found in coexistence between the gas and the solid (i.e. the crystal-liquid structure). Only at  $\rho^* = 0.75347$  the system is found in a pure solid phase. Higher values of the density were not explored.

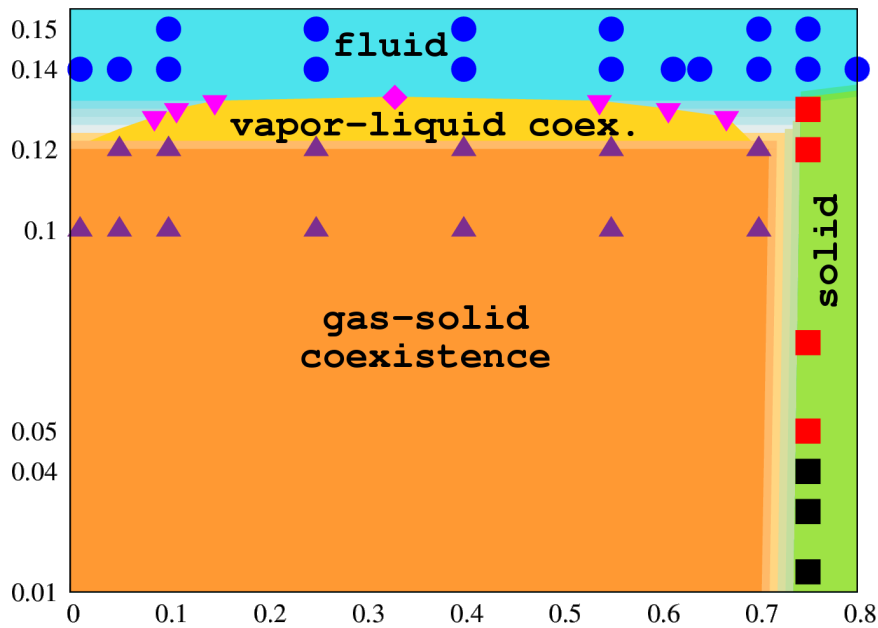


Figure 4.13: Phase diagram of the 45n model in the  $T^* - \rho^*$  plane. The statepoints indicated by the symbols were studied using simulations: From MD simulation we obtained the blue circles that denote a fluid phase, the squares that denote the ordered structure (crystal-liquid when red, crystal-frozen liquid when black) and the upwards violet triangles that denote coexistence between gas and solid. The pink downward triangles come from grand-canonical Montecarlo simulations and denote the the liquid-vapor coexistence line; the critical point is differentiated from the other points using a rhombus. This figure comes from a paper currently under publication process [FBK].

### 4.2.3 Dynamics of the 45n model

#### Some technical details

Before discussing the dynamic correlation functions, we have to introduce some technical details to the reader. Self-assembled crystals have many defects and planes are often tilted with respect to each other. A glance at figure 4.10 shows clearly what we mean: it is rather difficult to distinguish between layer and interlayer IPCs. A good criterion is checking the mean squared displacement of the particles, but this only works for  $T^* \gtrsim 0.045$ , when the interlayer IPCs diffuse. For  $T^* < 0.045$  the only possible criterion is to check the orientations,

and this is very difficult when the planes present defects. To circumvent the problem, we created a “perfect” lattice, where the planes were all perfectly straight and aligned parallel to the  $x - y$  plane. The interlayer IPCs were accommodated inside this structure: their  $z$  coordinate was chosen to be exactly in the middle point between pairs of layers, but their  $x$  and  $y$  coordinates were chosen randomly. The density of this configurations was the “ideal” one,  $\rho^* \simeq 0.75$ . This setup was equilibrated at very low temperatures: since  $T^*$  cannot be fixed in our MD simulations, a periodic rescaling of the temperature was necessary, otherwise the interlayer IPCs would acquire too much kinetic energy and impact with the layers creating defects. To do so, we put all the velocities to zero at regular intervals. We considered this “ground state” setup to be equilibrated when the system could be let evolve without any temperature drift even without the temperature rescaling. At the end of the equilibration, the (time-averaged) temperature was usually very low, in the range  $.005 < T^* < 0.011$ , the layers did not present defects, and the interlayers IPCs had moved from the random position in which they were initially placed to the equilibrium positions on top of the equators of the IPCs in the layers.

Since we wanted to study statepoints of higher temperature, we had to rescale the velocities so that the temperature would move to a slightly higher (or lower, in the rare instances in which we cooled) value, let the system equilibrate (again in the sense of no  $T^*$  drift), and repeat these two rescaling and equilibration steps until we reached the desired  $T^*$ . The rescaling of the velocities were kept small to minimize the formation of defects. When the system finally equilibrated at one of the desired temperatures, longer simulation were performed and the observables were sampled.

#### Dynamic correlation functions

We will now describe the observables measured using the method described in the previous §.

The mean squared displacement (MSD) is shown in the bottom panels of figure 4.14. At all temperatures, the MSD of the IPCs in the layers is quite small and does never exceed the value of 0.1 in units of  $(2/\text{sigc})^2$ . At  $T^* = 0.040$  and  $0.050$ , the figure shows not only the three-dimensional MSD, but also the MSD along the  $z$  direction and the one in the  $x - y$  plane. We can observe that the movement of the layer IPCs only happens in the  $z$  in the direction orthogonal to the planes while, on the other hand, the MSD of the interlayer IPCs shows that at low temperature these particles do not move, but when the temperature is around 0.45 they start to diffuse over a distance larger than their diameter; above this temperature they become mobile and the diffusion speed grows with temperature. Their movement is confined in the space between two parallel layers. The diffusion coefficients for both particle species are shown figure 4.15. Their growth is monotonous almost everywhere, except around the transition temperature where a surprise is found: both the layers and the interlayers show a small ripple. This is not a sampling mistake and was confirmed repeating the simulations; unfortunately we were not able to find an explanation.

Even more information is contained in the autocorrelation function of the orientation (ACN). The results are presented in the top panels figure 4.14. The red curves refer to the IPCs in the layers: it can be seen that the ACN has dumped oscillations with period

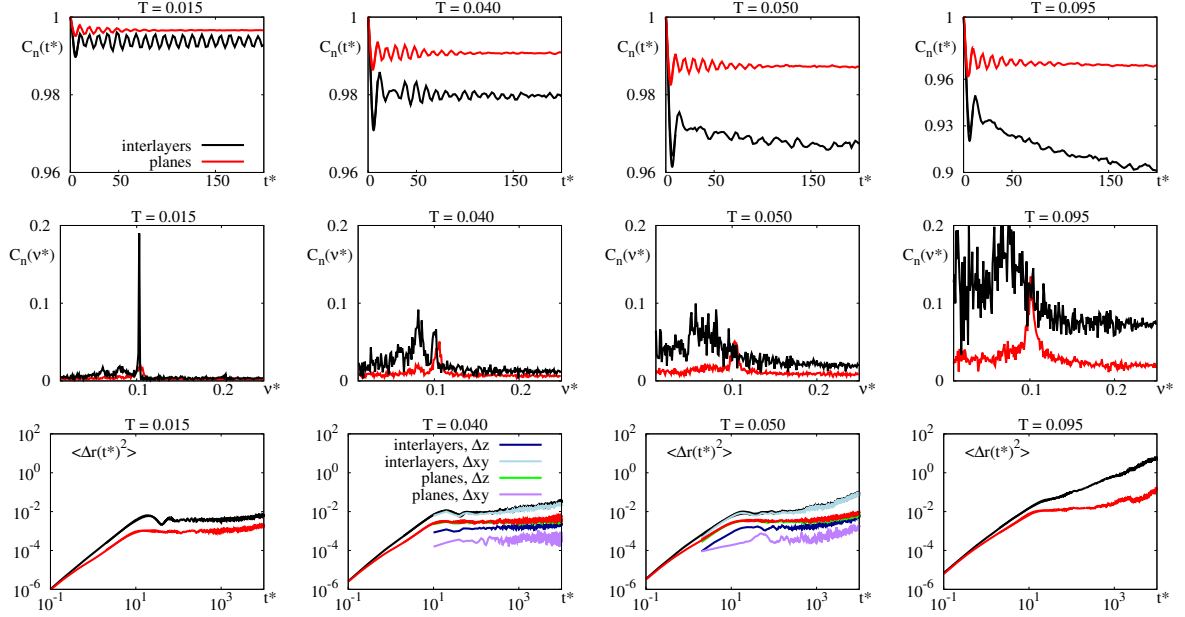


Figure 4.14: Correlation functions for model 45n. Top panels: orientational autocorrelation function at selected statepoints for the layer IPCs (red) and the interlayer IPCs (black). Middle panels: the Fourier transform of the orientational autocorrelation functions shown in the top panels, as functiona of the frequency  $\nu^* = 1/t^*$ . Lower panels: the mean squared displacement of the layer IPCs (red) and the interlayer IPCs (black). For the two temperatures around the transition, we also plotted the MSD in the  $x - y$  plane, and the MSD along the  $z$  direction.

$\tau^* = 10^3$ , around a constant value that decreases with temperature. A radically different behavior is found for the interlayer IPCs, whose ACN is drawn in black in the plots. At  $T^* \leq 0.040$  the ACN also oscillates around a constant value, but these oscillations are more complex than those of the layer IPCs: it is in fact the superposition of two modes. This can be better understood in frequency space, looking at the Fourier transforms of the ACN presented in the central panels of figure 4.14: two peaks can be identified, one, very sharp, is located at  $\nu^* = 0.1$  ( $\tau^* = 10$ ) and is the same oscillation that the layer IPCs undergo; the other, broader, is located at  $\nu^* = 0.08$  ( $\tau^* = 12.5$ ), is characteristic of the interlayers only, and becomes more pronounced as the temperature raises. The  $\tau^* = 10$  peak is due to the layer IPCs vibrating around their equilibrium orientation, and we suppose (but cannot prove conclusively) that the interlayer IPCs undergo the same oscillations when they are located in their global minima, i.e. on top of the equator of layer IPCs, aligned orthogonal to the layers. On the other hand, IPCs that are “dancing” in the annulus-shaped minima (explained in the previous subsection) present the second mode of oscillation.

At  $T^* \geq 0.050$  the interlayer IPCs ACN functions decay. As we learned from the MSD, at this temperature the interlayer IPCs start being able to diffuse in the  $x - y$  plane; at the same time, the oscillations are no longer peaked at  $\tau^* = 10$  and  $\tau^* = 12.5$ , become irregular with a continuous distribution of frequencies, as suggested by the Fourier transform. This is because they start hopping from minimum (equator or annulus) to minimum, and since defects are present in the lattice, their equilibrium alignment also has to change.

<sup>3</sup>We remind the reader that, as specified in the introduction, times  $t^*$  and time intervals  $\tau^*$  are expressed in units of  $t_0$ .

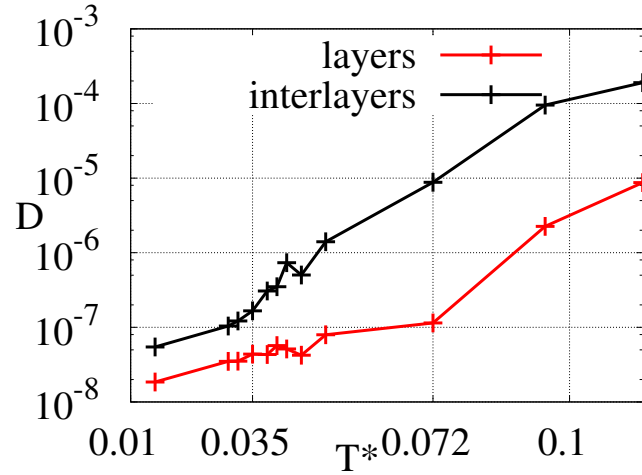


Figure 4.15: Diffusion coefficient for model 45n as a function of the temperature  $T^*$ . Black for the interlayers, red for the layers.

#### 4.2.4 Overcharging and undercharging of symmetric IPCs: 45sQc models

Up to now, the IPC charge has been overall neutral, i.e. the charge of each patch is half that of the central body. We now relax this condition and vary the charge of the center according to a simple formula:

$$Z_c = -\frac{30 + Q}{15} Z_p. \quad (4.1)$$

A positive value of  $Q$  makes the center proportionally more charged than the patches, and hence reduces the relevance of the patch-patch repulsion. For the same reason, a negative value of  $N$  makes the center-center repulsion less prominent. Values of  $Q$  such that  $Q \geq 8$  make the patch-center attraction so strong that the patches do not repel anymore; on the other hand, for  $Q < -3$  the center-center repulsion becomes so dominant that there is no longer attraction between patch and center.

It was shown in [NB15] that overcharge of the central body enlarges the region of stability in the  $p - T$  phase diagram of the layered structure that model 38n forms. For our models with  $Q \neq 0$  we did not explore in detail the phase diagram as we did for model 45n, but nevertheless we observed that the crystal-liquid structure did self-assemble more easily, in the sense that, by cooling an high-temperature gas, the layers self-assembled formed in a shorter simulation time than the 45n model. Under every other respect, overall charged and neutral models are equivalent: the shape of the lattice is exactly the same, and the dynamics too, as the reader can see in the correlation functions presented in figure 4.16: the interlayer IPCs present the same two peaks at  $\tau^* = 10$  and  $\tau^* = 12.5$  for  $T^* < 0.45$  and the decay for  $T^* > 0.45$ , as their neutral counterparts do.

#### 4.2.5 Models with asymmetric patches

The results presented in this section refer to models for which  $\gamma_1 = 45.6^\circ \neq \gamma_2$ . In section 4.1 we defined the orientation as the direction joining the two patches; now that the two patches are no longer equivalent, we still use that definition of orientation, and specify as “direction of the IPC” the direction pointed by  $45.6^\circ$  patch. As the reader can see in table 4.1,

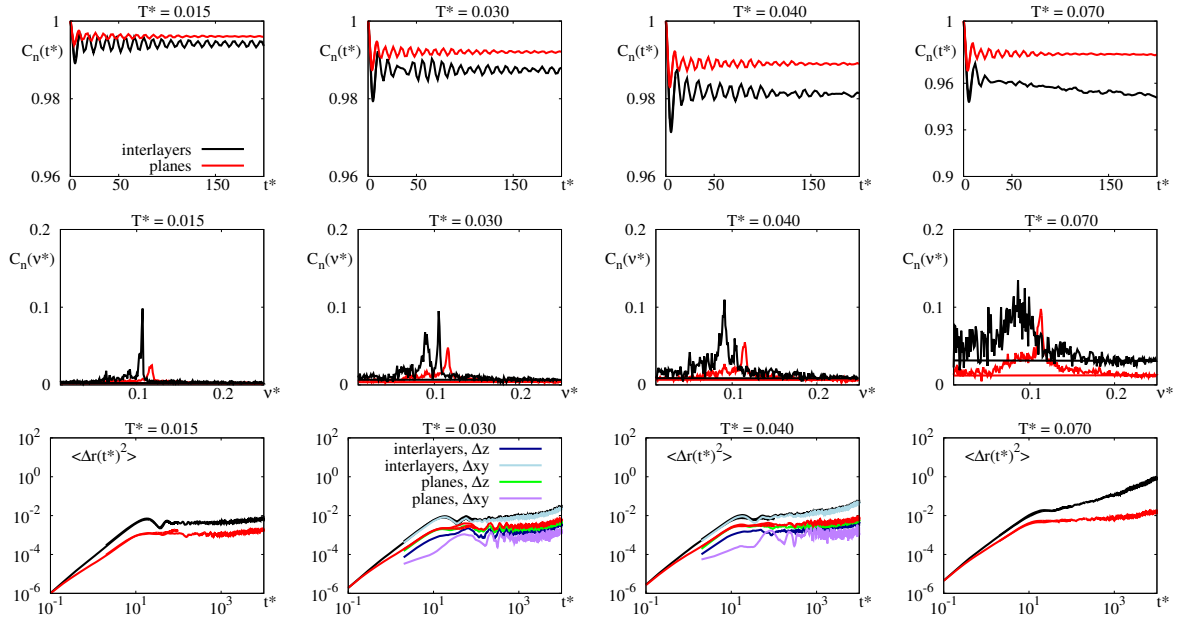


Figure 4.16: Correlation functions for model 45sQc. Top panels: orientational autocorrelation function at selected statepoints for the layer IPCs (red) and the interlayer IPCs (black). Middle panels: the Fourier transform of the orientational autocorrelation functions shown in the top panels, as functiona of the frequency  $v^* = 1/t^*$ . Lower panels: the mean squared displacement of the layer IPCs (red) and the interlayer IPCs (black). For the two temperatures around the transition, we also plotted the MSD in the  $x - y$  plane, and the MSD along the  $z$  direction.

we studied many models of patch amplitudes, however only those for which also the second patch is close to  $45^\circ$  crystallized.

How does the crystal-liquid structure change? The answer is surprisingly simple: the positions and orientations are still the same, and the directions of the IPCs are randomly distributed. Figure 4.17 shows, using the 3945n model as a reference, three possibilities in which a hexagonal plane could be arranged. In the left panel we can see that, along the diagonals defined by the cyan line in the figure, the patches of the same size face each other: the red line follows the direction pointed by the  $45.6^\circ$  patches (drawn in white) along a diagonal. Another possibility is presented in the central panel: this lattice is obtained by the one shown in the left panel by inverting the direction of the IPCs on every other diagonal. Finally, the right panel shows a configuration in which the directions are distributed randomly, obtained by self-assembly in a simulation. Although the three configurations appear quite different, they all share the same value of the energy per particle, and hence the one that will be realized in self-assembly is the one with the highest entropy, i.e. the one with the directions randomly distributed. Similar considerations hold for the interlayer IPCs: they might all align with the  $45.6^\circ$  patch pointing up, or down, or irregularly (some pointing up and some down); and since there is no energy difference between these three possibilities, the irregular alignment will be the one realized in simulation because of its higher entropy.

Neutral models with asymmetric patches self-assembled when the amplitude of their second patch was in the range  $36.2^\circ \leq \gamma_2 \leq 45.6^\circ$ . Model 3645n required a extremely long time

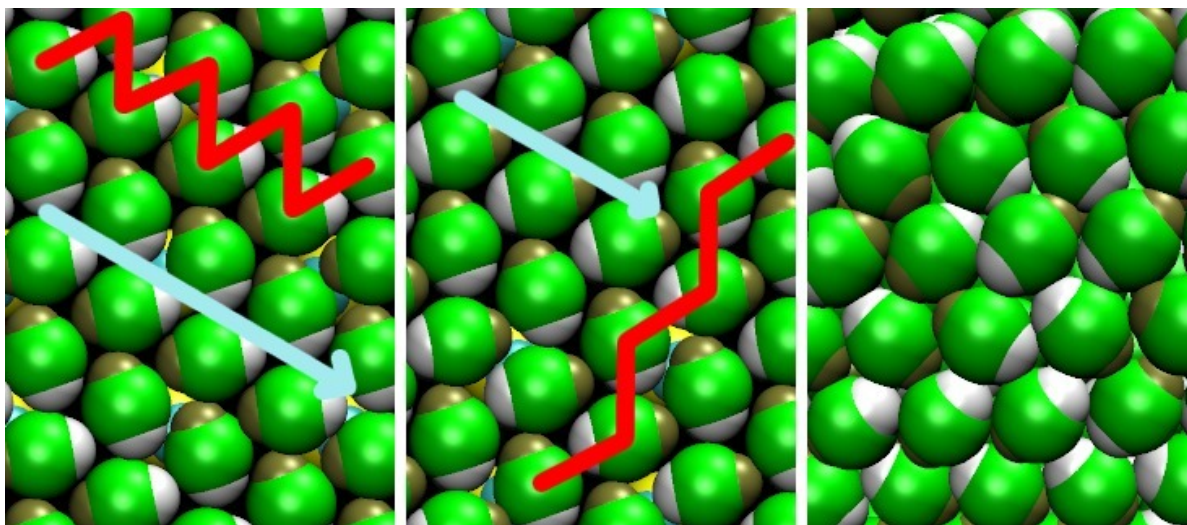


Figure 4.17: Three possible alignments of the patches in the hexagonal lattice (as explained in the text): two regular (left and center) and a disordered one (right). The  $45.6^\circ$  patches are colored in white, the  $39^\circ$  ones in brown. The cyan arrow denotes the direction defined as “diagonal” in the text; the red lines, that we drew to help the reader visualize the difference in the orientation of the patches, follow the directions pointed by the  $45.6^\circ$  patches.

to self-assemble via an extremely slow cooling procedure; however, it is remarkable that it did self-assemble, given how the large asymmetry and the small second patch amplitude. Other models with patch amplitude closer to the symmetric case, for example model 5045n, did not self-assemble at all. As we already put forward in the symmetric case, overcharging improves the stability of the layer phase. While the above-mentioned model 5045n did not self-assemble into the crystal-liquid structure, its charged version (5045c) did. This actually shows that the main obstacle to the spontaneous self-assembly of the crystal-liquid structure might be the patch-patch repulsion, whose relevance with respect to the center-center and patch-center interactions is reduced by the overcharging.

#### 4.2.6 45\* models: summary

Many of the the models presented in this section self-assembled in a novel phase –that was never observed before – composed by solid layers that behave like a solid, and particles between the layers that in the temperature range  $.045 \leq T^* \leq 0.125$  behave like a fluid, hopping between different minima. We studied dynamic correlation functions (ACN, MSD) to better understand the transition, and saw that the structure is also formed by asymmetric models where one of the patch has an amplitude different than  $45.6^\circ$ . Overcharging the colloid center enhances the stability of the crystal-liquid phase. We suspect that this is due to the reduced patch-patch repulsion.

### 4.3 Symmetric models with larger patch extension

For very large patch extensions  $\gamma \geq 49.5^\circ$  the crystal-liquid structure is no longer stable, and its place is taken by an FCC lattice with four independent orientations of the IPCs, shown from a side view in the left panel of figure 4.18. If the lattice were cut through one of the diagonals of the cubes, the planes at the interface would appear like the planes found in two-dimensional confinement [BLK14] that we presented in figure 2.6 from § 2.4, right panel. It is interesting to note that this FCC structure was predicted by Doppelbauer in his Ph.D. thesis [Dop12], using a neutral model with  $\gamma = 57^\circ$  and  $\delta/2\sigma_C = 0.25$ . In the same work he also studied a charged version of the same model, that had many other interesting stable phases, but unfortunately we did not succeed in self-assembling any of those.

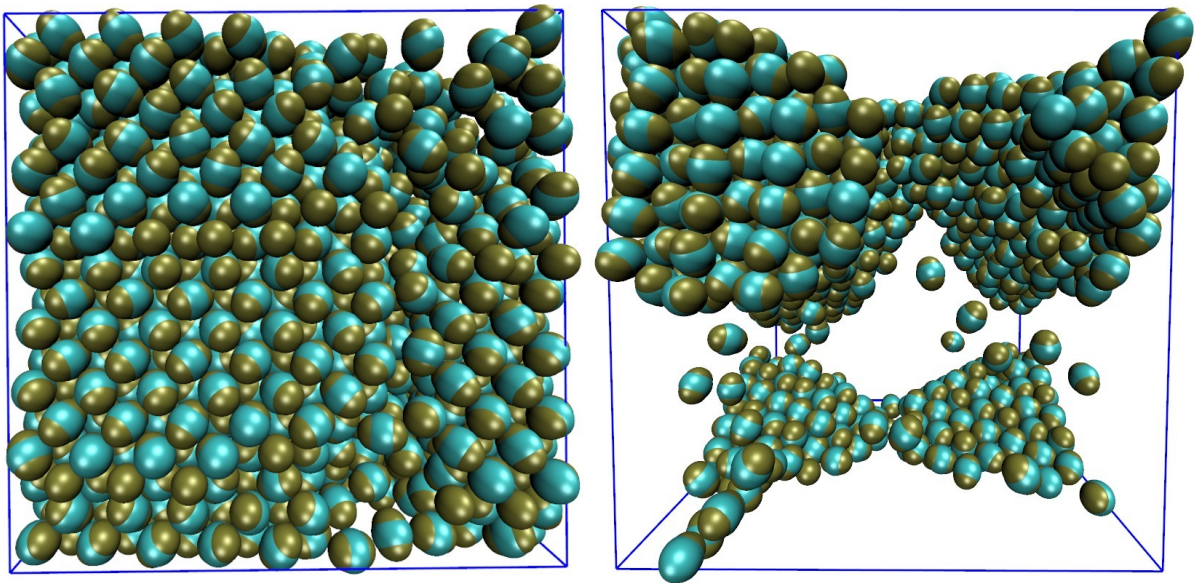


Figure 4.18: Snapshots of the face centered cubic structure formed by the 60n model. Left: a side view of a simulation at very high density ( $\rho^* = 1.0$ ), where the typical shape of the FCC can be identified. Right: a simulation snapshot at low density, where the interfaces present the hexagonal structure that was formed by the model also in two-dimensional confinement [BLK14].

The remarkable feature of this phase is that it is so energetically convenient with respect to a fluid phase, that it forms even at very low density in coexistence with gas, as can be seen in the right panel of figure 4.18.

#### 4.4 Completely asymmetric models

In this last section, we present some models whose patch amplitudes and charge distribution are chosen to extend to three dimensions the experimental results in two-dimensional confinement of van Oostrum (some are published in reference [vOHNR15], but a large part is still unpublished). The most interesting model is the 5040c whose parameters are chosen to mimic the experimental particles studied in reference [vOHNR15]. Despite the large asymmetry in the patches, this model still self-assembles in the crystal-liquid phase. A simulation snapshot showing the coexistence between the crystal-liquid phase and the low density fluid is presented in figure 4.19. It is important to note that the neutral equivalent (model 5040n) does not, again showing that overcharging stabilizes the ordered structure. We already observed this phenomenon for models 5045n and 5045c, where only the charged model self-assemble; however, in the case of the 5045c and 5045n models the patch had different amplitudes but carried the same charge, while in the case of the 5040c and 5040n models, the patches are asymmetric also in the charge.

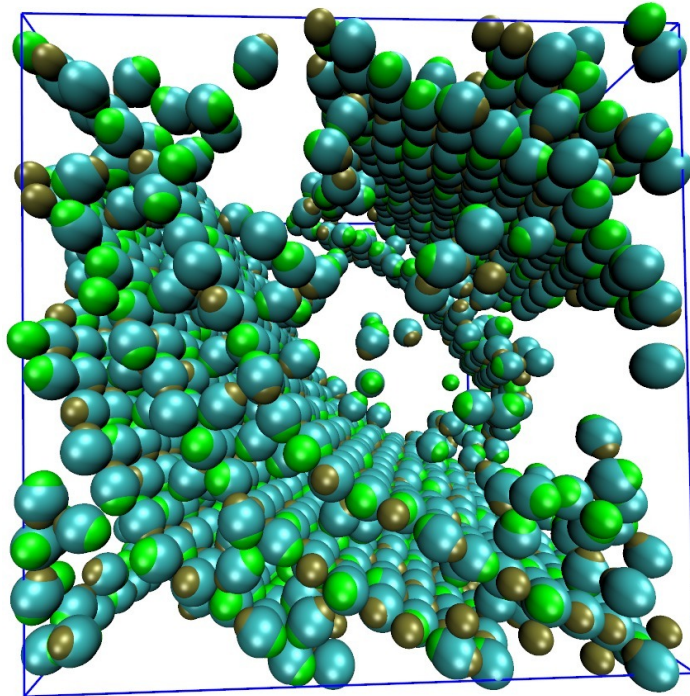


Figure 4.19: Snapshot from MD simulation of the model 5040c. This statepoint shows the coexistence between the crystal-liquid phase and a low-density gas.



## 5 Conclusions

In this thesis we studied colloids with a heterogeneously charged surface, referred to in the literature as inverse patchy colloids (IPCs) and first introduced in reference [BKL11]. While in conventional patchy particles the patches attract each other, in IPCs, due to the electric interaction between regions of like-unlike charge, the patches repel each other and attract the rest of the colloidal surface.

Previous studies of IPCs in two-dimensional confinement [BLK13, BLK14] showed that, depending on the patch amplitude, particles self-assemble in a variety of ordered structures. The results are summarized in the upper panels of figure 5.1: particles with small patch semiamplitude ( $\gamma = 31.1^\circ$ ) do not form ordered structures at all, medium-size patches ( $\gamma = 45.6^\circ$ ) form a hexagonal layer in which all the patches of the IPCs have their orientations aligned with the layer, and larger patches ( $\gamma = 59.2^\circ$ ) formed another type of hexagonal lattice where some of the IPCs have their patches pointing outside the plane.

In this work, we extended these studies to three dimensions. We investigated the phase behavior of the model, varying interaction range, patch size and charge distribution, and searched for ordered structures that could spontaneously self-assemble in the density range  $\rho^* \leq 0.8$ . For these investigation, we developed our own code for a molecular dynamics (MD) simulation.

For small-patch models (left panel of figure 5.1), no ordered structure was found, as it was in two-dimensional confinement; in this case, we studied the thermodynamics of the fluid using an integral-equations approach, namely the reference hypernetted chain method developed by Fred Lado [Lad82]; we compared the results with Montecarlo simulation provided data by Bianchi [KBFK15], and the associative Percus-Yevick method developed by Kalyuzhni [KBFK15]. These techniques showed good results in the reproduction of the radial correlation function and in the prediction of pressure and energy. We also used MD simulations to explore the phase diagram of a neutral model with  $\gamma = 31.1^\circ$ , of which we also studied the dynamics, observing simple oscillations in the orientation that will become more complex for larger patch systems.

For medium-patch models (central panel of figure 5.1), we discovered a hybrid crystal-liquid structure, composed by the same hexagonal planes seen in two-dimensional confinement and by additional particles located between (and whose patches were pointing to) the layers. At very low temperature, these interlayer IPCs are trapped in minima and do not diffuse. However, for  $T^* > 0.045$ , interlayers IPCs have enough kinetic energy to hop between different minima, and acquire a mobility comparable to that of a fluid. We studied the dynamics by means of correlation functions, and we discovered complex oscillations in the orientational autocorrelation function; these oscillations are influenced by the hopping and the orientational autocorrelation functions exhibits a sharp transition at  $T^* \simeq 0.045$ . We also computed the phase diagram of the symmetric neutral model with  $\gamma = 45.6^\circ$ , and stud-

ied the stability of the crystal-liquid phase with respect to overcharging of the colloid center and of the patches, and the variation in size of one of the two patches. We observed that the overcharging of the colloid center improves the stability of the crystal-liquid phase, while overcharging of the patches weakens it.

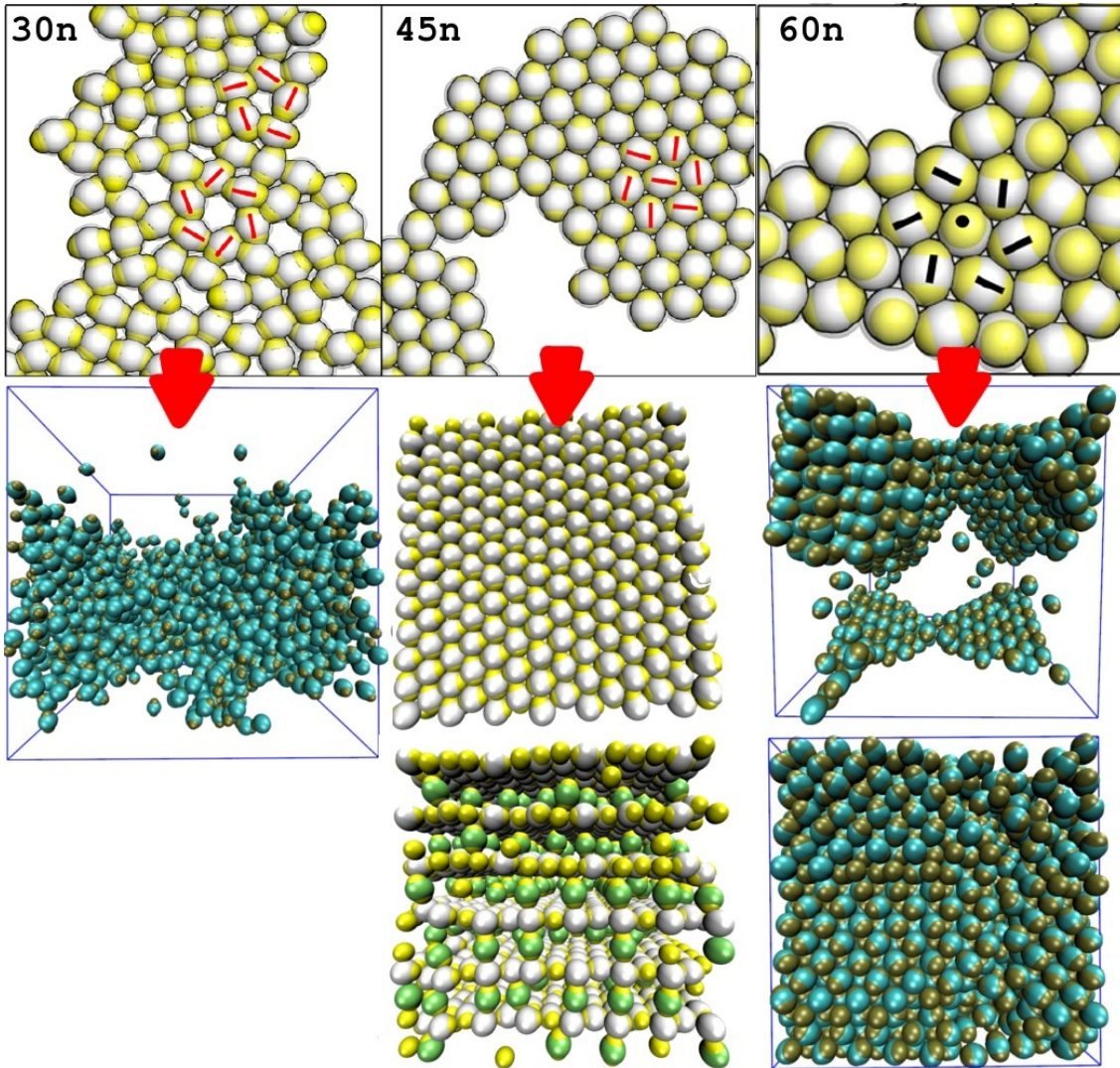


Figure 5.1: Structures formed by neutral IPCs in two-dimensional confinement (top panels) and in three dimension (lower panels, pointed by the red arrows). The patch amplitude grows from left to right. See the text for explanation.

For larger patch models (right panel of figure 5.1), we found an FCC structure, that if cutted along one of the diagonals of the cubes would appear like the planes seen in two-dimensional confinement. We saw that the FCC would form even at really low density, coexisting with the gas.

We also studied some models inspired by the experimental research of van Oostrum and coworkers [vOHNR15] and studied a charged model with patches asymmetric both in size and charge, compatible with the experimental IPC models, would (in absence of gravity)

spontaneously self-assemble in the crystal-liquid structure, while an overall neutral model with the same patch sizes would not.

Figure 5.2 summarizes all the ordered structure that spontaneously self-assembled, depending on the two patch semi-amplitudes  $\gamma_1$  and  $\gamma_2$ . The natural extensions of this work would be to complete the exploration of the parameters (charge, patch size and interaction range) of the model, and to further inquire the causes that trigger the self-assembly. It would also be insightful to systematically study all the ordered structures (not only the ones that self-assemble spontaneously) using solid-state methods such as those used in reference [NKD<sup>+</sup>14], although the work required would be huge. At  $T^* = 0$ , this task has been carried out by Doppelbauer in his Ph.D. thesis [Dop12], but at finite temperature the question remains open. Moreover, all the models studied in this work had two patches located at the opposite poles of the colloid; it would be interesting to study the behavior of a model with patches placed in other positions, or with three or more patches.

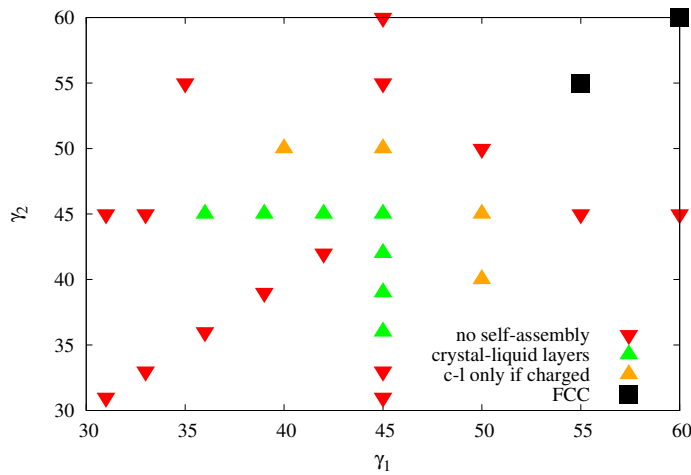


Figure 5.2: Ordered phases in function of the patch angles  $\gamma_1$  and  $\gamma_2$ . Combinations for which no ordered structure self-assembles are denoted by red downwards triangles; Upwards triangles show where the crystal-liquid structure was found (green if also overall-neutral IPCs could self-assemble, orange if only overall-charged models did); black squares denote the face-centered cubic lattice.



## Bibliography

- [AFST05] L. Angelani, G. Foffi, F. Sciortino, and P. Tartaglia, *J. Phys.: Condens. Matter* **17** (2005), L113.
- [And82] H. C. Andersen, *J. Comp. Phys.* **47** (1982), 1253.
- [AT87] M. P. Allen and D. J. Tildesley, *Computer simulation of liquids*, Oxford University Press, 1987.
- [BBL11] E. Bianchi, R. Blaak, and C. N. Likos, *Phys. Chem. Chem. Phys.* **13** (2011), 6397.
- [BH67] J. A. Barker and D. Henderson, *J. Chem. Phys.* **47** (1967), 2856.
- [BKL11] E. Bianchi, G. Kahl, and C. N. Likos, *Soft Matter* **7** (2011), 8313.
- [BLK13] E. Bianchi, C. N. Likos, and G. Kahl, *ACS Nano* **7** (2013), 4657.
- [BLK14] ———, *NanoLetters* **14** (2014), 3412.
- [Cac96] C. Caccamo, *Physics Reports* **274** (1996), 1 105.
- [Cal85] H. B. Callen, *Thermodynamics and an introduction to thermostatics*, Wiley, 1985.
- [CFR82] G. Ciccotti, M. Ferrario, and J. P. Rickaert, *Mol. Phys.* **47** (1982), 1253.
- [CS69] N. F. Carnahan and K. E. Starling, *J. Chem. Phys.* **51** (1969), 635.
- [DNBK12] G. Doppelbauer, E. G. Noya, E. Bianchi, and G. Kahl, *Soft Matter* **8** (2012), 7768.
- [Dop12] G. Doppelbauer, *Ordered equilibrium structures of patchy particle systems*, Ph. D. Thesis, Technische Universität Wien, 2012.
- [FBK] S. Ferrari, E. Bianchi, and G. Kahl, in preparation.
- [FBKK15] S. Ferrari, E. Bianchi, Y. V. Kalyuzhnyi, and G. Kahl, *J. Phys.: Condens. Matter* **23** (2015), 234104.
- [Fer72] E. Fermi, *Termodinamica*, second ed., Bollati Boringhieri, 1972.
- [Fre02] D. Frenkel, *Physica A* **313** (2002), 1–31.
- [FS02] D. Frenkel and B. Smit, *Understanding molecular simulations*, Academic Press, 2002.
- [GGL<sup>+</sup>14] A. Giacometti, C. Gögelein, F. Lado, F. Sciortino, S. Ferrari, and G. Pastore, *J. Chem. Phys.* **140** (2014), 094104.
- [GJC09] S. Granick, S. Jiang, and Q. Chen, *Physics Today* **July 2009** (2009), 68.
- [GLL<sup>+</sup>09] A. Giacometti, F. Lado, J. Largo, G. Pastore, and F. Sciortino, *J. Chem. Phys.* **131** (2009), 174114.
- [GLL<sup>+</sup>10] ———, *J. Chem. Phys.* **132** (2010), 174110.
- [Göt09] W. Götze, *Complex dynamics of glass-forming liquids*, Oxford University Press,

Bibliography

- 2009.
- [GRSG12] C. Gögelein, F. Romano, F. Sciortino, and A. Giacometti, *J. Chem. Phys.* **136** (2012), 094512.
- [GS07] S. C. Glotzer and M. J. Solomon, *Nature Mat.* **6** (2007), 557.
- [HCLG08] L. Hong, A. Cacciuto, E. Luijten, and S. Granick, *Langmuir* **24** (2008), no. 3, 621.
- [HM06] J. P. Hansen and I. R. McDonald, *Theory of simple liquids*, Academic Press, 2006.
- [KB11] W. Kob K. Binder, *Glassy materials and disordered solids*, World Scientific, 2011.
- [KBFK15] Y. V. Kalyuzhnyi, E. Bianchi, S. Ferrari, and G. Kahl, *J. Chem. Phys.* **142** (2015), 114108.
- [Kra07] V. Krakoviak, *Phys. Rev. E* **75** (2007), 031503.
- [Lad82] F. Lado, *Mol. Phys.* **47** (1982), 283.
- [MFV09] B. Madivala, J. Fransaer, and J. Vermant, *Langmuir* **25** (2009), no. 5, 2718–2728.
- [NB15] E. G. Noya and E. Bianchi, *J. Phys.: Condens. Matter* **27** (2015), 234103.
- [NKD<sup>+</sup>14] E. G. Noya, I. Kolovos, G. Doppelbauer, G. Kahl, and E. Bianchi, *Soft Matter* **10** (2014), 8464.
- [Pat96] R. K. Pathria, *Statistical mechanics*, 2nd ed., Elsevier, 1996.
- [PK10] A. B. Pawar and I. Kretzschmar, *Macromol. Rapid. Commun.* **31** (2010), 150.
- [QdGQ<sup>+</sup>12] Weikai Qi, Joost de Graaf, Fen Qiao, Sergio Marras, Liberato Manna, and Marjolein Dijkstra, *Nano Letters* **12** (2012), no. 10, 5299–5303.
- [RJWS09] I. B. Ramsteiner, K. E. Jensen, D. A. Weitz, and F. Spaepen, *Experimental observation of the crystallization of hard-sphere colloidal particles by sedimentation onto flat and patterned surfaces*, *Phys. Rev. E* **79** (2009), 011403.
- [Ros90] Y. Rosenfeld, *J. Chem. Phys.* **93** (1990), no. 6, 4305–4311.
- [RSI<sup>+</sup>11] L. Rossi, S. Sacanna, W. T. M. Irvine, P. M. Chaikin, D. J. Pine, and A. P. Philipse, *Soft Matter* **7** (2011), 4139.
- [SABW82] W. C. Swope, H. C. Andersen, P. H. Berens, and K. R. Wilson, *J. Chem. Phys.* **76** (1982), 637.
- [SBK15] M. Stipsitz, E. Bianchi, and G. Kahl, *J. Chem. Phys.* **142** (2015), 114905.
- [SGP09] F. Sciortino, A. Giacometti, and G. Pastore, *Phys. Rev. Lett.* **103** (2009), 237801.
- [vOHNR15] P. D. J. van Oostrum, M. Hejazifar, C. Niedermayer, and E. Reimhult, *Simple method for the synthesis of inverse patchy colloids*, *J. Phys.: Condens. Matter* **27** (2015), no. 23, 234105.
- [Voi02] T. Voigtmann, *Mode coupling theory of the glass transition in binary mixtures*, Ph. D. Thesis, Technische Universität München, 2002.
- [VPS<sup>+</sup>13] T. Vissers, Z. Preisler, F. Smallenburg, M. Dijkstra, and F. Sciortino, *J. Chem. Phys.* **138** (2013), 164505.
- [VW72] L. Verlet and J. J. Weis, *Phys. Rev. A* **5** (1972), 939.

- [Wer84a] M. S. Wertheim, *J. Stat. Phys.* **35** (1984), 19.
- [Wer84b] ———, *J. Stat. Phys.* **35** (1984), 35.
- [Wer86a] M.S. Wertheim., *J. Stat. Phys.* **42** (1986), 459.
- [Wer86b] M.S. Wertheim, *J. Stat. Phys.* **42** (1986), 477.
- [Wer87] ———, *J. Chem. Phys.* **88** (1987), 1145.





## 6 Widmung (ringraziamenti)

Prima di salutarvi, devo dire un enorme grazie: grazie al cazzo.

---

Io

F\*\*\* you, Silvano.

---

Clara, Giannis, Marta and Moritz. Many, many times.

Jedes Mal ich eine Thesis lese, die erste Sache ich schaue ist die Widmung. Und jedes Mal der erste Dank geht zum Supervisor. Am Anfag dachte ich "was für ein/e Arschkriecher/in"; nur wenn meine Zeit zu danken gekommen ist, habe ich verstehen dass, nach viele Nächte vergangen beim Schreiben, die erste Person dass du danken willst, ist der/die die ebenso viele Nächte beim korrigieren vergangen hat. Deswegen geht mein erster Dank zu **Gerhard**, und zu seinen Vorgänger **Giorgio Pastore** und **Piero Olla**. (spricht ihr alle deutsch, oder?)

Ringrazio **alla famiglia**, in particolare **a mia mamma**, pilastro imperituro di pazienza e maestra con l'eseempio, e **a mio babbo**, tre volte sulla polvere, tre volte sull'altar, fuori come un balcone come tutti i Ferrari. Lei è l'applicazione vivente della regola numero 2; lui mi ha ripetuto la numero 1 finché io non l'ho imparata a memoria, e lui l'ha dimenticata. **A nonna Anna**, fonte dell'incoerenza, **a nonno Silvano** fonte di genialità e burberità, **a nonna Meloni** e al suo sguardo inoppugnabile, e **a nonna Emilia**, fonte della regola numero 4.

Grazie a tutti soggetti oristanesi che hanno allietato la mia gioventú bruciata: **Caggia, Smada, Mizio, Pix, Concu, Carlonia, Ziccu; Roddie** (il sogno di ogni donna), **Leo** (leggendario anello di connessione tra ommu e mraxani), **Nico** e quel coglione di **Loddo**; l'avvocato ragionier **Dando, A(C + F), Kuzzo, Ghinamo**, il divino **Enricus**, e **Feffe**. E chiunque abbia mai messo piede nel MIO campetto.

Sa zenti macca conosciuta a Cagliari: **Pinball, Sonja, Mawro**, i magnanimi ma non abbastanza **Furbizio e Luisella**, la sempiterna magnanima **Gemmina, Collu (e Pinna), Pinna (e Collu), Maria V. Tiddia, Adri, Piccola Paola**, gli sfigati di Medaglia e Sigma.

**Fiore, Marty, An(tonio + tonino + na), FaBBio Nitella, Chiara Riosi**, i muli di villa Ara, "bon, puri sti mona de preti, diopoi, cosa ghe xe"[citazione necessaria].

Die liebe Leute in Wien: **Dario** dalla logica brillante, **Marylly** de la pratique exceptionnelle, **Sebastian** und **Moritz**, die mir gelernt haben was ein guter Österreicher sagen soll (eh, shiach, oida, dem Mann seine Jacke) und was nicht (jawohl, lecker, des/der/des/der), **Dieter** der Allmächtig, die lustige **Ismene** und **Stefan, Emanuela** und **Peter**, und die mütterliche Frau Höller und Riedler. Und das Lang Zentrum!

Il penultimo ringraziamento va alle seguenti persone, che non trovavano ovvia collocazione nei gruppi precedenti: **Giuseppe e Matteo Pitzalis, Stefania Zireddu, Davide**

**Angius e Cenn (sic!) Danieli.**

Le ultime persone che ancora non ho ringraziato meriterebbero un libro intero, ma come direbbe Pier cercando di alzare una serranda, "non fa". Spero che anche per voi un disegno valga mille parole.



//(minca mia a me spero di non aver dimenticato nessuno)



MARTA:  
LA MIA FIAMMA BRESCHI.

posso solo ringraziarti!

[citazione necessaria]



KANE E SCIMMIA:  
I MIEI FRATELLINI!



BOBONE:  
ECCE OMMU.  
ARES ES!



SPADRI:  
MAI CAPITO PERCHE' MI  
STA COSI' SIMPATICO!





## 7 Curriculum Vitae

### Lebenslauf

#### Persönliche Daten

---

**Name** Silvano Ferrari  
**Geburtsdatum** 7 Juni 1988  
**Geburtsort** Oristano, Sardinien, Italien  
**Staatsbürgerschaft** Italienische



#### Ausbildung

---

2013 – jetzt **Doktoratstudium**  
PHYSIK WEICHER MATERIE  
Technische Universität Wien

2010 – 12 **Masterstudium**  
THEORETISCHE PHYSIK  
Universität Triest

2007 – 10 **Bachelorstudium**  
PHYSIK  
Universität Cagliari

#### Publikationen

---

1. **Inverse patchy colloids with small patches: fluid structure and dynamical slowing down**, S. Ferrari, E. Bianchi, Y. Kalyuzhnyi, and G. Kahl, Journal of Physics: Condensed Matter 27, 234104 (2015)
  2. **Theoretical and numerical investigations of inverse patchy colloids in the fluid phase**, Y. Kalyuzhnyi, E. Bianchi, S. Ferrari, and G. Kahl, Journal of Chemical Physics 142, 114108 (2015)
  3. **From square-well to Janus: Improved algorithm for integral equation theory and comparison with thermodynamic perturbation theory within the Kern-Frenkel model**, A. Giacometti, C. Goegelein, F. Lado, F. Sciortino, S. Ferrari, and G. Pastore, Journal of Chemical Physics 140, 094104 (2014)
-